ABSTRACT

Title of Document: **EVALUATION AND MODELING OF ELECTROCHEMICAL MIGRATION ON PRINTED CIRCUIT BOARDS**

Xiaofei He, PhD, 2014

Directed by: *George Dieter Chair Professor* Michael G. Pecht, *Assistant Research Scientist* Michael H. Azarian, Department of Mechanical Engineering

Electrochemical migration (ECM) is the growth of conductive metal filaments on a printed circuit board (PCB) through an electrolyte solution under a DC voltage bias. ECM can cause a reduction in surface insulation resistance (SIR) between adjacent conductors and lead to intermittent or catastrophic circuit failures. The kinetics of the electrochemical migration process between copper traces in deionized water was investigated using electrochemical impedance spectroscopy and cyclic voltammetry. The rate limiting step was identified to be anodic diffusion before and during dendritic growth. Based on this, a model was developed to describe the kinetics of electrochemical migration under condensed and non-condensed conditions between copper conductors on printed circuit boards using Nernst Planck equation and impedance measurement. It was found that by acquiring electro-active ion surface concentration at anode with the help of impedance measurement and by considering migration and diffusion in the bulk ion transport, the model matches the experimental results quantitatively. Historical models are applied to the experimental results and compared with the model of this study.

EVALUATION AND MODELING OF ELECTROCHEMICAL MIGRATION ON PRINTED CIRCUIT BOARDS

By

Xiaofei He

Dissertation submitted to the Faculty of the Graduate School of the
University of Maryland, College Park in partial fulfillment
of the requirements for the degree of
Doctor of Philosophy
2014

Dissertation Committee:
Professor Michael G. Pecht (Advisor and Chair)
Professor Mohamad I. Al-Sheikhly (Dean's Representative)
Professor Daniel E. Falvey
Professor Chunsheng Wang
Professor Patrick McCluskey
Dr. Michael H. Azarian (Co-advisor)

Acknowledgements

I would like to thank my advisor, Professor Michael G. Pecht, for his continuous and valuable instructions, generous help, unqualified endorsement and amusing tolerance to me;

I would like to thank my co-advisor, Dr. Michael H. Azarian, for his continuous and valuable instructions, generous help, unqualified endorsement and amusing tolerance to me;

I would like to thank Professor Chunsheng Wang, for his valuable instructions, generous help and unqualified endorsement;

Thank my colleagues in CALCE for their warm and generous help;

Finally, thank my family especially my mother, for their love, high expectations and timely reliefs, as always.

Table of Contents

Introduction

With the miniaturization, higher power and higher density trend of modern electronics products, the electrical bias together with the presence of moisture, can trigger an electrochemical phenomenon, called electrochemical migration (ECM) on printed circuit boards (PCBs). This phenomenon can cause a reduction in surface insulation resistance (SIR) between adjacent conductors, generate leakage current and lead to intermittent or catastrophic circuit failures.

Chapter 1 gives a general literature review over ECM propensity of lead free solder, rate limiting step and cell kinetics and historical physicochemical models on ECM. ECM of assemblies with tin lead solder has been studied for a long time, but the propensity for ECM of lead free solder is still not understood well. With the transition from tin lead solder to lead free solder in recent years, electronic systems may incur more uncertain ECM risk. This necessitates the comparison between the effects of tin lead and lead free solder on propensity for ECM. So this issue is discussed in chapter 2. In addition to solder alloy, some other factors including board finishes, electrical field and spacings in terms of their effects to ECM are also discussed. The long term electrochemical behavior of lead free solder under environmental stresses manifested in the study has significant implications to its industrial usage conditions, so it is simulated with Armstrong's 3-D nucleation models to interpret its underlying physical mechanisms, which sheds light on its long term electrical behavior.

In addition to evaluation some key factors' influence to ECM, the rate limiting step of ECM out of its successive steps, such as electrodissolution, ion transport, electrodeposition, is studied. This work can pave way for developing an accurate model of the time-to-failure, and helpful for devising strategies to mitigate ECM. This is discussed in chapter 3.

Chapter 4 discusses a mathematical model to describe ECM based on Nernst Planck ion transport equations. The motivation of this work stems from the hardship of applicability of historical models to industry, which used macroscopic parameters or hardly measurable parameters to describe ECM. While the model built up in this work uses microscopic and measurable parameters, to directly cope with ECM. It can not only be used to confirm experimental results, but it also can be used to predict the time to failure of printed circuit boards when the dominant failure mechanism is ECM.

Chapter 5 is the conclusive section, summarizing the evaluation of factors to affect ECM and the modeling of ECM. The factors include solder alloys, finishes, electrical fields, spacings, and flux solids. The models include an equivalent circuit model associated with impedance spectra used to determine rate limiting step (chapter 3) and an ion transport model to describe the whole ECM process (chapter 4).

Chapter 1 Literature Review

S. Chaikin, et al [1], investigated silver migration on printed circuit boards using different substrates under 96% relative humidity, 40C and 480 V DC bias and 1/4 inch spacing. The substrates included Polystyrene, Polyethylene, Poly(viny1 chloride), Silicone-glass, Epoxy-glass, Teflon-glass, XXXP (paper based phenolic), Nylon, etc. It was found that Nylon could grow extensive dendrites, XXXP grew heavy dendrites, Teflon-glass and epoxy glass grew slight dendrites, while polystyrene and polyethylene did not grow dendrites. It was also found that XXXP and Melamine-glass were sensitive to temperature, with their dendritic growth becoming more severe with temperature from 30C to 85C, while epoxy-glass and Teflon-glass did not show much sensitivity to temperature.

F. Ogburn, et al [2], investigated the structure of lead dendrites by using x-ray diffraction. It was found that the dendrites grown were flat, with a thickness from 15 to 90 microns. The branching was 60° to the main stalk. The twist angle decreased with the increase of rate of growth. The dendrites growth direction was between <211> directions or <110> directions. The cross-sectioning of dendrites showed that dendrites had voids and channels.

G. Marshall and P. Mocskos [3] used Nernst Planck equations and Navier-Stokes equations to mimic the ramification of dendritic growth. Their approach considered the effect of diffusion, migration and convection of ions and electrolyte, with an emphasis of convection of electrolyte. Their simulation showed that with the advance

of dendrites, two contra-vortices were generated beside the tip of dendrites and pinched by the branches of dendrites. The cation, anion, and potential profile with 1-D and 2-D analysis were also simulated.

G. Marshall, et al [4] considered the gravity and electrical effect on the dendritic growth process. Their simulation showed that the density change close to cathode and anode before the dendritic growth can induce convections and result two vortices close to electrodes. The two vortices finally collide and become an overall vortex throughout the cell. The size of the vortices grows initially as $t^{0.8}$ with time t, but decreases to $t^{0.5}$ in the later stage. This paper confirmed experimental results from other researchers, but the choosing of the simulated parameters is open to questions since they are significantly different from typical experimental values.

L. Hua and J. Zhang [5] investigated the corrosion propensity and electrochemical migration property of Zn doped lead free solder (64Sn-35Bi-1Ag). It was found that Zn doping accelerated the time-to-failure, which was 100 hrs compared to 240 hrs for non-doped 64Sn-35Bi-1Ag solder for a 3mm spacing under 80°C, 85%RH and 3V bias conditions. The dendrites generated by Zn doped solder contained Zn and Sn as the main migrated metal, while the dendrites generated by non-doped solder contained Sn as the main migrated metal. Zn doping also lowered the equilibrium potential (corrosion potential) when subject to a 3 wt% NaCl solution corrosion test and thus increased corrosion propensity of 64Sn-35Bi-1Ag solder. So Zn doping degrades the reliability of 64Sn-35Bi-1Ag in terms of ECM and corrosion. However, the reason why this happens was not probed.

L. Hua, et al [6], investigated the corrosion and ECM propensity of Zn and Ge doped Sn-3.0Ag-0.5Cu solder in 3.5 wt% NaCl solutions. It was found that the corrosion potential of Zn doped SAC solder decreased with the amount increase of Zn (0.1 wt% ~8 wt%), while the Ge doped SAC solder incurred the minimum corrosion potential at a Ge proportion of 1 wt% (0.1 wt% ~8 wt%). Both Zn and Ge doping accelerated dendritic growth of SAC solder under 3V bias in 3.5 wt% NaCl solutions, with the major migrating metal being Sn. It was also found that the anti-oxidation capability of SAC solder was increased by Ge doping, but decreased by Zn doping.

M. Moshrefi [7] used thermal cycling and bias test to investigate the reliability issues of Sn-3.0Ag-0.5Cu. The temperature was from -20C to 100C, with a ramp up rate of 3C/min and a 20 min dwell. The bias was 50 V between lead frames. It was found white residues occurred after thermal cycling test between lead frames and at the edge of soldered traces. Out of the 4 SAC soldered boards from four manufactures, only one board did not incur white residue. Other 3 boards incur white residues at 82 to 250 locations. Sulfur was detected in the white residue; however, the composition of white residue was not clarified.

B. Liu, et al [8], used 5% NaCl fog spray to pretreat SnPb and SAC solder balls followed by a thermal cycling test. The temperature was from 0C to 100C, with a ramp up rate of 10C/min and a 10 min dwell. It was found that the pretreatment to SnPb solder did not affect the characteristic life compared to as-received SnPb solder, but the pretreatment to SAC solder did reduce the characteristic life by 43% compared to as-received SAC solder.

K. Hansen, et al [9] investigated the effect of flux residue on PCBs after wave and reflow soldering. It was found that a major organic acid of the flux was adipic acid, which did not chemically degrade until 250C, the peak temperature of wave soldering. Even if at this temperature, 0.5 wt% of flux residue will be left on the PCBs. At 300C, all the acids in the flux were gone. The local SIR measurement corresponded to the weight measurement with temperatures. The leakage current of flux residues at 250C dissolved in DI water was almost 1 order of magnitude lower than flux residue at 170C dissolved in DI water.

D. Minzari [10], et al, studied ECM on 10KOhm surface mount ceramic resistor which included Sn-Pb (2% Pb) terminals and alumina substrate using 5V and 12V bias and 10 ppm NaCl electrolyte. It was found that at 5V the dendrites had larger side branches while at 12 V the dendrites were mainly a long trunk. The dendrites growth process did not change current much until the dendrites touched anode the current increased significantly. Also there was a pH gradient increasing from anode to cathode after applying voltage to the cell for a few seconds. The time to failure (summation of incubation time and growth time) was from 18 s to 317 s with large scatter regardless of voltage applied. But the problem is, the sample size was only 2 (only twice for each voltage), so little statistical significance can be drawn. Another finding was that dendrites are made up of an oxide shell and a metallic core through TEM analysis.

L. Hua, et al [11] compared the corrosion behavior between 64Sn-35Bi-1Ag solder and Zn doped 64Sn-35Bi-1Ag solder using potentiodynamic polarization in 3% NaCl

solution. It was found that Zn doped accelerated corrosion and lowered the corrosion potential. The more Zn percentage, the lower the corrosion potential. ECM test were also performed in 80C and 85%RH on two electrodes (3cm apart) reflowed with 64Sn-35Bi-1Ag solder with and without Zn doping in 3V. The Zn doping reduced time to failure from 240 hrs to 100 hrs.

D. Minari, et al [12] performed water drop test on surface mount resistors and capacitors with Sn as terminals at 5V and 12 V. The gap was around 1 mm. Chloride, bromide, adipic acid, and pH controlling materials (HNO3 and NaOH) were used to characterize the dendritic growth probability. It was found that at a relatively low concentration of chloride, bromide, and adipic acid, the dendrites are more likely to grow, but once the concentrations are above a limit (chloride 1000 ppm, bromide 250 ppm, adipic acid 1000 ppm), there are no dendrites. There exists an optimal dissolution and migration kinetics to induce dendrites. Slower or faster than that, no dendrites grow. The reason was explained that too much dissolution of Sn ions trigger the formation of stannate ions at cathode, which bear negative charge and can be expelled by cathode, thus lowering the chance to grow dendrites. Pourbaix diagram and local pH change were also introduced to explain the Sn ion stability. But the explanation tends to constitute a hypothesis instead of a supported theory.

S. Ho, et al [13] studied the role of barrier layer of Ni-B in the ECM. It was found that a thickness of 0.6 μm Ni-B (1%B) plated onto Cu can effectively suppress ECM. Without this layer, the SIR of Cu traces transited from 10^{14} Ohms to 10^{8} ~10^{9} Ohms after a 10V/85C/95%RH exposure for 7 days. With this layer, the SIR maintained

higher than 10^{14} Ohms after 10V/85C/95%RH exposure for 7 days. In addition, it was speculated that the control step is the reduction of cations at cathode. However, this was not proved by their experimental results.

C. Gabrielli, et al [14] studied the copper dendrite growth in oxalic acid. Oxalic acid is a cleaning agent in post chemical mechanical polishing process. The experiments were conducted using disk+disk pattern and disk+bar pattern with a distance (0.3~10 μm) and a voltage (0.4~1.2 V). It was found that at a lower oxalic acid concentration (10^{-4} mol/L), the filamentary dendrites are more likely to grow. At a higher oxalic concentration (10^{-3} mol/L), the dendrites are more compact and thick. The failure time increases with distance under the same voltage. In such a condition, it was concluded that diffusion from anode rather than migration dominated the ECM.

O. Devos, et al [15] studied the dendritic growth in oxalic acid solution. It was found that during the incubation period the migration of ions from anode to cathode dominates the process. Two inhibitors were also tested to check their effectiveness in suppressing dendritic growth. One inhibitor, 3-me´thyl-1,2,4-triazole-5-thiol was found very effective. The higher its concentration, the lower chance dendrites grow.

L. Zou, et al [16] studied a few different fluxes in affecting the dendrite growth between Cu traces (0.2 mm gap) using electrochemical impedance spectroscopy (EIS). It was stated that a lower contamination level results in a ion transport dominance between traces, while a higher contamination level leads to a control by interfacial electrochemical processes, thus increasing the chances to grow dendrites at cathode. This statement, however, is questionable.

C. P. Fabian, et al [17] studied two organic materials' role in copper electrodeposition using EIS. The two organic materials are activated polyacrylamide (APAM) and guar, a type of sugar. It was found that APAM can increase the charge transfer resistance and thus suppresses the kinetics, behaving as an inhibitor in the deposition. But guar slightly decreases the charge transfer resistance, so it does not behave as an inhibitor. The reason was proposed to be the more inclination of APAM to be specifically adsorbed in IHP layer.

Modeling:

Barton & Bockris [18] studied the Ag dendritic growth in AgNO3 electrolyte and built up a mathematical model. This is the first model to describe dendrite growth with respect to overpotential and concentration. The model predicts a constant growth speed under constant potential by assuming diffusion control current-potential kinetics. When exchange current approaches infinity, the maximum dendrite growth speed is proportional to square of cathode overpotential. When exchange current approaches zero, the maximum dendrite growth speed is proportional to cathode overpotential. But it does not consider the metal dissolution and migration to initiate dendrites, thus cannot determine the incubation time.

Chazalviel [19] simulated the dendritic growth process. A depletion layer is shown in the vicinity of dendrites by the simulation of cell concentration profile using Nernst Planck equations for ion transport and Poisson equation for electric field. The time for depletion layer to form at cathode:

$$t \propto \frac{1}{(J\mu_a)^2}$$

This time can be used to approximately calculate the incubation time.

V. Fleury [20] performed an extensive study of electrochemical deposition under galvanostatic condition without supporting electrolyte. It was found that the dendrite growth speed is proportional to anion mobility and electrical field.

$$\upsilon = \mu_a E$$

This can be used to calculate the growth time with respective to anion mobility and electrical field.

J. C. Bradley [21] studied the dendrite incubation and growth process. It was assumed that incubation is migration controlled. The incubation time is proportional to gap distance and the inverse of electrical field. This model claimed growth period is more likely convection controlled.

$$t_{incubation} = \frac{L}{\mu E}$$

G. Marshall [22][23] built a comprehensive model to simulate dendrite growth process using Nernst-Planck equation to describe ion transport process, Poisson equation for electrical potential profile, Navier-Stoke equation for electrolyte velocity. The main focus was on convection in the dendrite growth. But it only has qualitative agreement with experimental results.

DiGiacomo [24] developed a model that depicts the TTF as the ratio of circuit physical parameters to stress conditions (voltage, temperature, relative humidity (RH)). The assumption was migration controlled, same as Barton & Bockris. Its major

advantage was the depiction of ionic current with respect to RH, in which the humidity factor matched B.E.T. adsorption isotherm III. The validity of overall model was not experimental confirmed.

Yang [25] studied the Ag migration process on PCBs in non-condensing conditions. He developed an overall regression TTF model using voltage, temperature and RH. The use of B.E.T. isotherm helped to determine the surface conductivity of pure adsorbed water with respect to temperature and humidity. This model claimed the TTF is proportional to inverse of voltage. However, the surface conductivity obtained in non-dendrite condition was used in the model as the surface conductivity under dendrite growth to calculate the TTF, which is open to questions.

Solder ECM Propensity:

P. A. Kohl [26] studied the electrodeposition of Sn/Pb alloys and the effects of surface agents in fluoboric acid electrolyte. It was found that when current is beyond 800 mA/cm2, smooth and semi-bright deposits can be produced. The addition of polymeric surfactants can suppress the dendritic growth, and the addition of lactones can help distribute currents uniformly.

D. Shangguan, et al [27] stated that the propensity of Sn-Ag (96.5/3.5) solder to ECM is less than that of Sn-Pb-Ag (62/36/2) solder because solder with high Sn content tends to form a protective tin oxide layer, tin dendrites easily break, and a higher reflow temperature of lead-free solder leaves less flux residue. Also it was found that Sn-Ag (96.5/3.5) solder with Ag conductor has the least inter-diffusion distance and

the largest adhesion strength. So the conclusion was that Sn-Ag (96.5/3.5) solder is a superior solder alloy fit for solder interconnects in thick film automotive electronics packages when Ag conductor is used.

T. Takemoto, et al [28] studied ECM propensity of solder alloys in distilled water under constant voltages. It was found that in Sn-Pb alloy systems, Pb is the major metal constituting the dendrites. Under a given voltage, pure lead's time to short is around 100 s while pure tin's time to short is around 1000 s. It was also found that pure In, In-50Pb, In-48Sn, and Sn-1.2Al were immune to ECM.

G. Harsanyi [29] studied the ionic contaminants' effect on the migration behavior of different metals. It was found that with Cl- , the Au, Pd and Pt can form complexes ($AuCl_4^{2-}$, $PdCl_4^{2-}$, $PtCl_4^{2-}$) and increase their ECM propensity. While for metals such as Ag, Cu, Sn, and Pb, their migration were accelerated with the presence of the ionic contaminants, but when the contamination level increases to some medium level, a precipitation can occur to hinder or stop the ECM process.

B. A. Smith, et al [30] studied the role of weak organic acids used in low solids fluxes in the ECM. The weak organic acids included succinic acid, glutaric acid, and adipic acid. IPC-B-24 board, with these three acids sprayed, was used to perform the SIR test at 85C/85%RH and 40C/93%RH at 50V. It was found that glutaric acid and adipic acid incurred dendrites, while succinic acid did not. On succinic sprayed boards, green copper complexes generated at lower temperature, while blue copper chelates generated at higher temperature. Due to the thermal effects on the flux

residue, it was claimed that a higher temperature at 85C might be inappropriate since it evaporated some of the flux residues.

R. Manepalli, et al [31] studied the threshold voltage for Ag corrosion and ECM initiation on a Ag line with a gap of 0.1 mm at 85C/85%RH. The substrate was silica. It was found that threshold voltage is 3V for ECM to occur. A higher voltage did not necessarily result in a shorter time to failure, which could not confirm DiGiacomo's model well.

W. Jud Ready, et al [32] studied the SIR behavior of IPC-B-24 boards (0.5 mm spacing) at 85C/85%RH/100V with a daily and hourly measurement. A variety of flux was used before wave and reflow soldering. The substrate was FR-4. It was found that SIR increased in general with intermittent drops due to dendritic growth. Also it was found that daily SIR measurement was not sufficient to detect dendritic growth, while hourly SIR measurement was able to perceive dendritic growth. Both daily and hourly SIR measurements were not able to detect CAF growth.

S. Yoshihara, et al [33] studied the migration characteristics of lead free solder versus SnPb solder by Quartz Crystal Microbalance technique in situ. This technique is to measure the increase of resonant frequency due to the loss of weight at anode to monitor the dissolution kinetics. It was found that lead-free solder dissolve slower than SnPb solder and shows better migration resistances in general.

M. S. Moats, et al [34] studied the cupric ions' diffusivity dependence on copper ion concentration, acid concentration and temperature. Copper ion concentration was 35~70 g/L. The acid concentration was 160~250 g/L. Temperature was 40C~65C. It

was found that increasing the copper ion and acid (H2SO4) concentration slightly decreased the diffusivity. The temperature had an obvious effect on the diffusivity. The diffusivity decreased around 20% for each 10C temperature decrease.

K. Mondal, et al [35] studied the removal of copper ions by electrodeposition at 45C. It was found that in the copper ion concentration within a 1~1.4 g/L range, the diffusivity of copper ions was $6.3x10^{-7}$ cm^2/s to $1.5x10^{-6}$ cm^2/s. Nernst Planck equation was used to model the process. It was found that copper ions removal speed was 4 times greater than the speed of nickel ion removal. Also O-Phosphoric acid was found to be a suitable catholyte for the removal of metal impurities.

T. Zapryanova, et al [36] studied the electrochemical growth of single copper crystals on a tungsten electrode in a CuSO4 + Na2SO4 (2 mol/L)+H2SO4 (0.5mol/L) electrolyte at 35C. The concentration of copper ions was from 0.01 ~ 0.04 mol/L. It was found that the diffusivity of copper ions was $9.75x10^{-6}$ cm^2/s. The charge transfer coefficient alpha was 0.5. Since the electrolyte was a large excess of supporting electrolyte, the kinetics of the system was determined by multi-step charge transfer and diffusion.

A. Carey, et al [37] studied the copper ion diffusivity dependence on concentration. They found that at high ionic strength electrolyte, the copper ion's diffusivity can deviate pretty far from the diffusivity at infinite dilution. It was found that the diffusivity can decrease from $8.58x10^{-6}$ cm^2/s to $3.2x10^{-6}$ cm^2/s when concentration increased from 0 to 0.2 mol/L. When concentration increased from 0.2 to 0.36 mol/L, the diffusivity decreased to $2.6x10^{-6}$ cm^2/s. Their study also claims that other

unknown non-Fickian process probably existed in addition to the traditional Fickian diffusion process in a high ionic strength electrolyte.

D. Q. Yu, et al [38] studied the ECM of SnPb and lead-free solder using DI water under 3V, 5V and 10 V voltages. The gap was 0.5 mm. It was found that in Sn-37Pb and Sn-36Pb-2Ag, Pb was the major migrated metal. For lead free solders such as Sn-Ag and Sn-Ag-Cu, Sn was the major migrated metal. For Sn-8Zn-3Bi, both Sn and Zn migrated. A higher electrical bias resulted in a shorter failure time. The morphology of Pb dendrites was stick-like, Sn dendrites were gracile-like, and Zn dendrites were feathers-like.

D. Q. Yu, et al [39] studied the ECM of SnPb and lead-free solder using DI water under 3V, 5V and 10 V voltages on FR-board with a gap of 0.3 mm. It was found that in Sn-37Pb and Sn-36Pb-2Ag, Pb was the major migrated metal. For Sn-3.5Ag and Sn-4Ag-0.5Cu solder, Cu migrated due to the poor wettability of solder paste which led to exposure of Cu traces to DI water. Cu dendrites were grapes or bumps-like. The resistances of Pb, Sn, Cu and Zn dendrites varied from a few KOhms to 150 KOhms.

S. Zhan, et al [40] studied the ECM on Conformally coated (silicone, urethane and acrylic) PCBs with no-clean flux under 6~42 V with a spacing of 0.16~0.64 mm. Sn-37Pb solder was coated onto the copper traces. 40C/93%RH and 85C/85%RH environmental conditions were used. It was found that silicone was better than urethane in retarding SIR degradation, which was in turn better than acrylic. The trapping of fibrous contaminants below the conformal coating can build up a

preferential metal migration path and accelerate the ECM. It was also found that test at 40C/93%RH could better accelerate the test failure than 85C/85%RH, because 85C evaporated some amount the weak organic acids from the flux residues and decelerated the test failures.

Y. Tsai, et al [41] studied the effect of complex agents on the electrochemical co-deposition of Sn-Bi alloys using linear sweep voltammetric technique. The complex agents include citric acid, ethylenediaminetetraacetic acid (EDTA), and polyethylene glycol (PEG). It was found that a synergistic effect of these three complexes (0.4M citric acid, 1M EDTA, and 0.2M PEG) can lower the deposition potential of Bi to close to Sn. The addition of EDTA and PEG significantly suppressed the growth of dendrites.

B. Noh, et al [42] studied the ECM resistances of SnPb and SAC305 solder on FR-4 board with 0.1, 0.318 and 1.0 mm gaps under both distilled water and THB conditions. 6.5V and 15V DC were used for water drop test. 85C/85%RH/50V was used for THB condition. It was found that SAC solder had longer TTF than SnPb solder at all the distances and voltages. Under THB condition the SAC solder incurred less intermittent SIR drops than SnPb solder. So the overall conclusion was SAC solder had higher ECM resistances than SnPb solder under bulk water or adsorbed moisture electrolytes.

C. Dominkovics, et al [43] studied the fractal dimension of lead-free and SnPb solder alloys coated with different finishes. They used water drop test to generate dendrites at 10V across 0.5 mm and 1 mm spacings on FR4 boards. It was found that the fractal

dimension of Ag to be 1.82, Cu to be 1.74, Sn 1.66, and SAC387 1.58, which are considered as a characteristics of different metals. It was also found that the fractal dimension of overall solder alloy is the molar weighted mean of the original metals' fractal dimensions.

Y. H. Xia, et al [44] studied the ECM propensity of lead-free solders vs SnPb solder. They conducted the water drop test on Cu traces spaced from 0.15 mm~0.95 mm with a voltage of 3V, 5V, and 10V. The substrate was FR-4 board. The time to short for all the solder alloys were from 20s to 120s at 0.65 mm spacing. An increase of spacing from 0.15 mm to 0.95 mm increased the time to failure from 20 s to 500 s. It was also found that too much flux residues that covered the entire copper traces could retard the occurrence of ECM. This finding was quite contrary to the usual findings reported by other researchers. Also for Pb-bearing solder, the major migrated metal was Pb; for Sn-Ag-Cu solder, Sn and Cu migrated; for SnZnBi solder, only Zn migrated. This confirmed other researchers' findings.

S. Zhan, et al [45] studied the ECM of SnPb solder with no clean flux (aqueous based and rosin based) under THB conditions. A voltage of 6~24 V across 0.16~0.64 mm spacings were applied on copper traces coated with SnPb solder on FR4 board. The THB conditions were 40C/93%RH, 65C/95%RH and 85C/85%RH. It was found that rosin based flux led to a worse reliability and more SIR failures than aqueous based fluxes. This was because rosin based flux left 50% more organic acid residues on the boards, whose hygroscopic nature had helped to adsorb moisture and helped build up

an electrolyte. The intermittent SIR drops were explained to be due to the breaching and rehealing of passivation layer.

S. Lee, et al [46] studied the ECM propensity of Sn and Pb metal on silica substrate with a voltage of 0.5~3V across 0.3 mm spacing in a 0.001 wt% NaCl electrolyte. It was found that Sn passivated but Pb did not. Under constant voltages, the current of Sn electrodes was a couple of order of magnitude less than that of Pb. Under the same voltage, the TTF of Sn was longer than the TTF of Pb by half to one order of magnitude. From 1 V to 3 V, the TTF of Sn was 100s~600s, while the TTF of Pb was 20s~200s.

J. Jung, et al [47] studied the ECM of eutectic SnPb solder in 0.001 wt% NaCl and Na2SO4 electrolyte with a 3V voltage across 0.3 mm spaced pad on a silica substrate. It was found that in NaCl solution, Pb-rich phase preferentially corroded due to a more stable layer of Sn oxide. In Na2SO4 solution, Sn-rich phase preferentially dissolved due to a more stable Pb oxide layer in it. Thermodynamically, SnO2 is more stable than SnO while PbO is more stable than PbO2.

Y. R. Yoo, et al [48] studied the ECM propensity of Sn37Pb and Sn58Bi in 0.001 wt% NaCl and Na2SO4 electrolyte with a 2V voltage across 0.3 mm on a Si wafer substrate. It was found that the resistance of ECM ranked as Sn58Bi > Sn37Pb > Sn in both NaCl and Na2SO4 electrolytes. The time to failure in both electrolytes did not differ much. For Sn37Pb solder, the migrated metal was Sn and Pb. For Sn58Bi solder, the migrated metal was only Sn. Anodic polarization test was also conducted on these solders in 0.001 wt% NaCl and Na2SO4 electrolytes. Pure Sn was easier to

dissolve than Sn37Pb and Sn58Bi. Also the dissolution behavior of these 3 solders did not show obvious differences in both electrolytes. All three solders showed passivation behaviors.

L. Hua, et al [49] studied the ECM behavior of Sn-35Bi-1Ag solder doped with Zn under THB (80C/85%RH/1~10V) conditions with a 3cm gap. It was found that for undoped Sn-35Bi-1Ag solder, Sn migrated; for Zn doped Sn-35Bi-1Ag solder, both Sn and Zn migrated. Zinc dendrites were ZnO. Potentiodynamic polarization tests were also conducted to un-doped and zinc doped Sn-35Bi-1Ag solder in 3% NaCl electrolyte. The percentage of zinc in doped Sn-35Bi-1Ag solder was from 0.2~5 wt%. It was found that the more zinc in the solder, the lower the corrosion potential, the easier for the solder to be corroded. The general conclusion was the doping of zinc into the Sn-35Bi-1Ag solder increased the ECM propensity.

S. Lee, et al [50] studied the ECM propensity of Sn-Pb solder alloys using anodic polarization in 0.001% NaCl electrolyte and water drop test (DI water) on 0.3 mm spaced Sn-Pb electrodes on silica substrate. The voltage was 2V. It was found that an increase of Pb content from 12% to 100% increased the current by almost 1 order of magnitude, and decreased the time to failure from 100 s to 25 s. Also migrated Pb was dendrite-shaped, while migrated Sn was globular filaments. In the anodic polarization, Pb had lower corrosion potential than Sn. Pb did not have passivation, but Sn did have passivation. It was concluded that the polarization was consistent with water drop test.

L. Mendes, et al [51] studied ECM of SAC305 with HASL and ENIG finishes by applying 2V or 3V across 0.1mm and 0.25 mm gaps in DI water. The substrate was

FR-4 board. It was found that the time to failure was from 10 s to 200 s for these two finishes coated solder. Finishes did not show significant effects. The main migrated metal was Sn, showing as stick like dendrites. Ag and Cu did not migrate.

Chapter 2

Evaluation of Electrochemical Migration on Printed Circuit Boards with Lead-Free and Tin-Lead Solder

Abstract

In order to evaluate the current leakage and electrochemical migration behavior on printed circuit boards with eutectic tin-lead and lead-free solder, IPC-B-24 comb structures were exposed to 65˚C and 88% relative humidity conditions under a DC bias for over 1500 hours. These boards were processed with either Sn-3.0Ag-0.5Cu solder or Sn-37Pb solder. In addition to solder alloy, board finish (organic solderability preservative versus lead-free hot air solder leveling), spacing (25 mil versus 12.5 mil) and voltage (40V versus 5V bias) were also assessed by using in situ measurements of surface insulation resistance (SIR) and energy dispersive spectroscopy after test. It was shown that an initial increase of SIR was caused by the consumption of electroactive species on the surface, intermittent drops of SIR were caused by dendritic growth, and a long term SIR decline was caused by electrodeposition of a metallic layer. The prolonged SIR decline of Sn-3.0Ag-0.5Cu boards was simulated by 3-D progressive and instantaneous nucleation models, whose predictions were compared to experimental data. Sn-37Pb boards exhibited a co-migration of Sn, Pb and Cu, while Sn-3.0Ag-0.5Cu boards incurred a co-migration of Sn, Ag and Cu. Among the migrated species, Sn always dominated and was observed as either a layer or in polyhedral deposits, Pb was the most common element found in

the dendrites, Cu was a minor constituent, and Ag migrated only occasionally. Compared to solder alloy, board finishes played a secondary role in affecting SIR due to their complexation with or dissolution into the solder. The competing effect between electric field and spacing was also investigated.

Keywords

Electrolyte, electrochemical migration, dendrite, current leakage, surface insulation resistance, reliability

2.1 Introduction

The current trend of electronic products is toward high density packaging, high circuit speeds, and high input and output counts [52]. This requires the miniaturization of electronic components and the reduction of spacing on printed circuit boards (PCBs). The typical spacings in dual-in-line (DIL) packages 20 years ago were 2.54 mm (0.1 inch) [53], but nowadays the spacings associated with some surface mount technology (SMT) circuits are between 0.1 mm and 0.25 mm (4-10 mils) [54]. This shrinkage of spacing between biased metallizations, together with moisture adsorption and contaminants on PCBs [52], can trigger an electrochemical phenomenon [55]-[59] called electrochemical migration (ECM), which is the growth of metallic dendritic structures across the gap between electrodes in the presence of moisture under a DC bias. If a dendritic structure bridges the gap, an electrical short can occur. At constant voltages, a reduction of spacing on a PCB will increase the electric field and shorten

the migration distance, which will decrease the time-to-failure and thus increase the reliability risk for electronic products.

The occurrence of ECM requires a DC voltage, an electrolyte and metal ions. The electrolyte can be either adsorbed moisture films on the substrate or condensed droplets of water. In the case of moisture adsorption, the maximum number of adsorbed monolayers of water at a certain temperature cannot be infinite. For example, at 23ºC and 100% RH, polytetrafluoroethylene can adsorb three monolayers at most, quartz can adsorb a maximum of seven monolayers [60], but for α-alumina, the maximum number of adsorbed monolayers is around 25 [61]. On PCBs at 40ºC/93% RH or 85ºC/85% RH, a typical adsorbed moisture layer is many nanometers in thickness [62]. Due to the interaction between the substrate and the adsorbed moisture, the first few layers do not behave like bulk water. Only when the number of monolayers of adsorbed moisture is above a critical value can the successive adsorbed layers start to behave as bulk water [60][61]. Migrating metal ions can originate from metallization (copper traces), finish (such as immersion tin, silver, etc.), or solder (such as Sn-Pb, Sn-Ag-Cu, or similar alloy systems).

The ECM process consists of the following sequence of steps: path formation, electrodissolution, ion transport, electrodeposition, and filament growth [63]. Path formation is the creation of a favored path—a medium consisting of an electrolyte layer for metal ions to migrate. Electrodissolution involves the oxidation of metals to generate cations at the anode. These cations tend to migrate under the influence of electromotive forces to the cathode (ion transport) and deposit there as neutral metal

(electrodeposition). As more and more neutral metals deposit on the nuclei, a dendritic structure may grow and propagate from cathode to anode (filament growth).

Typical accelerated test conditions for ECM on PCBs involve the exposure of test specimens to elevated temperature, humidity, and voltage bias (THB) levels, which are intended to reduce the time-to-failure without inducing condensation [64]. The contributions of material and processing factors to ECM in THB conditions such as conformal coating, flux, conductor spacing, and voltage bias, have been reported previously [63].

Over the past several years, lead free solder alloys have been widely used as a replacement for the traditional eutectic tin-lead solder. Although some studies have been published on the relative risk of ECM with selected lead-free solder alloys and finishes [65][66], there are few reported results from THB tests which compare tin-lead and Sn-Ag-Cu solder alloys. This paper is intended to compare the differences in electrical and electrochemical behaviors of Sn-37Pb (SnPb) and Sn-3.0Ag-0.5Cu (SAC) soldered PCBs subjected to THB exposure. The surface insulation resistance (SIR) trends and the morphologies of migrated metals were analyzed. In addition to solder alloy, board finish, electric field and conductor spacing were also investigated with respect to their contributions to ECM.

2.2 Design of Experiments

An IPC-B-24 board with interleaved comb structures was chosen and modified for this study. Since the 16 mil and 20 mil spacings used on the IPC-B-24 board have

little difference in either migration distances or electric fields given the same voltage, 12.5mil (0.32 mm) and 25mil (0.64 mm) spacings were adopted to further differentiate the spacing effects.

A typical lead-free solder, SAC solder, was chosen to compare with the traditional eutectic SnPb solder with respect to their susceptibilities to ECM. Each was reflow soldered onto copper comb structures to create samples on which the migrating species, morphologies and metallic distributions could be compared. Prior to soldering, the copper traces were finished with either organic solderability preservative (OSP) or lead-free hot air solder leveling (HASL), in order to compare a relatively low-cost organic finish (OSP) with one type of inorganic finish (HASL). Thus the comparisons included: SnPb versus SAC solder, OSP versus HASL finishes, and 0.32 mm (12.5 mil) versus 0.64 mm (25 mil) conductor spacings. Figure 1 shows the test specimens.

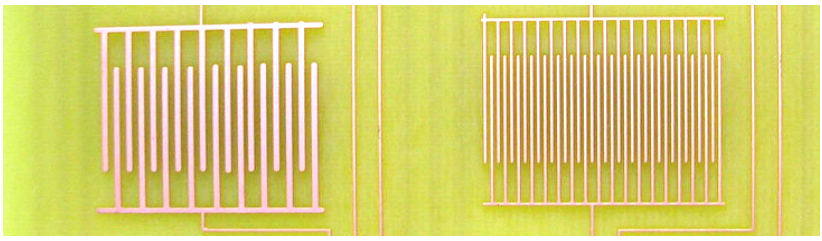

Figure 1: Image of a test board prior to soldering, containing comb structures based on an IPC-B-24 pattern, with 0.64 mm (25 mil, left) and 0.32 mm (12.5 mil, right) conductor spacings.

No-clean fluxes were used in the reflow solder paste since no-clean flux is now widely used in the electronics industry. REL0 flux was used in the SnPb solder paste

and ROL0 flux was used in the SAC solder paste. Based on the notation for solder fluxes given in IPC-J-STD-004 [67], “RE” and “RO” designate resin and rosin, respectively. “L” indicates low activity and “0” means the halide content is below 0.05% in the flux residue.

The temperature and humidity conditions (65°C/88%RH) were selected based on the recommendations of IPC-TM-650 method 2.6.14.1. Since prior studies [63] showed that testing at higher temperatures (such as 85°C) can cause the weak organic acids in no-clean fluxes to be volatilized, the choice of a higher temperature could have adversely affected the usefulness of the test results, since field conditions typically involve lower temperatures. Thus 65°C was chosen as the test temperature. The test humidity (88%RH) is within the range of humidities (85%RH~93%RH) commonly used in THB tests. While the IPC standard calls for a 500 hour test duration, longer test times were selected for this study because the major objective was to provide insights that would be of general relevance to electronic products including those with an expected life of more than just a few years, rather than simply qualifying a candidate process to a minimum requirement. The actual test durations were 1653 hours for the 40V test and 1550 hours for the 5V test. The voltage biases selected were 40V and 5V DC so as to cover a range of voltages that may be used in power lines and signal lines. The SIR failure threshold was 100 MOhms, which was consistent with the criteria cited in IPC J-STD-004A method 3.4.5.1 and IPC-9201. For each combination of experimental factors, 3 identical test comb structures were

tested, so in total 24 comb structures were tested at each of two voltages. Table 1 provides an overview of the test matrix.

Table 1 THB Test Board Characteristics and Process Factors

Solder alloy	SnPb, SAC
Solder process	Reflow
Board finish	OSP, lead-free HASL
Conductor spacing	0.32 mm (12.5 mil), 0.64 mm (25 mil)
Voltage bias	5V, 40V
Flux (no clean)	ROL0 for SAC, REL0 for SnPb
Substrate	FR-4 (170 °C glass transition temperature)
Replicates	3
Environment	65°C/88%RH (non-condensing)
Duration	1653 hours for 40V, 1550 hours for 5V

An SIR test system was used to detect leakage current. The SIR test system comprised a computer, a high resistance meter, low noise switches, a temperature-humidity chamber, a DC power supply, triax cabling, and the test boards. The multichannel high resistance meter was an Agilent 4349B with a measurement range from 10^3 Ohms to 10^{15} Ohms. Its accuracy ranges from 2.5% to 3.1%. Agilent E5252A low noise switches provided the ability to multiplex 48 channels to the resistance meter, allowing an SIR reading to be collected once every 3.6 minutes for each comb pattern. A 1-megohm current limiting resistor was placed in series with each comb pattern in order to minimize the fusing of dendrites in the event of a drop in SIR, while still

providing the opportunity to observe SIR behavior over about 4 orders of magnitude in resistance.

2.3 Results and Discussion

The times to failure of SIR data collected during the THB tests (40V and 5V) are shown in Tables 2 and 3.

Table 2: Times to Failure for Comb Structures at 65ºC/88% RH/40V

Solder	Finish	Spacing (mil)	Time to Failure (Hours)		
			Sample 1	Sample 2	Sample 3
SnPb	OSP	25	s	s	s
		12.5	**1313.8**	**0**	**195.7**
	HASL	25	s	s	s
		12.5	**1.4**	**9.4**	s
SAC	OSP	25	**1063.4**	s	**888.6**
		12.5	**85.6**	**87.3**	**91.3**
	HASL	25	**706.3**	**257.8**	**1365.9**
		12.5	**117.6**	**134.4**	**101.7**

2.3.1 SIR Behavior of Solder Alloy: SnPb vs. SAC

The experimental results (Tables 2 and 3) reveal that the SnPb boards consistently incurred fewer failures than the SAC boards. The switch from 40V to 5V led to an appreciable decrease in the number of failures on the SnPb boards, while this switch did not greatly affect the number of failures on the SAC boards. Given the same finish

or spacing, the number of failures of the SnPb boards was always lower than that on the SAC boards. In addition, the times to failure of the SnPb boards had greater variability compared to the more narrowly distributed times to failure of SAC boards, when the same finish and spacing were considered.

Table 3: Times to Failure for Comb Structures at 65ºC/88% RH/5V

Solder	Finish	Spacing (mil)	Time to Failure (Hours)		
			Sample 1	Sample 2	Sample 3
SnPb	OSP	25	s	s	s
		12.5	s	s	s
	HASL	25	s	s	s
		12.5	**234**	s	s
SAC	OSP	25	s	s	s
		12.5	**432.1**	**539.8**	**353.9**
	HASL	25	s	**900**	**871.9**
		12.5	**423.6**	**273.3**	**409.6**

Note: “s” means survived.

The SIR trends between SnPb soldered and SAC soldered samples were different, as shown in Figures 2 and 3. The SIR of the SnPb samples shows an increasing trend in the beginning of the test followed by a gradual leveling off. The SIR of the SAC samples, however, shows a long-term decline after increasing for an initial period of about 100 hours. This phenomenon occurred for all SnPb and SAC boards in both 40V and 5V THB tests, regardless of which types of finish and spacing were used.

The long-term behavior of SnPb and SAC boards can be explained as follows. Initially after the humidity and bias were applied, the adsorbed moisture films on the FR-4 laminate surface combined with flux residues and ionic contaminants on the surface of PCBs and built up an electrolyte. Flux residue contains organic salts (fluxing product) and weak organic acids (remaining flux activators) such as adipic and glutaric acids, which are the common activators of no-clean flux. Together with the DC bias between electrodes, an electrochemical cell was formed.

Analysis of SIR curves of surviving SnPb samples shows that the relationship between SIR, *R,* and time, *t,* follows a power law formula $R = at^n$, where *a* is a constant. Averaged *r-square* values, a measure of the goodness of fit, were 0.98 for 40 V SIR curves and 0.92 for 5 V SIR curves, indicating that the fits were good. The *n* values of 40V stressed samples ranged from 0.40 to 0.67, with a mean of 0.52. The *n* values of 5V stressed samples ranged from 0.43 to 0.72, with a mean of 0.61. A *t-test* (statistical hypothesis test) was conducted and it was found that there was no statistical difference between the means of these two groups of *n* values when a significance level of 5% was applied. Thus it is unlikely that *n* is voltage dependent. Taking into account the experimental statistical uncertainties, it is most likely that the mean value of *n* is between 0.5 and 0.6. This suggests that the SIR of the comb structure is approximately proportional to the square root of time, which is a typical characteristic of a diffusion-controlled ion transport process under a constant voltage [68][69].

The initial SIR increase on SnPb boards implies an initial current decay with time. Surface current decay on a polymer under a constant voltage has been investigated for

several decades. The polymers studied include epoxy resin [70][71], polytetrafluoroethylene [60], polyethylene [72], polypropylene [73], poly (hexafluoropropylene-tetrafluoroethylene) [75], etc. The relation between the current *I*, the so-called "absorption current", and time *t* is described as $I \propto t^n$. When the polymer is tested in vacuum, *n* is close to -1, and when in air, *n* is between -0.6 and -0.8 [73][74][75]. Thus the absorption current decays more slowly in air than in vacuum. The explanations for this absorption current decay include lateral spread of surface charges in vacuum [74], polymer surface polarization [76], charge injection [77], and electrons hopping across surface localized states [78]. The polymers mentioned above are cleaned polymers, but for epoxy resin, especially with ionic contaminants on the surface, this current decay has been attributed to a diffusion-controlled process and analyzed in the *frequency* domain [70]. Unfortunately, the origin of charge carriers has not been exactly specified. The charge carriers can be electrons [78], most likely in vacuum, but in air when moisture adsorption takes place it is generally accepted that the charge carriers bear an ionic nature [70] [71] [72] [73] [77].

Since surface conductivity of a polymer exposed to water vapor is always several orders of magnitude higher than that in a vacuum, most likely the charge carriers with moisture adsorption present are ions. So the resistance-time transient response to a constant bias *U* based on ion transport in a cell is

$$R = \frac{U}{i_{Total} A} = \frac{U}{\sum_{1}^{k} (z_i F c_i^b (a-1) \sqrt{\frac{D_i}{\pi t}}) A} = \frac{U}{\sum_{1}^{k} (z_i F c_i^b (a-1) \sqrt{\frac{D_i}{\pi}}) A} \sqrt{t} \qquad (1)$$

where A is the cross-sectional area of the electrolyte, i_{Total} is the total current density, z_i is the charge number, F is the Faraday constant, c_i^b is the initial bulk concentration of a specific type of electroactive ion, a is a constant set by the system, D is the diffusivity, and t is time. A detailed derivation of Equation 1 is given in the appendix.

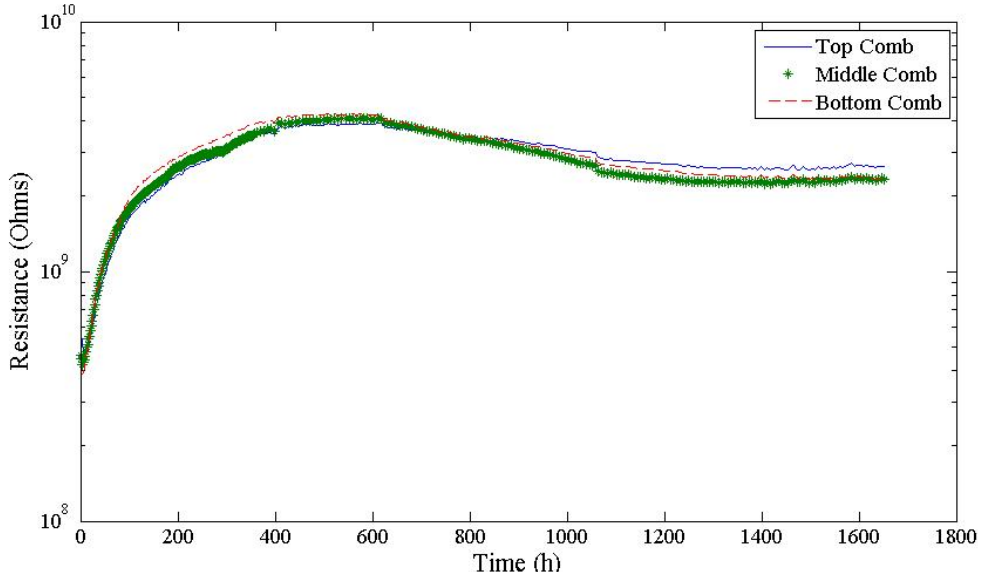

Figure 2: 40V SIR of 3 comb structures on a SnPb soldered board with HASL finish and 25mil spacing.

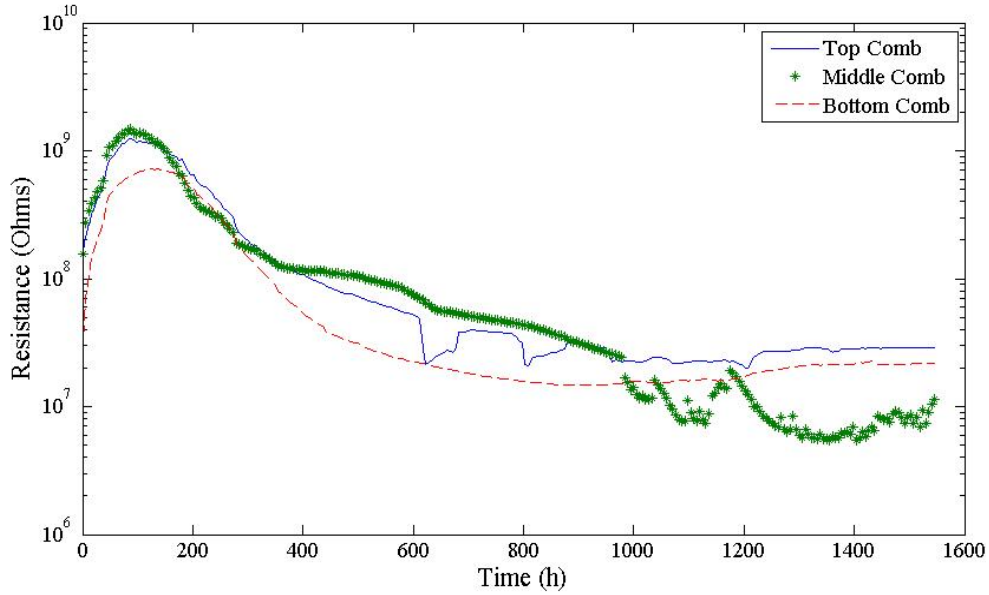

Figure 3: 5V SIR of 3 comb structures on a SAC soldered board with OSP finish and 12.5-mil spacing.

From Equation 1 we can see that $R \propto t^{0.5}$ since z, F, a, D, A, and c_i^b are all constants, because the types and initial amounts of the electroactive species such as ionic contaminants were fixed after the start of the THB test. So in the initial period of time, such as the first 600 hundred hours in Figure 2, the flux residues and ionic contaminants present on the surface of the board migrated toward the electrodes, where they were oxidized or reduced and thus consumed. Since their initial amounts on the surface were limited and fixed, their consumption on the surfaces of the electrodes created a depletion region in the vicinity of the electrodes, thus expanding the diffusion layer thickness into the bulk electrolyte with time. As more and more residues or contaminants were consumed, their concentrations in the vicinity of the electrodes decreased further, and ionic *migration* (see Appendix) proportional to concentration decreased more and more. Ionic *diffusion* finally dominated the ion transport process on the board surface. This is true if no significant amount of metals dissolve, since the dissolution of metal can introduce new electroactive ions into the system and perturb the composition of the ionic flux, thus significantly changing the current density. On most of the survived SnPb soldered boards, little dendritic growth occurred, thus corroborating the assumption that existing flux residues and contaminants were the *only* available electroactive species in the cell.

In contrast, the SAC board did not grow dendrites, but exhibited the deposition of layers, as shown in Figures 4 and 5. In the figures, energy dispersive spectroscopy (EDS) maps show that migrated Sn has formed a continuous layer spreading across

the gap. This indicates that electrocrystallization into a layer or film-like deposit rather than dendrites, corresponding to a nucleation and growth model, occurred.

The current-time transients of electrocrystallization in an electrochemical cell under a constant voltage have been investigated previously [79][80][81]. Armstrong (1966) [79] introduced a three dimensional nucleation and growth model using lattice incorporation and described the current-time transient to a constant DC bias (as in a potentiostat) in growing deposits of layers. For progressive 3D nucleation, where nucleation and growth of the lattice occur at the same time, the current density is

$$i = zFk_1(1 - \exp(-\frac{\pi M^2 \gamma k_2^2}{3\rho_d^2} t^3))$$

and thus the resistance is

$$R = \frac{U}{zFk_1(1 - \exp(-\frac{\pi M^2 \gamma k_2^2}{3\rho_d^2} t^3))A} \quad (2)$$

For instantaneous 3D nucleation, where nucleation stops and growth of the lattice continues on the initially grown nucleation centers, the resistance is

$$R = \frac{U}{zFk_1(1 - \exp(-\frac{\pi M^2 k_2^2 N_0}{\rho_d^2} t^2))A} \quad (3)$$

where k_1 and k_2 are the growth rate constants perpendicular and parallel to the substrate, respectively. M is the molecular weight, γ is the nucleation rate constant, N_0 is the saturation density of nuclei centers, ρ_d is the deposit density, U is the bias, t is time, and A is the cross-sectional area for the electrolyte.

Equations 2 and 3 indicate that R decreases with time and finally reaches a plateau. The final plateau is determined by k_1, the perpendicular growth rate, since the exponential terms related to k_2 and t decay with time. This suggests that as more and

more layers of deposits form at the cathode, the deposition front advances toward the anode, so the current density increases with time and the resistance decreases but eventually approaches a steady state set by k_1, the perpendicular growth rate. A simulation of the resistance-time transient based on Equations 2 and 3 can be made by assuming appropriate nucleation and growth rate constants for tin ions, as shown in Figure 6. The curves in the figure were obtained under the assumptions that the electroactive species is Sn^{2+}, $k_2^2\gamma = 3\times10^{-22}$ mol^2 nuclei cm^{-5} s^{-3}, $k_2^2N_0 = 3\times10^{-17}$ mol^2 nuclei cm^{-5} s^{-3}, $k_1 = 2.2\times10^{-7}$ mol cm^{-2} s^{-1}, and voltage bias U=5 V. The adsorbed water layer is assumed to have a thickness of 100 nm [62] and a length of 12 mm (the length of the fingers of the comb structures), so the cross sectional area is $A=1.2\times10^{-5}$ cm^2. Note that after 100 hours, the simulated SIR curves show a long term decline, matching the experimental data. Although it is hard to determine which type of nucleation (progressive or instantaneous) occurred on the SAC board, these two nucleation and growth models show similar SIR trends and most likely, both types of nucleation occurred. Both the degree of matching between the SIR and the model, and the correspondence of the morphology to the model, lead to the conclusion that the SAC board experienced metal migration and deposition on the cathode as layers rather than dendrites, which generated a long term SIR decline.

The differences in SIR behavior between SnPb and SAC boards may be caused by flux chemistry and their long-term compatibilities with solder. Both the SnPb and SAC boards contained a significant amount of flux residues before the THB tests, and flux residues spanned the gap in some places on both types of boards. The flux

residues on the surface are designed to either react with water vapor or oxygen, or react at electrodes through redox reactions so that the ionic constituents of the cell are depleted with time and thus the SIR increases to a relatively high steady value, a sign of SIR recovery. The degradation of flux residue caused by reactions between water vapor and flux or fluxing product is a diffusion controlled process [82] characterized by the diffusion of water through the outer layer of degraded flux residue to react with the inner material. Thus the liberation of electroactive species may also be diffusion controlled, since free ions have to diffuse from inside through the outer layer of degraded flux residue to become electroactive. Either the release of electroactive species from the degraded flux residue or the consumption of electroactive species at electrodes can place the circuit under diffusion control. This is why the surviving SnPb boards without significant metal migration showed an initial diffusion controlled SIR behavior. If for some reason, the flux residue on the surface is not compatible with the solder in the long run, SAC solder in this case, it may complex with the solder and trigger the electrochemical migration of metal ions, whose deposition as layers rather than dendrites can give rise to a long term SIR decline. This suggests that a flux which passes standard tests (for example, 168 hours at 85°C/85%RH, 96 hours at 35°C/85%RH, or 96 hours at 65°C/85%RH, all under bias) may not necessarily pass a THB test of more than 500 or 1000 hours.

Dendritic growth was responsible for most of the SIR failures of the SnPb boards. The dendritic growth bridging the gaps between electrodes (Figures 8 and 9) was always accompanied by intermittent SIR drops, as shown in Figure 7. During dendritic growth, dendrites can break due to fusing [83] or mechanical stress [84], but rapid regrowth can occur [84]. This breaking and regrowth may cause the SIR to oscillate in a cyclic fashion and thus show intermittent drops. This is consistent with previous reports [62][85] on this phenomenon.

2.3.2 Morphology of Migration: SnPb vs. SAC

The morphology of electrodeposits at the cathode is affected by various factors such as the overpotential (the potential difference between the potential applied to the electrode and the potential of the electrode at equilibrium) of the cathode, current density, adhesion of nuclei to electrodes, electrolyte viscosity, and temperature. When the overpotential is small, a spongy or porous deposit can occur. When the overpotential is increased, the nucleation rate is increased, and a polycrystalline layer structure results. If the overpotential or the current density is larger than the critical values, a dendritic structure can be provoked to grow [86].

As shown in Figures 4 and 5, diffuse layer deposits formed on the failed SAC boards. Among the migrated species, Sn always dominated, Cu concentration was always less than Sn, and Ag was present in only small quantities and only occasionally. On failed SnPb boards, typical dendrites occurred in the 40V THB tests (Figures 8 and 9), and polyhedral or layer-like deposits emerged in the 5V testing (Figure 10). Migrated Sn,

Pb, and Cu co-existed in either dendrites or polyhedral deposits. In dendrites Pb dominated, while in the polyhedral deposits Sn dominated. Taking into account both dendrites and polyhedral deposits, Sn was still the predominant migrated species under most cases, Pb was less prevalent than Sn, and Cu was present in small proportions.

Apparently, a co-migration of Sn, Pb, and Cu on the SnPb board and Sn, Cu, and Ag on the SAC board occurred. Since typical cathodic overpotentials for electro-deposition of these metals are less than 1 V [87][88][89], 5 V and 40 V are high in an electro-deposition sense. Assuming that the deposits were a mixture of metals in their pure states rather than solid solutions or chemical compounds, a 5V or 40V bias provided enough margin to accommodate the required cathodic overpotential for deposition of these metals, although the voltage drop across the surface-adsorbed film electrolyte can be significant [62]. That is why all these metals co-migrated. The reason why Pb was predominant in the dendrites may be due to the higher solubility of Pb^{2+} than Sn^{2+} by almost 3 orders of magnitude [90], making it easier for the flux of Pb^{2+} to exceed the critical current density to trigger dendritic growth. The dominance of Sn in the overall migrated species may be due to its larger proportion in eutectic SnPb solder or SAC solder, though it had to deposit as layer structures due to the low solubility of Sn^{2+}. The reason for the occurrence of dendrites on the SnPb board in the 40 V tests was that the chance for cathodic overpotentials in the 40V test to exceed the critical cathodic overpotential needed to trigger dendritic growth was much higher than in the 5V test.

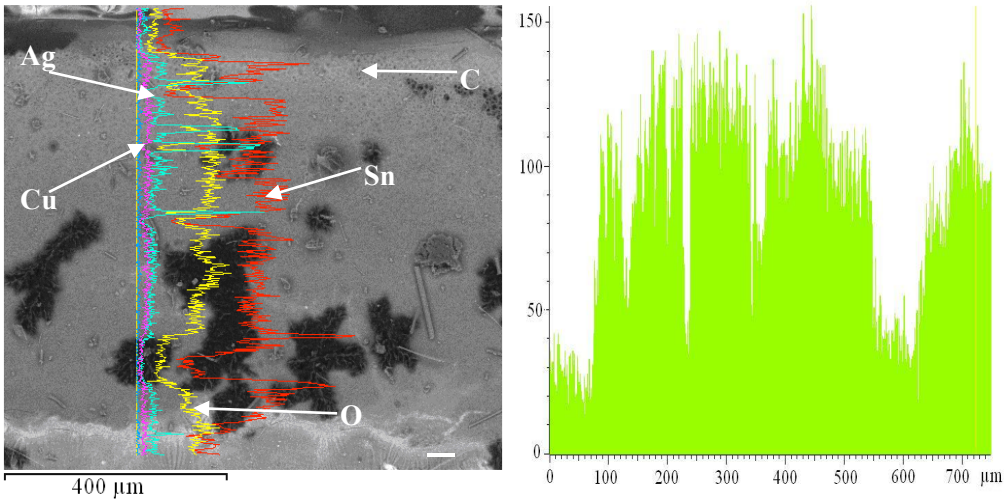

BSE Sn

Figure 4: An EDS line scan of materials existing in the gap on SAC-soldered board with OSP finish and 25 mil spacing after 40V THB test. The left graph is the original back scattered electron (BSE) image, and the right graph is the Sn distribution along the line scan from the top to the bottom.

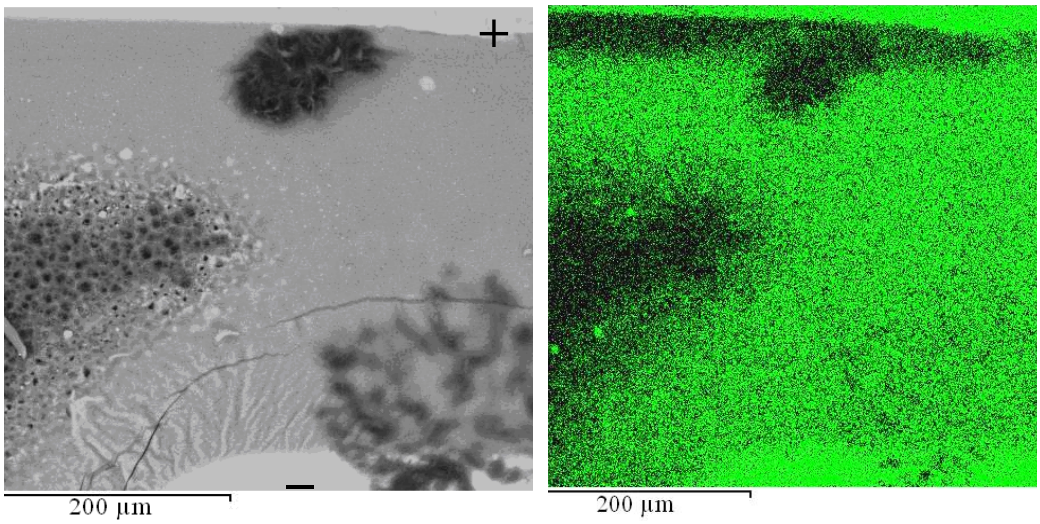

BSE Sn

Figure 5: An EDS map of a 12.5 mil sample on the SAC-soldered board with HASL finish after a 5V THB test. The left graph is the original BSE image, and the right graph is the Sn distribution spanning the gap as a layer deposit.

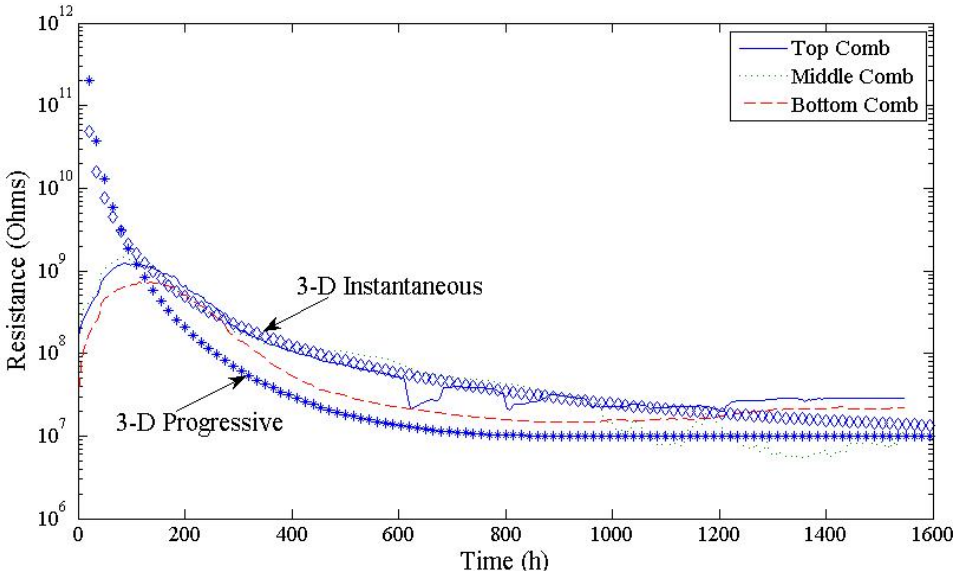

Figure 6: A simulation of resistance with time based on Equations 2 and 3. The two simulated curves, for 3-D progressive and instantaneous nucleation, are shown together with the experimental curves from Figure 3.

2.3.3 Effect of Board Finish: OSP vs. HASL

Finishes are used to retard the oxidation of bare copper on PCBs and maintain the solderability of metal surfaces. OSP is an organic layer evenly deposited onto exposed copper metallizations. The coating of OSP, made from benzimidazole, can be 200~500 nm thick and more durable than the previous benzotriazole version [91]. HASL involves passing boards over molten solder and blowing off excess molten solder by a hot air knife, thus leaving a thin solder layer over the exposed copper metallization. The thickness of the HASL layer can be up to several hundred micrometers with large variations [92]. But OSP is more prone to physical damage during PCB handling, and it can partially dissolve in solvents including water [91].

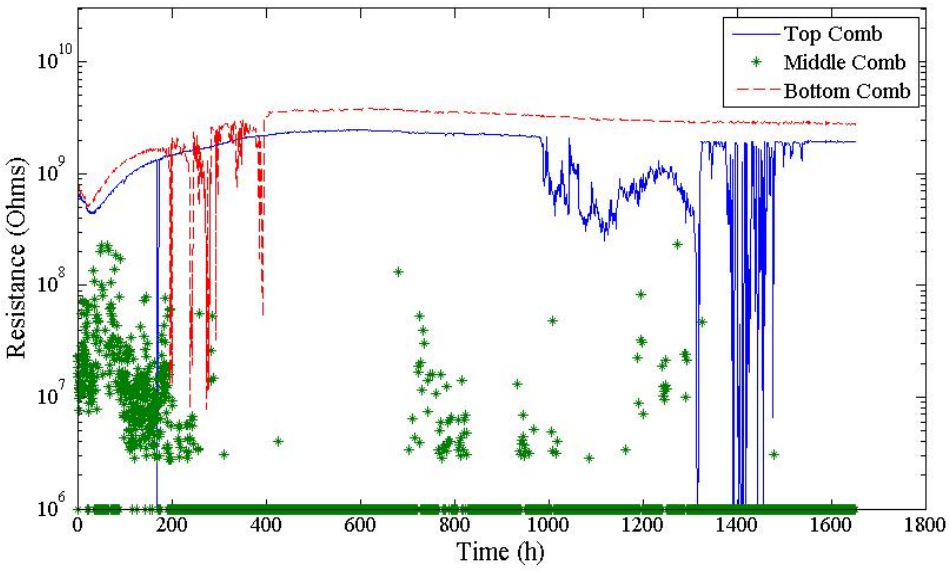

Figure 7: 40V SIR of 3 comb structures on a SnPb soldered board with OSP finish and 12.5 mil spacing.

In the present study, OSP and HASL finishes did not show noticeable differences in their effect on SIR. This can be concluded from statistical analysis such as the Weibull analysis in Figure 11 showing substantial overlap of the 90% confidence intervals. All boards using the same solder always showed similar SIR trends, regardless of whether OSP or HASL was used. One particular phenomenon was that OSP-finished SAC boards generated green residues, though their SIR trends were still similar to HASL-finished SAC boards.

Green residues may result from the reaction between remaining OSP and fluxing products. Benzimidazole, with a melting temperature of 170ºC-172ºC [93], may not completely evaporate during the reflow process. A green copper complex can form from the reaction between benzimidazole HL ligand and copper sulphate at 60ºC [94]. So it is possible that the remaining OSP reacted with fluxing products (copper organic salts) and formed green residues during THB testing (65ºC, 88%RH). The similar SIR

trends with and without green residues suggest that green residues are non-detrimental to SIR and have high resistances, thus confirming the findings of Tellefsen [95]. HASL finish can dissolve into solder during the soldering process, and therefore plays a secondary role in affecting ECM compared to solder. Thus neither finish contributed measurably to the SIR result.

2.3.4 Effect of Electric Field and Spacing

Electric field acts as the driving force for ion migration. This driving force together with the relaxation effect and electrophoresis effect determines the migration velocity of ions. The relaxation effect is the overall backward drag from an ion's ionic cloud when the ion moves forward, while electrophoresis stems from the collision between ions' hydration sheaths when they move [69]. Therefore, a higher ion migration speed results from a higher electric field, a higher ionic mobility, a lower electrolyte viscosity, and a smaller ionic radius (including the sheath of the ion). The spacing determines the travel distance for ions to reach the cathode and thus affects the migration time. A smaller spacing also increases the probability for flux residues or surface contaminants to bridge the gap between electrodes, allowing moisture to adsorb and form a continuous electrolyte medium (the ECM step of path formation).

Table 4 shows the times-to-failure of different boards with respect to four electric fields. At each value of electric field, four types of boards with the same spacing were combined into one group and the characteristic life of this group was calculated based on Weibull statistics. By doing so, four representative points were generated and

plotted in Figure 12. One can observe that given the same spacing, a larger electric field led to a shorter characteristic life. The combination of a larger spacing and a smaller electric field resulted in the longest characteristic life. But a larger spacing under a higher electric field (point 2) still led to a longer characteristic life than did a smaller spacing under a lower electric field (point 3). This comparison not only suggests that spacing itself is an independent factor affecting ECM, which is consistent with the findings of Zhan, et al. [63], but it also means that a larger spacing can overcome the disadvantageous effect induced by a larger field and still lengthen the characteristic life under some conditions. A further analysis that shows the strong effect of spacing is given in Figure 13, which shows that a larger spacing can lengthen the characteristic life independently of electric field.

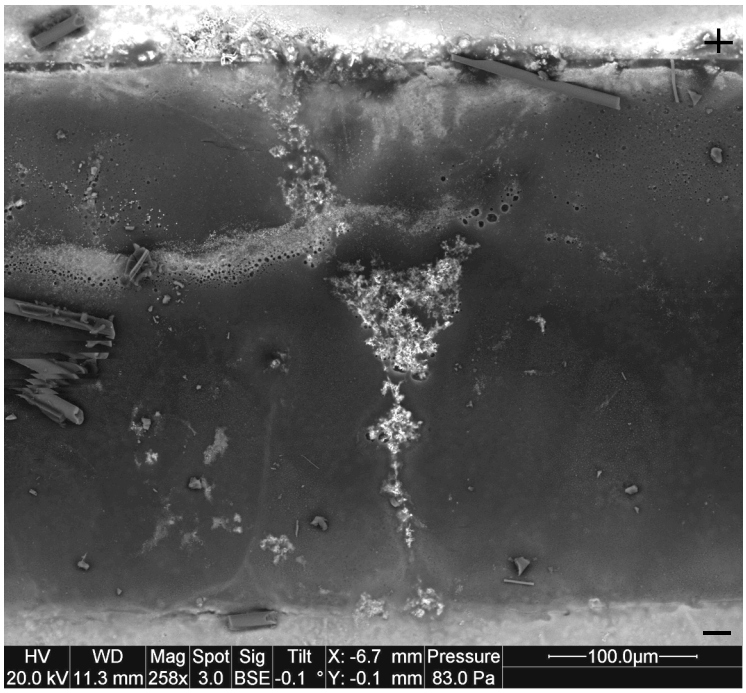

Figure 8: A dendrite spanning the gap on a SnPb-soldered board with OSP finish and 12.5 mil spacing after a 40V THB test.

Table 4 Times to Failure (Hours) of SIR According to Electric Field and Board

	(5V, 25mil) **0.2 V/mil**	**(5V, 12.5mil)** **0.4 V/mil**	**(40V, 25mil)** **1.6 V/mil**	**(40V, 12.5mil)** **3.2 V/mil**
SnPb_OSP	s/s/s	s/s/s	s/s/s	1313.8/0/195.7
SnPb_HASL	s/s/s	234/s/s	s/s/s	1.4/9.4/s
SAC_OSP	s/s/s	432.1/539.8/353.9	1063.4/s/888.6	85.6/87.3/91.3
SAC_HASL	s/900/871.9	423.6/273.3/409.6	706.3/257.8/1365.9	117.6/134.4/101.7

Note: "s" means it survived the test.

2.3.5 Main Effects and Interaction Effects

The main effects and interaction effects of this 2^4 (4 factors, 2 levels) full factorial experimental design were extracted using analysis of variance (ANOVA). It was found that greater insight into SIR response could be obtained by replacing voltage bias with electric field as a factor in the analysis. Based on the times to failure in Table 4 and assuming the failure times for the survived samples are just the termination times for the THB tests, the main effects plot and interaction plot were generated, as shown in Figures 14 and 15. It can be observed that solder alloy and spacing are the two dominant factors since the lines connecting their data points have steep slopes, showing larger variations from the grand mean (1000 hours in this case). The electric field also shows significant influence on the SIR response. It has a similar

pattern as Figure 12. The finish, however, does not show much influence and plays an insignificant role.

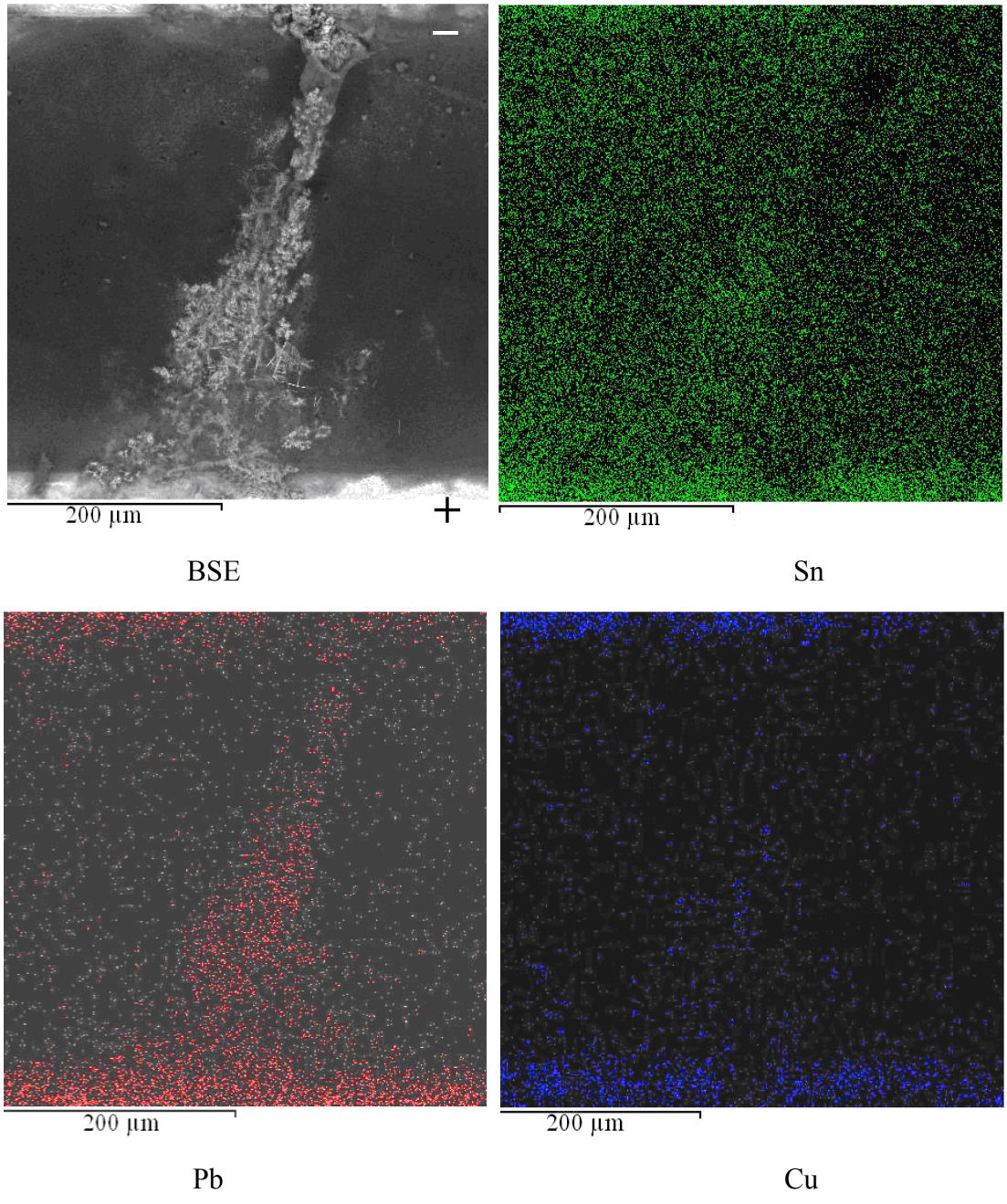

Figure 9: A dendrite spanning the gap on a SnPb-soldered board with OSP finish and 12.5 mil spacing after a 40V THB test.

In an interaction plot, the more parallel the lines, the less interaction between the factors. The interactions between any two of these four factors, however, are not pronounced since their lines are all more or less parallel to each other, as shown in Figure 15. The interaction between the electric field and spacing can not be determined from the plot due to the lack of a complete set of electric fields with one spacing, or vice versa, but their competition is discussed in the next section.

2.3.6 Risk Index Discussion

The observation of metal migration by itself represents a risk factor for electronic products. One way to evaluate the combined effect of metal migration and SIR degradation is to assess the metal migration and SIR with numerical values and combine them to form a risk index. The criteria are given in Table 5. The final index is the sum of the risk indices of metal migration and SIR. The SIR index is the sum of the indices of the initial SIR right after temperature and humidity exposure, the SIR at 1000 hours, and the final SIR of the THB test with 20%, 30%, and 50% weights associated with them, respectively.

The differences among solder alloys, finishes, and spacings with respect to their risk indexes are compared using statistical tools including fitting of distributions, means of samples, and confidence intervals. The smaller the risk index, the lower the risk associated with ECM and SIR, and the higher the reliability. From Figures 16 and 17, it can be observed that SnPb solder has a large percentage of samples with risk indices close to zero, with its best fit being an exponential distribution. The risk index data for

the SAC solder is more scattered and its best fit is a Weibull distribution. The risk index for SnPb has a significantly smaller mean than that for SAC. OSP and HASL finishes show similar influence since they belong to the same best fit-exponential distribution and have similar means and confidence intervals, as shown in Figure 18.

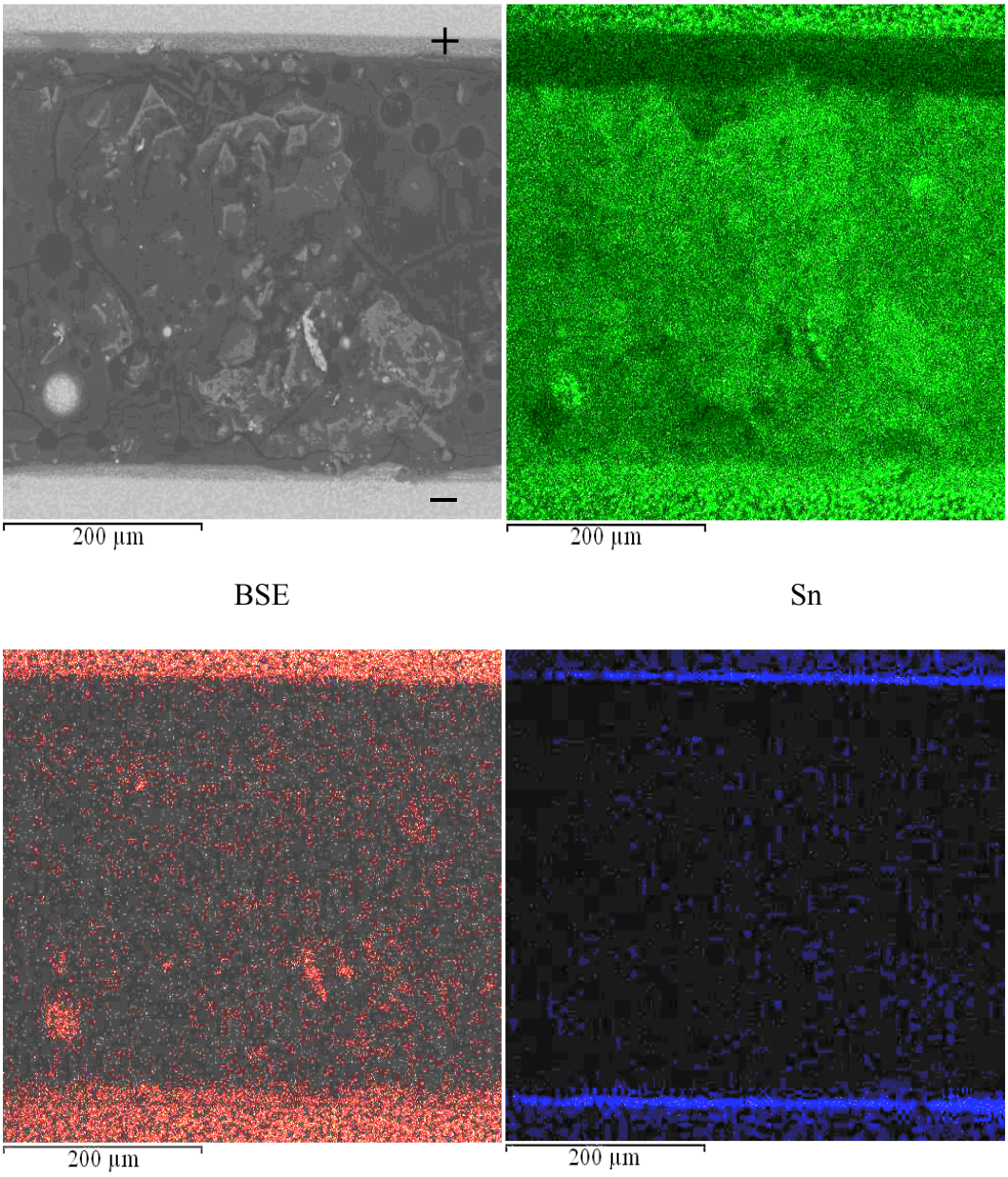

Figure 10: Migrated metal in the shape of bumps or polyhedra on SnPb-soldered board with HASL finish and 12.5 mil spacing after 5V THB test.

The intervals of the risk index are plotted in Figure 19 against an ascending series of electric fields, with an indication of their associated spacings. It can be observed that given the same spacing, an increase in electric field increases the mean of the risk index, though this increase for 12.5 mil samples is more appreciable than for 25 mil samples. Focusing on a comparison between groups II (0.4V/mil, 12.5 mil) and III (1.6 V/mil, 25 mil), it may be expected that an increase of electric field by 4 times would increase the risk index. However the mean of the risk index actually decreases. This suggests that the doubling of the spacing suppressed the increased risk resulting from the increase of the electric field by 4 times. The risk index decreased from 3.60 to 1.47, which implies a stronger and independent influence of spacings on risk, pointing to the importance of the path formation step in the ECM process.

A further exploration can be performed to clarify which factor—spacing or electric field—is more influential in determining the risk index, as shown in Figure 19. Let asterisk "A" represent an imaginary group of 25 mil samples with a 0.4 V/mil field. So a transition from $I \rightarrow II$ can be viewed as $I \rightarrow A \rightarrow II$. The increase of risk index from group I (25 mil, 0.2 V/mil) to group III (25 mil, 1.6 V/mil) is 28%, so the transition from I to A (double the field) cannot increase the risk index by more than 28%. The transition from I to II (double the field and half the spacing) increased the mean of the risk index by 213%, thus suggesting that the transition from A to II (half the spacing) has potentially increased the risk index by 185%. Thus under a relatively low electric field (less than 0.4 V/mil), a change of spacing by 2 times has a more significant effect on the risk index than a change of electric field by 2 times.

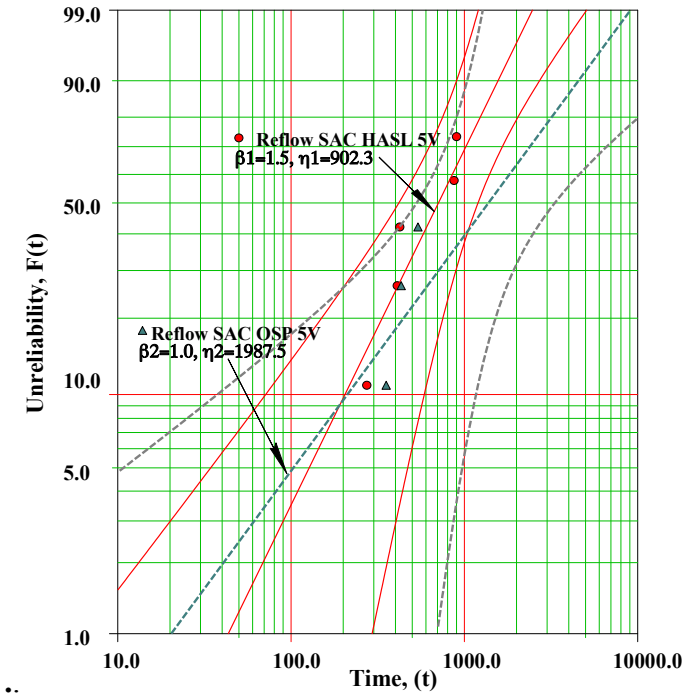

Figure 11: Weibull plot comparing SAC soldered samples with OSP (dashed lines) and HASL finishes (solid lines) from 5V THB test with 90% confidence intervals (CI).

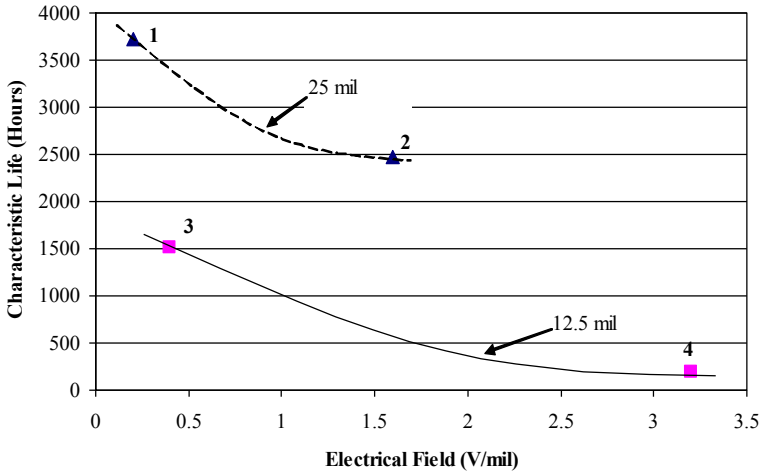

Figure 12: Characteristic lives of four groups: 1 (0.2V/mil, 25mil), 2 (1.6V/mil, 25mil), 3 (0.4V/mil, 12.5mil) and 4 (3.2V/mil, 12.5mil). The dashed and solid curves are for illustration purposes only.

Similarly, let "B" represent an imaginary group of 12.5 mil samples with a 1.6 V/mil field. So a transition from $IV \rightarrow III$ can be viewed as $IV \rightarrow B \rightarrow III$. The transition from IV to B (half the field) decreases the risk index by no more than 44%, which is the decrease of risk index from group IV to II (reduction of the field to one eighth of the original value). But the decrease of risk index from group IV to III (half the field and double the spacing) is 76%, so a change from B to III (double the spacing) can decrease the risk index by more than 32%. This implies that under a relatively high field (higher than 1.6 V/mil), a change of spacing by 2 times is comparable to a change of electric field by 2 times in its effect on the risk index.

Together with the comparison between groups II and III discussed previously, it may be concluded that when the electric field is less than 1.6 V/mil, spacing dominates the risk index, but when the electric field is larger than 1.6 V/mil, the electric field and spacing exert similar influence on the risk index.

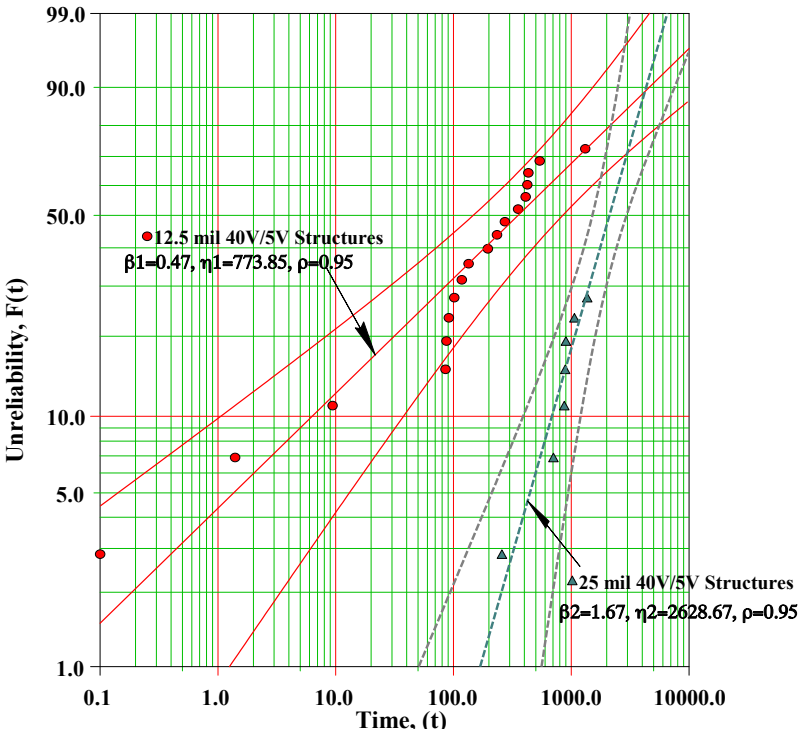

Figure 13: Comparison between all 25 mil samples (dashed lines) and 12.5 mil samples (solid lines) from 40V and 5V THB tests with 90% CIs.

Table 5 Risk Index Criteria According to Metal Migration and SIR Degradation

Dendritic Growth (More than 20% of Conductor Spacing) or Migrated Metal Spanning the Gap	Risk Index of Metal Migration	SIR Degradation	Risk Index of SIR
None	0	$>10^8$ Ohms	0
Less than two places	1 or 2	$>10^7$ Ohms	1
Few or some places	3 or 4	$>10^6$ Ohms	2
Many places	5 or 6	$=10^6$ Ohms	4

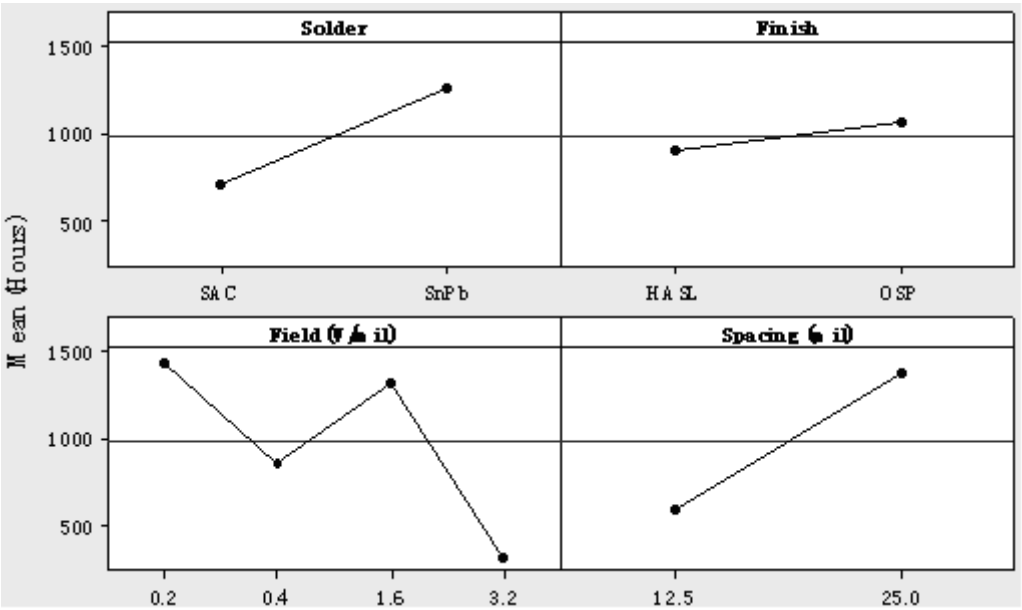

Figure 14: Main effects plot for times to failure based on Table 4.

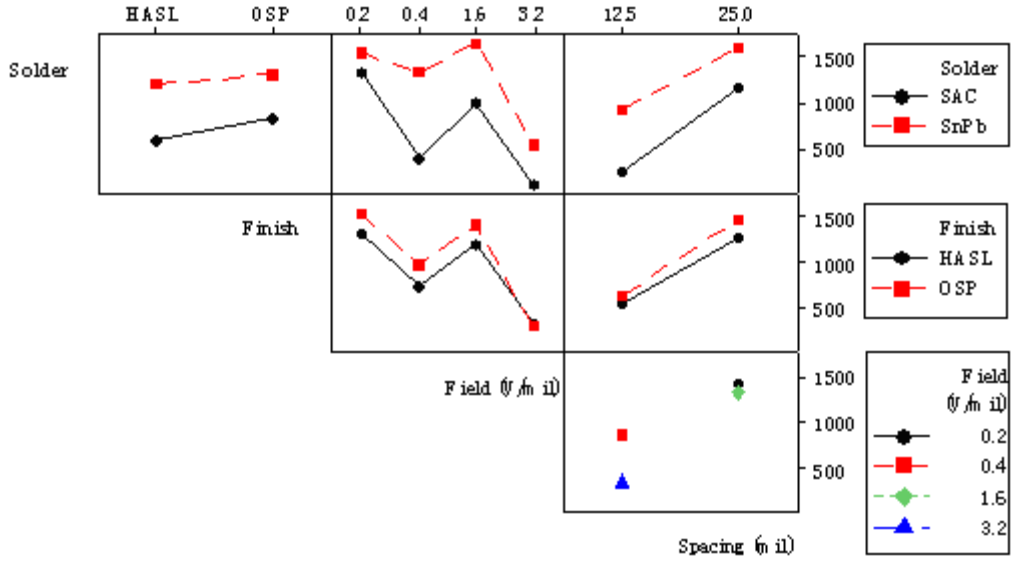

Figure 15: Interaction plot for times to failure based on Table 4.

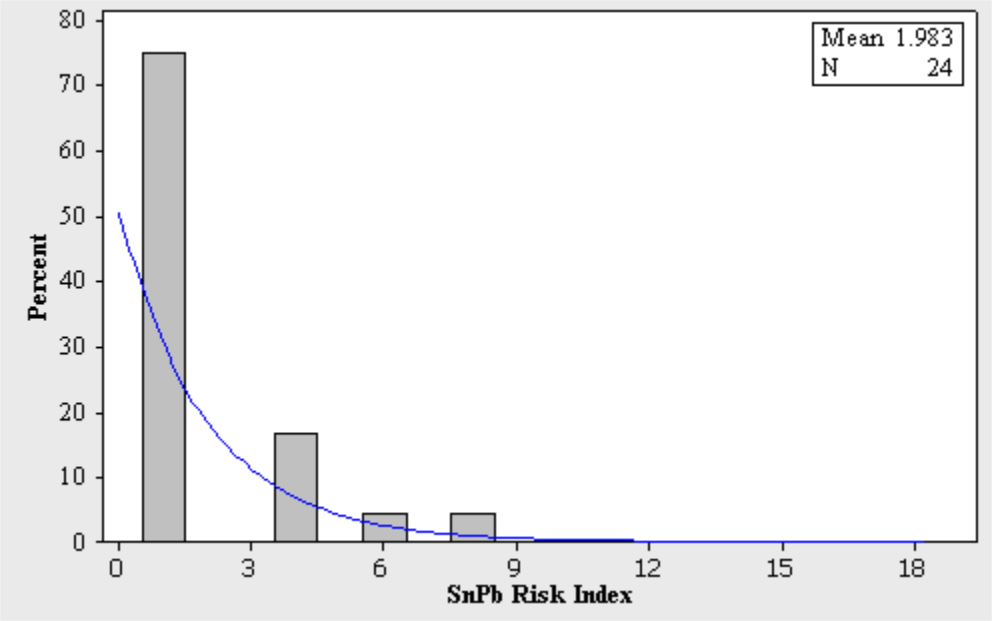

Figure 16: Histogram of SnPb risk index based on the best fit-exponential distribution, with a mean of 1.98, sample size of 24, and a 95% CI of (1.33, 2.96).

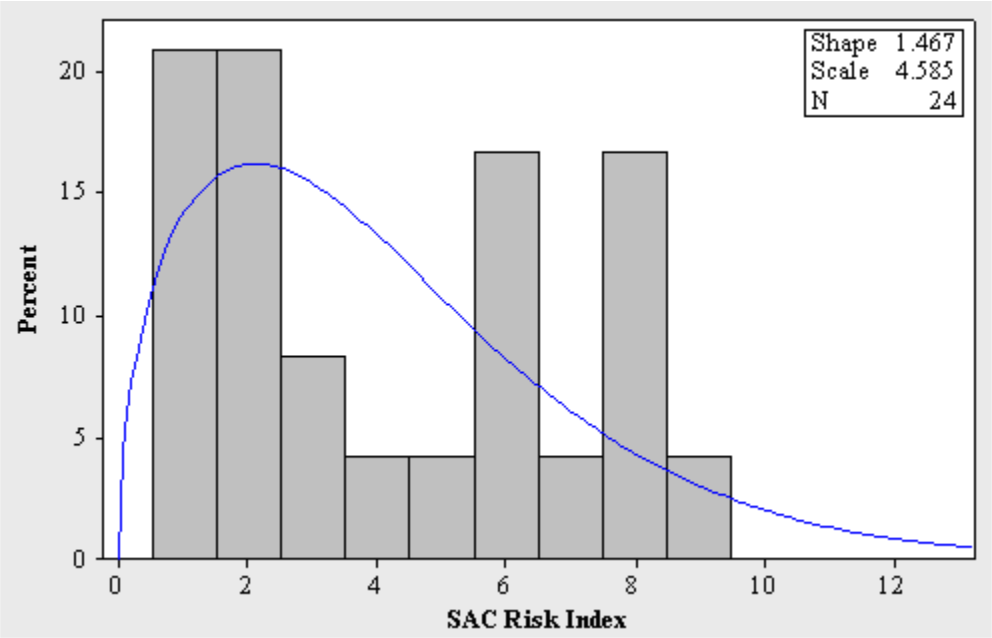

Figure 17: Histogram of SAC risk index based on the best fit-Weibull distribution, with a mean of 4.15, sample size of 24, and a 95% CI of (3.15, 5.47).

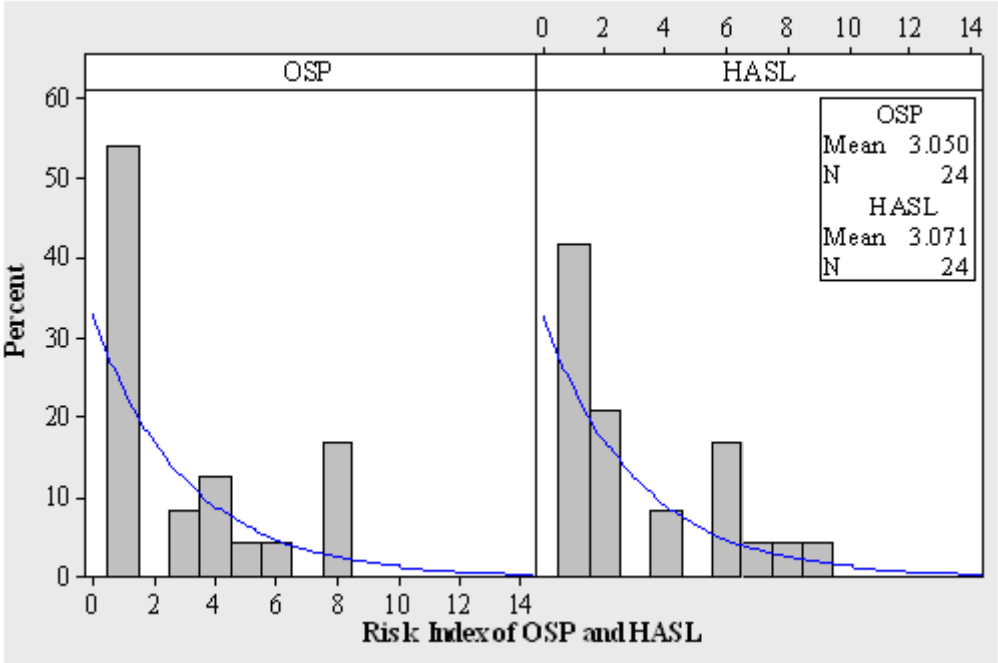

Figure 18: Histogram of OSP and HASL risk index based on the best fit-exponential distribution for both. OSP has a mean of 3.05 and a 95% confidence interval of (2.04, 4.55), and HASL has a mean of 3.07 and a 95% confidence interval of (2.06, 4.58). Sample sizes are both 24.

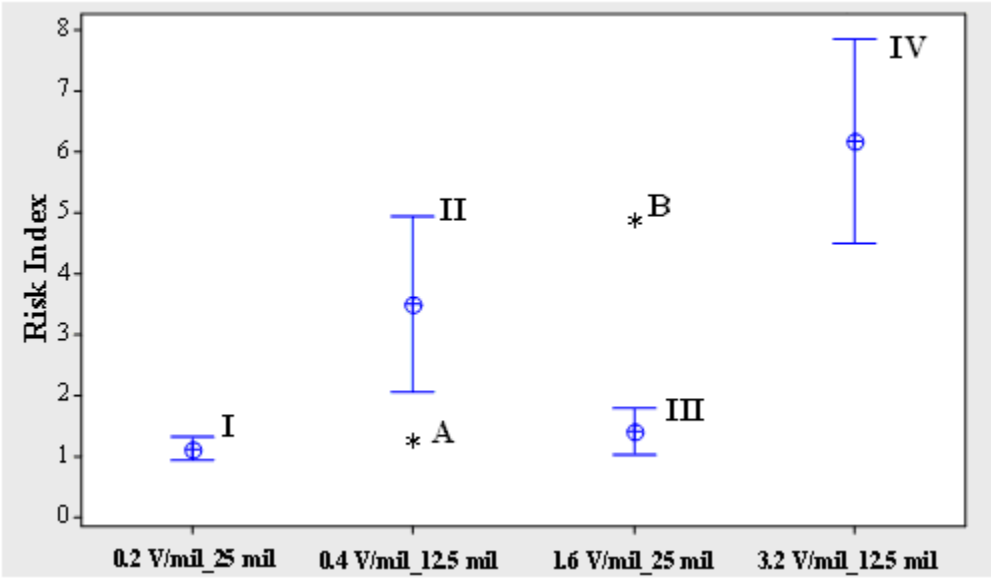

Figure 19: Interval plot (95%) of risk index of 4 combinations of electric fields and their spacings. Group I- 0.2V/mil_25 mil samples have a mean of 1.15, and a

95% confidence interval of (0.99, 1.35); group II-0.4V/mil_12.5 mil samples have a mean of 3.60, and a 95% confidence interval of (2.16, 5.04); group III-1.6 V/mil_25 mil samples have a mean of 1.47, and a 95% confidence interval of (1.23, 1.91); group IV-3.2V/mil_12.5 mil samples have a mean of 6.41, and a 95% confidence interval of (4.85, 7.96). The means and confidence intervals come from their best fit distributions. Asterisk A and B are imaginary points to represent 0.4V/mil_25 mil samples and 1.6V/mil_12.5 mil samples, respectively.

2.4 Conclusions

IPC-B-24 comb patterns have been tested under THB conditions to evaluate the propensity of eutectic SnPb and lead free SAC solder to undergo ECM, and to assess the effects of board finish, electric field and spacing. A clear relationship between the electrochemical behavior and electrical behavior of different solders was established. The dendritic growth on the surface led to intermittent SIR drops, metal layer deposition resulted in a long term SIR decline, and the consumption of electroactive species generated the initial SIR increase right after humidity exposure, a characteristic of a diffusion-controlled cell. A model based on 3-D progressive and instantaneous nucleation was used to simulate the long term SIR decline and it matched the experimental data. The similarities between the simulation and experimental data indicate that both types of nucleation had occurred.

This study shows that SAC solder can exhibit failures under THB conditions if there is a long-term incompatibility between the fluxes and solder systems. The failure

mechanism for the SAC boards, the deposition of metallic layers, was different from the dendritic growth often encountered on SnPb boards. The long-term deposition of metallic layers on the SAC boards necessitates the careful selection and evaluation of flux and solder systems to ensure their long-term compatibilities. The SIR results obtained with SAC solder demonstrate that THB tests of 500 hours or longer may be required to uncover reliability risks. SIR may exhibit a rising trend in the first 100-200 hours and give the impression of stabilization, whereas additional testing may reveal problems that could threaten the reliability of electronic products which have long expected lifetimes.

A co-migration and co-deposition of Sn, Pb, and Cu on the SnPb board and Sn, Cu, and Ag on the SAC board was observed. The co-deposition of these metals was due to their low deposition potentials, which were in the milli-volt range, compared to the 5 V or 40 V applied bias. Although it has been argued by some researchers that Ag cannot migrate at room temperature due to its formation of intermetallic compounds, a small amount of Ag migration was observed in some samples in this study on SAC boards. Among the migrated species, Sn was predominant and manifested itself as layer deposits, Pb was predominant in the dendrites, while only a small proportion of the migrated metal was Cu. The occurrence of dendrites on SnPb boards tested at 40 V rather than at 5 V was attributed to the larger chance for the cathodic overpotential to exceed the critical cathodic overpotential and trigger dendritic growth under conditions of higher electrical stress.

The occurrence of ECM was influenced less by surface finish than it was by solder alloy. In the case of OSP this was attributed to the complexation of OSP during THB testing, which resulted in a non-detrimental green residue. In the case of HASL, the soldering process caused the HASL finish to dissolve into the solder, resulting in a final composition that was not sufficiently different from the nominal solder alloy composition to change its propensity for ECM compared to the OSP samples.

There was interaction between electric field and conductor spacing with respect to ECM. Within a spacing range from 12.5 mil (0.32 mm) to 25 mil (0.64 mm), when the electric field was relatively low (less than 1.6 V/mil), spacing was a stronger factor than electric field in affecting ECM. When the electric field was relatively high (larger than 1.6 V/mil), electric field had comparable influence with spacing on ECM. With the current trend in the electronics industry towards miniaturization, higher density products would be expected to have greater risk of ECM overall, and to exhibit greater sensitivity to spacing than electric field. ECM's larger sensitivity to spacing implies that only lessening the electric field may not be sufficient to mitigate risk, and additional measures are needed to effectively suppress ECM.

Appendix for Chapter 2

Since Fickian diffusion is a special case of a general ion transport process, a series of ion transport equations can be introduced to give a general context in order to clarify the preconditions required for Fickian diffusion. This theoretical framework for ion

transport is given by the Nernst-Planck equation [68], which has broad applications in electrochemistry. The ionic flux

$$J = -D\frac{\partial c}{\partial x} - z\mu Fc\frac{\partial \phi}{\partial x} + cV \tag{A1}$$

where J is the ionic flux, D is the diffusivity, c is the concentration, μ is the mobility of a specific type of ions, F is Faraday's constant, V is the hydrodynamic speed relative to the frame of physical test setup, and z is the charge number of an ion. Here V is zero since the electrolyte is not stirred and static electrodes are used. When the bias is high (40V or 5V), c can be very small in the vicinity of the cathode and practically zero on the surface of the electrode [68]. Thus Equation (A1) reduces to

$$J = -D\frac{\partial c}{\partial x} \tag{A2}$$

Based on the continuity equation and assuming c_1 is an electro-active species in the electrolyte,

$$\frac{\partial c_1}{\partial t} \approx D_1\frac{\partial^2 c_1}{\partial x^2} \tag{A3}$$

with a boundary condition of

$$c_1(x,0) = c_1^b \qquad \text{(initial bulk concentration at t=0)}$$

and

$$c_1(x \to \infty, t) = c_1^b \quad \text{(bulk concentration beyond the diffusion layer thickness).}$$

Equation (A3) can be solved by the Laplace transformation. Its final solution is

$$c_1(x,t) = c_1^b(1 + (a-1)erfc(\frac{x}{2\sqrt{D_1 t}}))$$

where a is a constant related to the voltage step. So the electric current density is

$$i_1(t) = z_1 F J_1 = -z_1 F D_1 (\frac{\partial c_1}{\partial x})_{x=0} = z_1 F c_1^b (a-1)\sqrt{\frac{D_1}{\pi t}} \quad \text{(A4)}$$

If c_1, c_2, …c_k, c_{k+1},…c_n exist in the electrolyte, c_1, c_2, …c_k are all the electro-active species, and c_{k+1}, c_{k+2}, …c_n are all the electro-inactive species, then the electroneutrality assumption results in

$$\sum_1^n z_i c_i = 0$$

Since Equation (A4) can also apply to other electro-active species (not only c_1), the total current density is

$$i_{Total} = i_1(t) + i_2(t) + ... + i_k(t) = \sqrt{\frac{1}{t}} \cdot \sum_1^k (z_i F c_i^b (a-1)\sqrt{\frac{D_i}{\pi}})$$

Thus the measured resistance across the electrodes is

$$R = \frac{U}{i_{Total} A} = \frac{U}{\sqrt{\frac{1}{t}} \cdot \sum_1^k (z_i F c_i^b (a-1)\sqrt{\frac{D_i}{\pi}}) A} = \frac{U}{\sum_1^k (z_i F c_i^b (a-1)\sqrt{\frac{D_i}{\pi}}) A}\sqrt{t} \quad \text{(A5)}$$

where U is the voltage bias across the electrodes, and A is the cross-sectional area of the electrolyte.

Chapter 3

Electrochemical Impedance Spectroscopy Analysis of Metal Migration Kinetics on Printed Circuit Boards in Deionized Water

Abstract

The kinetics of electrochemical migration following the potentiostatic charging of copper electrodes on printed circuit boards in deionized water was investigated using electrochemical impedance spectroscopy and cyclic voltammetry. Using a Ag/AgCl reference electrode, the kinetics of Cu dendritic growth on the cathode and copper dissolution on the anode was separately studied. The diffusion resistance and the charge transfer resistance at the anode and the cathode before and after dendritic growth were determined by applying an equivalent electrical circuit to the electrochemical impedance spectroscopy data. The rate limiting step of electrochemical migration was identified as the diffusion at the anode.

3.1 Introduction

With the miniaturization of electronic products, there is a greater risk that the electrical bias across metal traces on printed circuit boards (PCBs) will trigger electrochemical migration (ECM) and result in a short circuit. ECM is defined as the growth of conductive metallic structures on a PCB through an electrolyte solution under a DC voltage bias [64]. The humidity and impurities in air can produce an electrolyte between metal traces, resulting in metal corrosion and deposition under a

DC voltage bias. The steps in ECM include path formation, electrodissolution, ion transport, electrodeposition, and filament growth [63]. Path formation is the formation of an electrolyte between two electrodes. Electrodissolution is the oxidation of metals to generate cations at the anode. These metal cations can migrate under the electromotive forces to the cathode (ion transport) and deposit at the cathode as neutral metal. As more and more neutral metal deposits on the nuclei (electrodeposition), dendritic structures may grow from the cathode toward the anode (filament growth). Dendritic growth reduces the surface insulation resistance (SIR) between adjacent metal traces, leading to current leakage and intermittent or irreversible circuit failures of PCBs.

The electrodeposition and electrodissolution of metals, and models describing both, have been investigated in prior studies [70]-[107]. However, these publications are limited to the investigation of either electrodeposition or electrodissolution and use an inert metal as a counter electrode; therefore, the results may not be applicable to a practical case when the same metal is conjugately used as both the anode and the cathode on a PCB. Although the electrochemical reaction kinetics of a conjugate cell was investigated by Sun et al. [108], the kinetics of electrodeposition on the cathode and electrodissolution on the anode metal could not be separated from the overall ECM due to the lack of a reference electrode, and thus the rate limiting step could not be determined. Identification of the dominant factors and the rate limiting step in ECM is essential for developing an accurate model of the kinetics of dendritic growth and is helpful for devising strategies to mitigate ECM.

Electrochemical impedance spectroscopy (EIS) investigates the kinetics of electrochemical oxidation and deposition of metals because it separates the electrolyte resistance, charge transfer resistance, and diffusion resistance based on their frequency dependencies. EIS sweeps an AC signal (voltage or current) over a wide range of frequencies and measures the responses (current or voltage) of an electrochemical system [62]. The impedances of an electrochemical system can be obtained by fitting EIS data to a physicochemical model [101][110] or an equivalent electrical circuit [70][107][62].

In this study, the kinetics of dendritic growth on a cathode copper trace and copper dissolution on an anode copper trace was independently investigated using EIS. The rate limiting step for ECM on PCBs under an electrical bias across metal traces was obtained.

3.2 Experimental Setup and Procedure

Comb structures from standard IPC-B-25 test boards were used to study the kinetics of dendrite growth and dissolution of Cu. The gap between adjacent traces was 0.635 mm (25 mil). In order to control the growth between one pair of electrodes and facilitate optical observation, one pair of electrodes was isolated by severing the rest of the electrodes, as shown in Figure 1. This was conducted so that dendrites could only grow within one gap. The copper traces were covered by an organic solderability preservative (OSP) coating made of benzimidazole (200 nm thickness), which prevents Cu from oxidation. An Ag/AgCl micro-reference electrode was located close to the electrodes to monitor the cathode and anode potentials during electrochemical tests, as shown in Figure 1. An illustration of the ECM is shown in Figure 2.

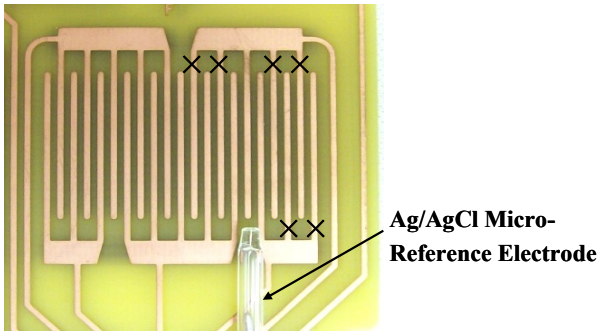

Figure 1: Comb structures of IPC-B-25 test boards and Ag/AgCl micro-reference electrode.

Deionized (DI) water with a resistivity greater than 18.2 MOhms·cm was used as the electrolyte. The DI water was exposed to room ambient conditions. The use of DI water can create a direct migration path for ECM and avoid the time-consuming path formation step when the comb is under a humidity environment and adsorbed moisture becomes an electrolyte. Before starting the test, the comb structure was rinsed with DI water. Then, the comb structure was inserted into the DI water electrolyte. The open circuit potential (OCP, the equilibrium potential of the whole system when the net current is zero) of the bare copper electrodes in DI water was 0.05–0.08 V, relative to the Ag/AgCl reference electrode.

A series of constant potentials, relative to the Ag/AgCl reference electrode (equal to DC voltage of 3.0 V to 4.4 V across the cell), were applied on the anode for 1 or 2 minutes to initiate dendrites. If dendritic growth was detected, the DC potential lasted for no longer than 1 minute. After each potential application and 1 hour of relaxation at an open circuit, the impedances of anode dissolution and cathode deposition were sequentially measured by switching the working electrode to the anode and cathode, respectively, and applying EIS from 10^6 Hz to 0.1 Hz at a 5mV AC potential. Thus,

each impedance measurement included an anode impedance and a cathode impedance.

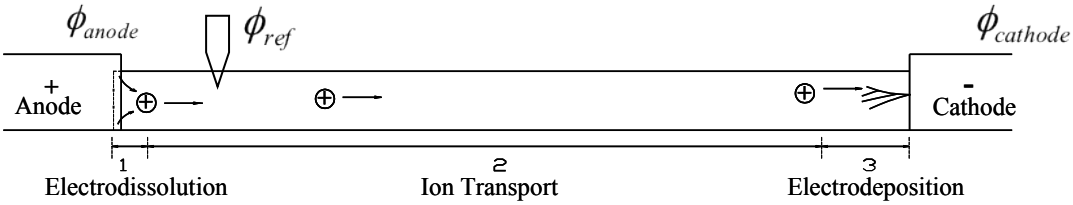

Figure 2: The ECM process that occurred on the surface of the comb structure.

After each EIS measurement, a DC bias was again applied on the cell, followed by another EIS measurement. Therefore, the DC bias and EIS measurement were applied sequentially to measure the reaction kinetics at the anode and cathode at different dendrite growth stages, until the dendrites finally touched the anode. Potentiodynamic polarizations over a potential range of 0–1.6 V at a scan rate of 5 mV/s were also applied on the anodes to investigate the anodic dissolution and the growth of dendrites on the cathode. Both the potentiodynamic polarization and EIS tests were recorded using a Solartron 1260/1287 Electrochemical Interface (Solartron Metrology, UK).

3.3 Equivalent Circuit

The PCB comb structures can be represented by the equivalent circuit in Figure 3.

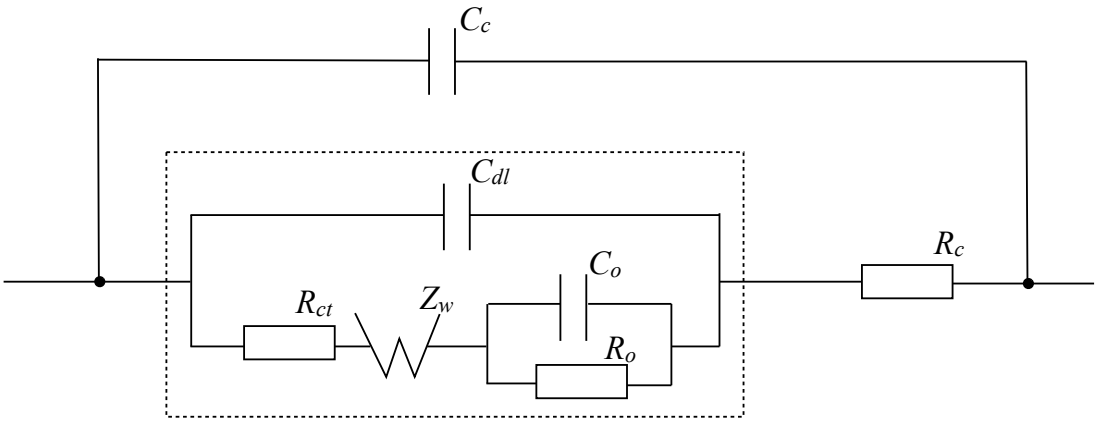

Figure 3: The equivalent circuit of electrodes (anode or cathode) corresponding to Figure 2. C_c is the electrical capacitance of the electrodes, C_{dl} is the double layer charging capacitance, R_c is the ionic transport resistance, R_{ct} is the charge transfer resistance, Z_w is the Warburg diffusion resistance, C_o is the capacitance associated with the OSP coating, and R_o is the resistance of the OSP coating.

3.4 Results and Discussion

The current responses of constant potentials and potential dynamic scans, the EIS spectra before and during dendritic growth, the cell parameters such as C_{dl}, C_c and R_o and the rate limiting step will be discussed.

3.4.1 Current Response

Different potentials (vs. Ag/AgCl reference) were applied on the anode to monitor the anodic dissolution and cathodic deposition. Figure 4 shows the anode current responses under potentiostatic charge at different potentials. The current density increased with potential in general, but when the applied potential reached 1.8 V, the current density initially increased, started to decrease after 12 seconds, and then

increased again. The current decrease after 12 seconds may have been caused by faster Cu oxidation than Cu^{2+} dissolution in electrolyte, forming a complex layer of CuO and $Cu(OH)_2$ on the anode [112]. The Cu oxide layer separated Cu from the electrolyte, retarding the electrochemical oxidation rate until the Cu oxidation rate was equal to the dissolution rate. In an electrolyte with a relatively high concentration of bicarbonate (0.75 M) and carbonate (0.05 M), a layer of $Cu(OH)_2$ and $CuCO_3$ forms at the anode [112]. But, in the DI water electrolyte in this study, a complete passivation layer of Cu reaction products at the anode was unlikely to form. Therefore, this short diffusive period was followed by a gradual increase in the current density, because the Cu^{2+} dissolution in the electrolyte kept enhancing the ionic conductivity of electrolyte with time.

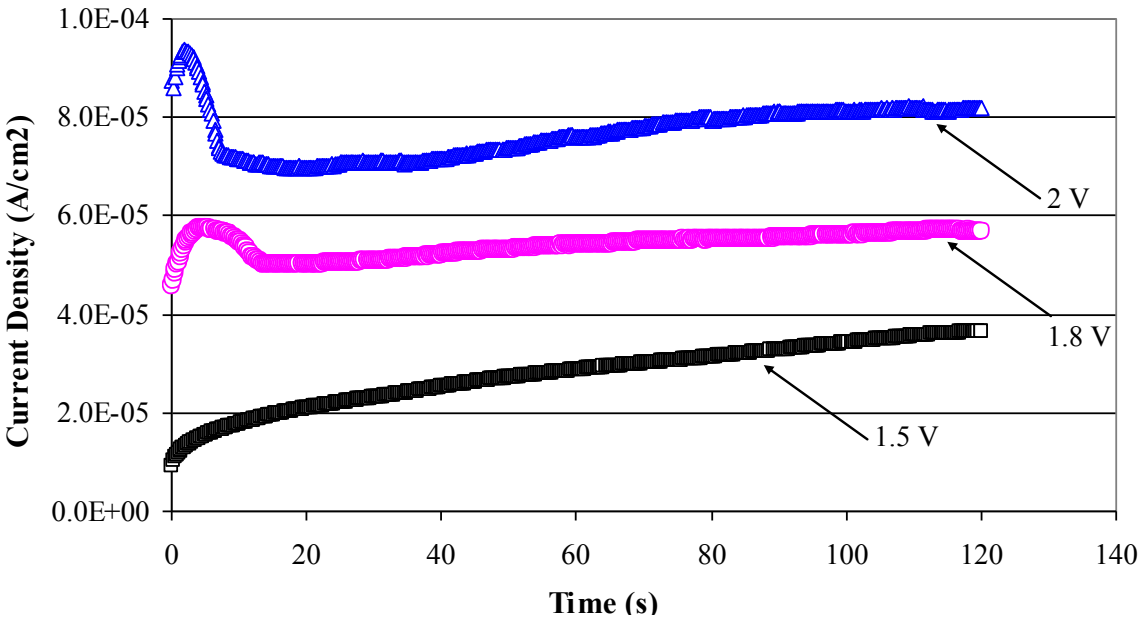

Figure 4: Current responses of the copper trace–DI water cell at different applied potentials.

When dendrites did not touch the anode, the current density curve under potentiostatic charge was smooth and continuous. However, when a dendrite touched the anode, the current density showed a sudden jump followed by oscillations for an extended period,

as shown in Figures 5. The potential for initiation of dendrites varied depending on the concentration of Cu^{2+} in the electrolyte, where a higher Cu^{2+} concentration had a lower potential for dendrite initiation. A higher Cu^{2+} concentration resulted from applying a higher potential or extending the application time at a given potential.

The dendritic growth could also be initiated by potentiodynamic polarization scans. Figure 6 shows the current responses of a fresh DI water cell under potentiodynamic scans. Dendrites did not form during the first four potentiodynamic polarization scans from 0.0v to 1.6V, but they initiated and touched the anode in the fifth scan, which was observed in situ by an optical microscope.

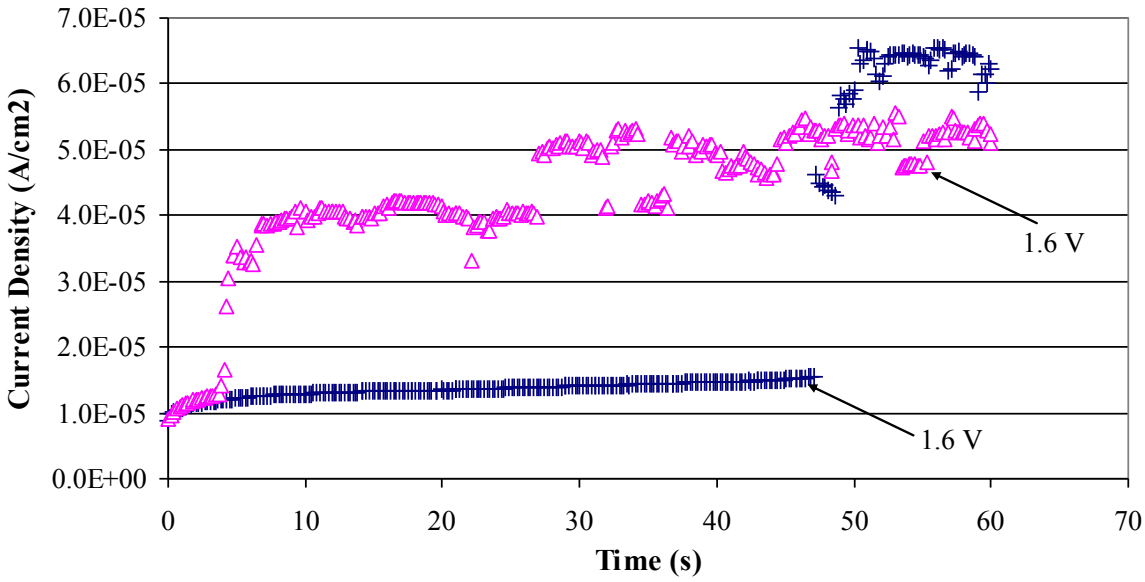

Figure 5: Typical potentiostatic responses of the copper trace–DI water cell when dendrites started to grow. The current density jumped once dendrites touched the anode and then oscillated, as shown by these two typical DC applications.

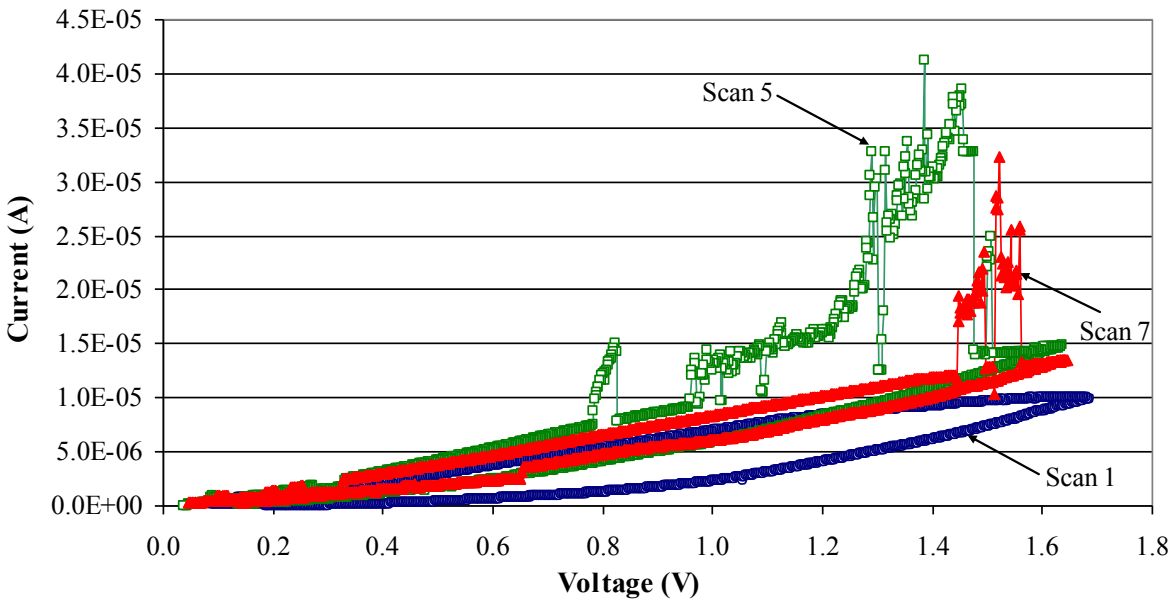

Figure 6: Typical potentiodynamic polarization scans of the copper trace–DI water cell with (red and green) and without (blue) dendritic growth. The potential went from 0 V to 1.6 V before returning to 0 V, and the scan rate was 5 mV/s. All potentials were applied with respect to the Ag/AgCl reference electrode.

3.4.2 EIS Results before Dendritic Growth

Fifteen series of impedance measurements were conducted after each constant potential or potentiodynamic polarization. A typical series of anode and cathode impedances after four successive potentiodynamic polarizations from 0.0V to 1.6V before dendrite formation are shown in Figures 7 and 8, respectively. The impedances of both the anode and the cathode consist of three overlapped semicircles. The depressed high-frequency-semicircle (10^6 Hz to around 8.5 KHz) corresponds to the ion transport across the OSP layer at the anode and cathode. The depressed medium-frequency semicircle (8.5 KHz to around 40 Hz) corresponds to the charge transfer that is in parallel with the double-layer capacitance in the equivalent circuit (Figure 3). The first two semicircles' impedances are overlapped and cannot be distinguished on the anode (Figure 7) due to the large impedance scale, but can be observed on the

cathode impedance (Figure 8). The low-frequency region (40 Hz to 0.01 Hz) corresponds to the limited diffusion of copper ions in the electrolyte solution, which is in series with the charge transfer resistance in the equivalent circuit (Figure 3).

The diffusion impedance at the low frequency region decreased in both the z' and z" axes after each potentiodynamic polarization. The anodic diffusion impedance is proportional to the Warburg impedance coefficient (Equation 1), which is in an inverse relation (Equation 2) to the bulk concentration of electroactive species (Cu^{2+} in this case). So, as the copper dissolution proceeded, the copper ion concentration at the anode increased with time, resulting in a decrease of anodic diffusion impedance in both the z' and z" scales, as shown in Figure 7. Therefore, the diffusion semi-circle "shrunk" toward the origin as the dissolution proceeded. The anodic charge transfer resistance remained the same (Table 1), because copper dissolution in the beginning had not created a rougher surface, and thus, the effective surface area remained the same, as expressed in Equation 3.

It was observed that the charge transfer resistance at the cathode remained almost the same, as shown in the cathodic impedance curve in Figure 9 and Table 1. The lack of change in cathodic charge transfer resistance was because the reaction at the cathode before dendritic growth (reduction of copper ions) was mainly the reduction of hydrogen ions. The reduction of hydrogen ions caused the effective surface area of the cathode to be time-independent. The cathodic diffusion resistance decreased appreciably by the increase of copper ion concentration. By fitting the experimental results to the equivalent circuit model (Figure 3), the parameters of the cell were extracted (Table 1) and are shown in Figure 9. The diffusion resistance at the anode dominated the cell kinetics before dendrite growth initiated.

$$Z = \sigma\omega^{-1/2}(1-j)\tanh(\delta(\frac{j\omega}{D})^{1/2}) \quad (1)$$

$$\sigma = \frac{RT}{\sqrt{2}An^2F^2}(\frac{1}{c_o^*\sqrt{D_o}} + \frac{1}{c_R^*\sqrt{D_R}}) \quad (2)$$

$$R_{ct} = Z_{ct} = \frac{RT}{j_0 nF} = \frac{RT}{(nF)^2 Ak_0} \quad (3)$$

where Z is the Warburg impedance, σ is the Warburg impedance coefficient, δ is the diffusion layer thickness, ω is the applied frequency, R is the gas constant, T is the temperature, C_o^* is the bulk concentration of oxidant, C_R^* is the bulk concentration of reductant, D is the diffusivity, A is the surface area of electrodes, n is the number of transferred electrons in the reaction, F is the Faraday constant, and k_0 is the standard heterogeneous rate constant.

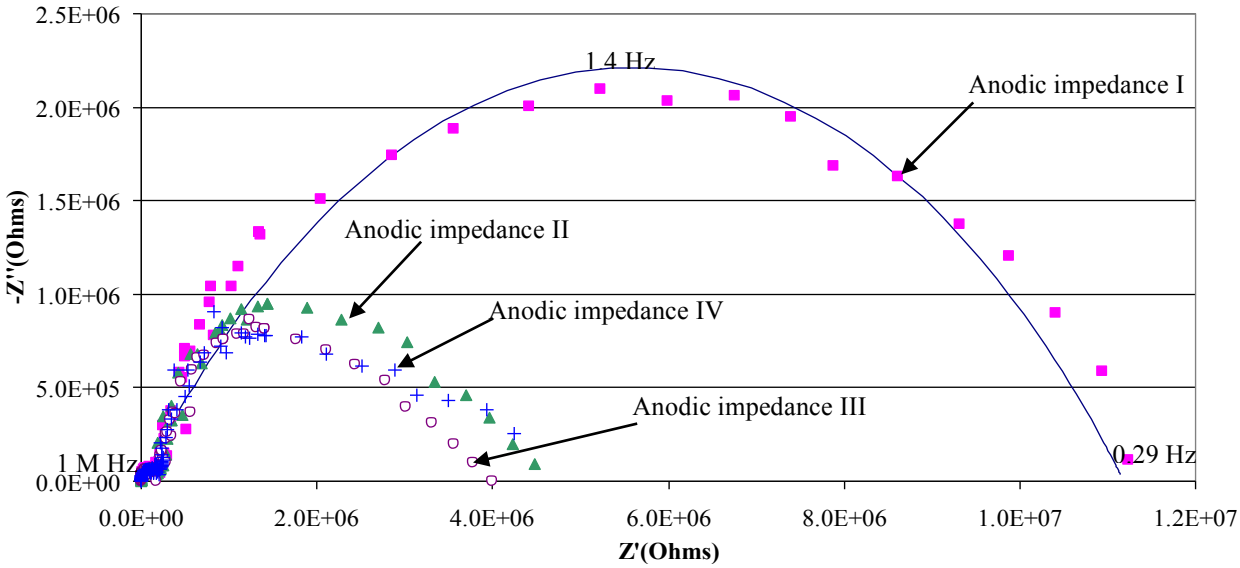

Figure 7: A series of anode impedances in a Nyquist plot. Each was followed by a potentiodynamic scan from 0.0 V to 1.6 V before dendritic growth on the cathode. The solid curve is the fitted curve for anodic impedance I. The fitted parameters: σ

=2.5x10^{6} Ohm (Hz)$^{0.5}$, δ=0.06 mm, Cc=8.32x10^{-11} F. Other fitted values are shown in Table 1. The copper ion diffusivity D=3.67x10^{-10} m^2/s.

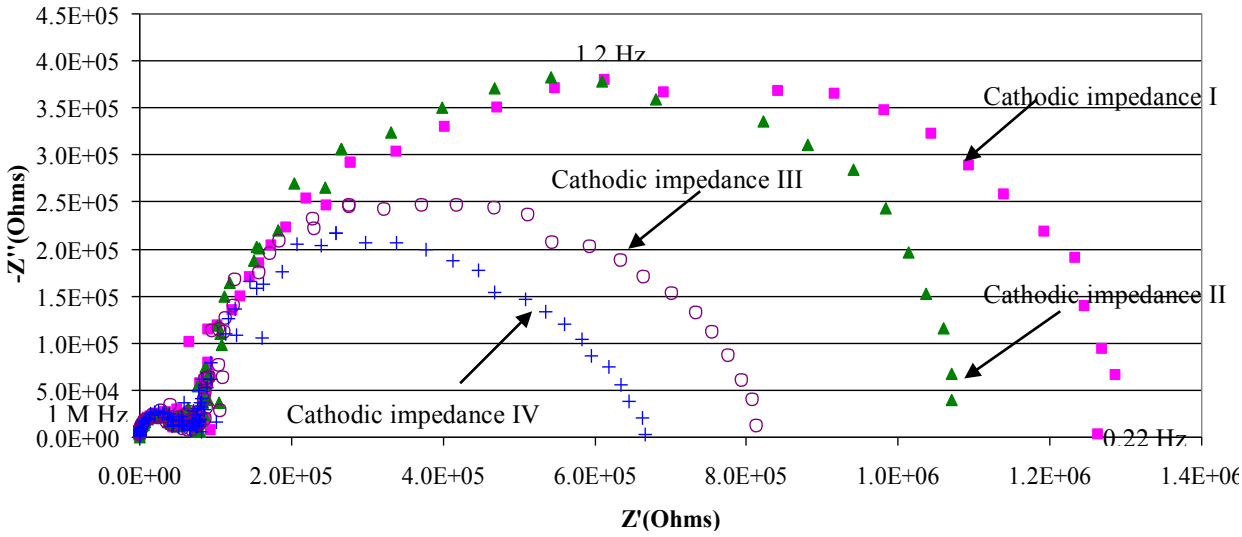

Figure 8: A series of cathode impedances in a Nyquist plot. Each was followed by a potentiodynamic scan from 0.0 V to 1.6 V before dendritic growth.

Table 1 Copper Trace–DI Water Cell Parameters before Dendritic Growth

Impedance Measurement Stages	R_c (Ohms)	R_{ct_anode} (Ohms)	$R_{ct\_cathode}$ (Ohms)	Z_{w_anode} (Ohms)	$Z_{w\_cathode}$ (Ohms)	C_{dl_anode} (F)	$C_{dl\_cathode}$ (F)
I	39.4	1.1x10^{5}	3.0x10^{4}	1.1x10^{7}	1.2x10^{6}	3.0x10^{-9}	3.9x10^{-9}
II	158.4	1.1x10^{5}	4.2x10^{4}	4.4x10^{6}	1.0x10^{6}	6.7x10^{-10}	2.4x10^{-9}
III	148.2	1.0x10^{5}	4.0x10^{4}	3.8x10^{6}	7.3x10^{5}	9.8x10^{-10}	6.4x10^{-9}
IV	94.2	1.3x10^{5}	3.7x10^{4}	4.4x10^{6}	6.0x10^{5}	1.3x10^{-9}	2.0x10^{-9}

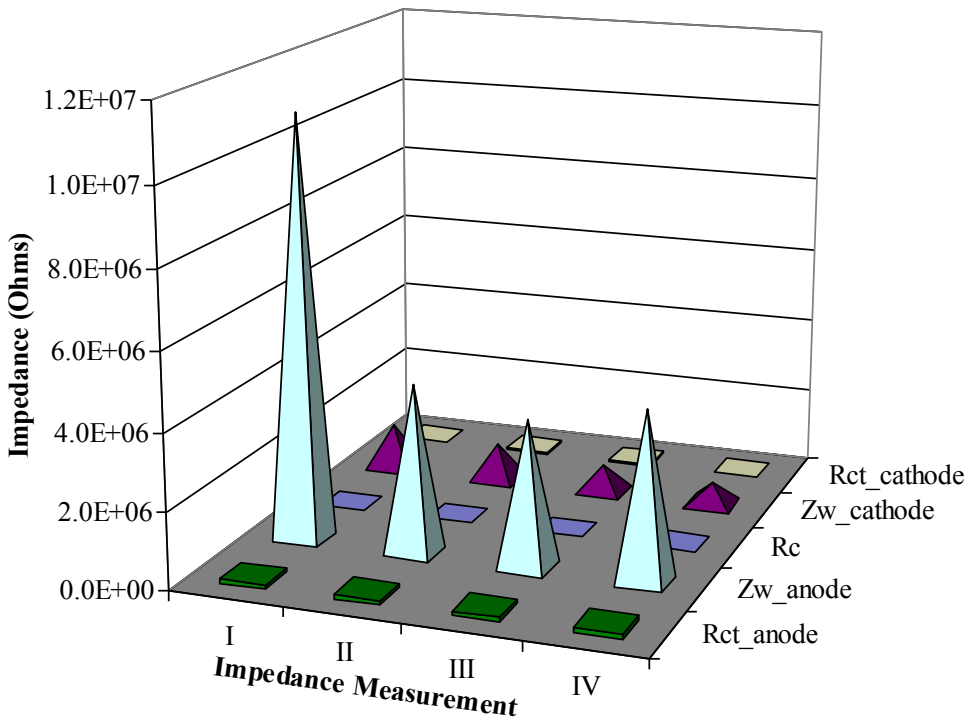

Figure 9: Copper trace–DI water cell parameters before dendritic growth.

3.4.3 EIS Results during Dendritic Growth

Impedance measurements during dendritic growth were also conducted sequentially with potentiodynamic polarizations or constant potentials, from dendrite initiation until dendrites touched the anode. The anodic and cathodic impedances are shown in Figures 10 and 11, respectively.

The impedance spectra during dendritic growth were processed using the same frequency region assignments and fittings as before dendritic growth. The cell parameters in three successive dendritic growth stages were extracted (Table 2) and are shown in Figure 12. After dendrites initiated, the charge transfer resistance decreased to about 55% at the anode. The reduced charge transfer resistance on the anode was because of the increased surface roughness due to the electrodissolution of copper with time. The small amount of variation of the charge transfer resistance on the cathode was due to the fact that, after dendrites initiated, the current in the cell

was more concentrated at the tip of dendrites, and the effective surface area at the tip of dendrites did not change significantly as the dendrites grew.

The diffusion resistances at the anode and cathode also decreased. Because the anode was the source of copper ions and the cathode was the "sink" of the copper ions, when dendrites were growing, a concentration gradient of copper ions existed between the anode and the cathode. There were larger concentrations of copper ions closer to the anode. So, as dendrites grew toward the anode, the frontier of dendrites approached a region of "richer" copper ions, thus lowering the cathodic diffusive resistance based on Equations 1 and 2. The anodic diffusive resistance decreased because the anode surface roughened by continued metal dissolution and the increase in copper ion concentration at the anode.

It was observed that the diffusion resistances were approximately one order of magnitude higher than the charge transfer resistances at both the anode and cathode. Thus, ion transport in the electrolyte was more difficult than charge transfer at electrodes. In addition, the anodic diffusion resistance was larger than the cathodic diffusion resistance, and so the anodic diffusion dominated the dendritic growth process. Since the growth of dendrites depends not only on the cathode overpotential, but also on the copper ion concentration at the cathode, the availability and sustainability of copper ions transported from the anode are substantial in maintaining the concentration at the cathode. Therefore, the anodic diffusion of copper ions into the bulk regulated the whole ECM process, thus rendering anodic diffusion the rate limiting step. A typical dendrite is shown in Figure 13. The cell parameters are shown in Figure 14.

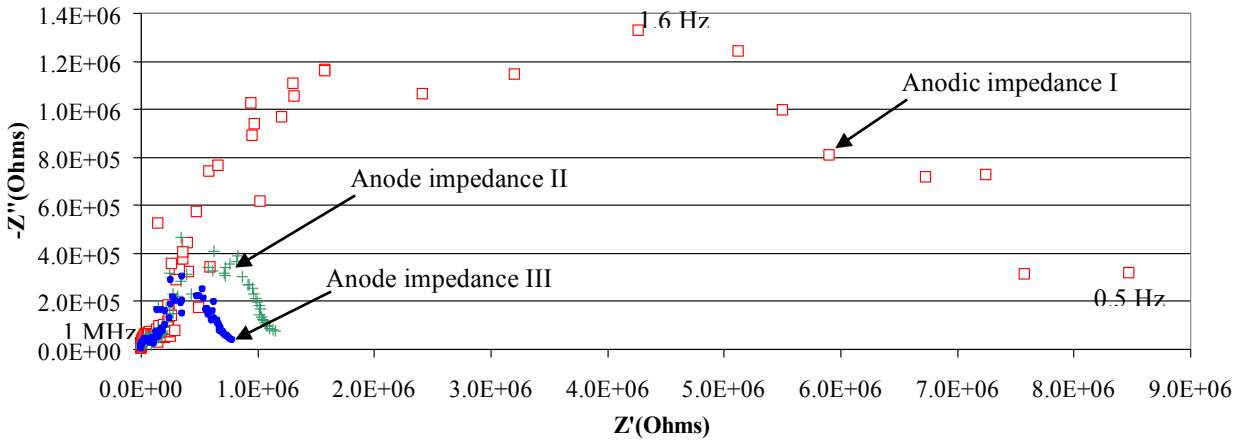

Figure 10: Anodic impedance of copper trace–DI water cell during dendritic growth.

3.4.4 Confirmation of C_{dl} and C_c

Based on the literature [70][62], the double-layer charging capacitance, C_{dl}, and the capacitance of the copper traces, C_c, are 10^{-9} F and 10^{-11} F, respectively. The capacitances of copper traces in air and in DI water at room ambient conditions were measured using an Agilent 4263B LCR meter. The capacitances of copper traces (5 pairs of anode–cathode in parallel) were 5.20×10^{-12} F in air and 1.65×10^{-8} F in DI water. This means that one pair of electrodes had capacitance values of 1.04×10^{-12} F in air and 3.3×10^{-9} F in DI water. When in air, the capacitance value 1.04×10^{-12} F was the C_c *in air* without the influence of C_{dl}. When in DI water, the capacitance value 3.3×10^{-9} F was an overall capacitance value of C_{dl} and C_c *in water* in parallel (the sum of both). The C_c *in water* is 80 times the C_c *in air* because water's relative permittivity is 80 in room ambient conditions, so the C_c *in water* was 8.32×10^{-11} F in this study in the same level with the fitted values. So, the C_{dl} dominated the obtained capacitance value: 3.3×10^{-9} F *in water*. Based on the experimental measurements, the C_{dl} was 10^{-9} F *in DI water*, matching the fitted values (Tables 1 and 2). This suggests that it is correct to apply the equivalent circuit model (Figure 3) to ECM.

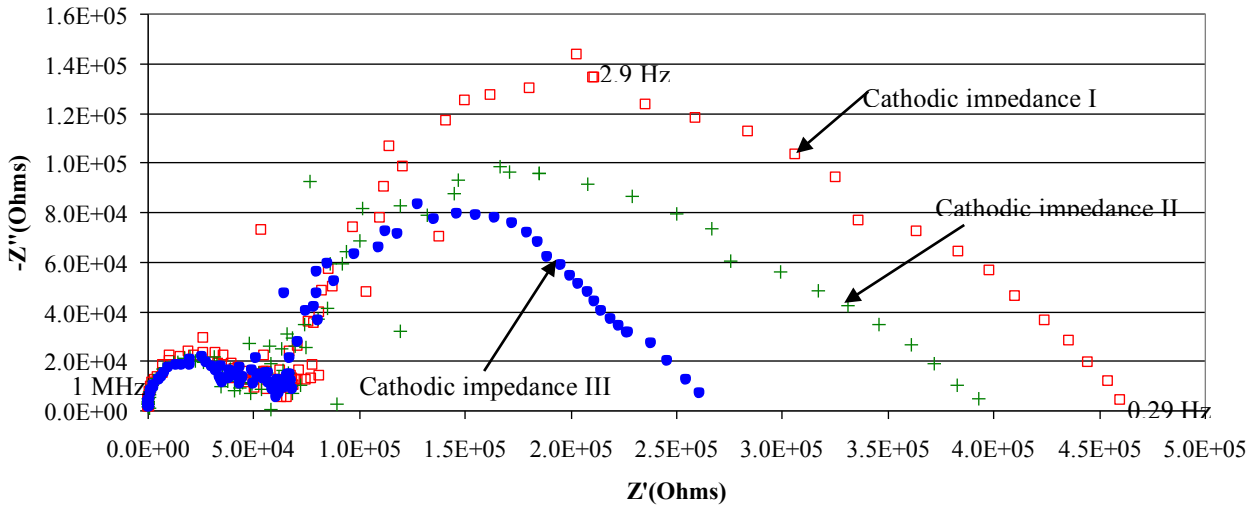

Figure 11: Cathodic impedance of copper trace–DI water cell during dendritic growth.

Table 2 Copper Trace–DI Water Cell Parameters during Dendritic Growth

Impedance Measurement Stages	R_c (Ohms)	R_{ct_anode} (Ohms)	$R_{ct\_cathode}$ (Ohms)	Z_{w_anode} (Ohms)	$Z_{w\_cathode}$ (Ohms)	C_{dl_anode} (F)	$C_{dl\_cathode}$ (F)
I	129.6	$1.1x10^5$	$3.4x10^4$	$8.0x10^6$	$4.0x10^5$	$5.7x10^{-10}$	$1.2x10^{-9}$
II	145.8	$8.3x10^4$	$2.8x10^4$	$1.7x10^6$	$3.3x10^5$	$2.2x10^{-9}$	$3.1x10^{-9}$
III	105.5	$5.0x10^4$	$3.3x10^4$	$1.0x10^6$	$2.0x10^5$	$1.1x10^{-9}$	$3.5x10^{-9}$

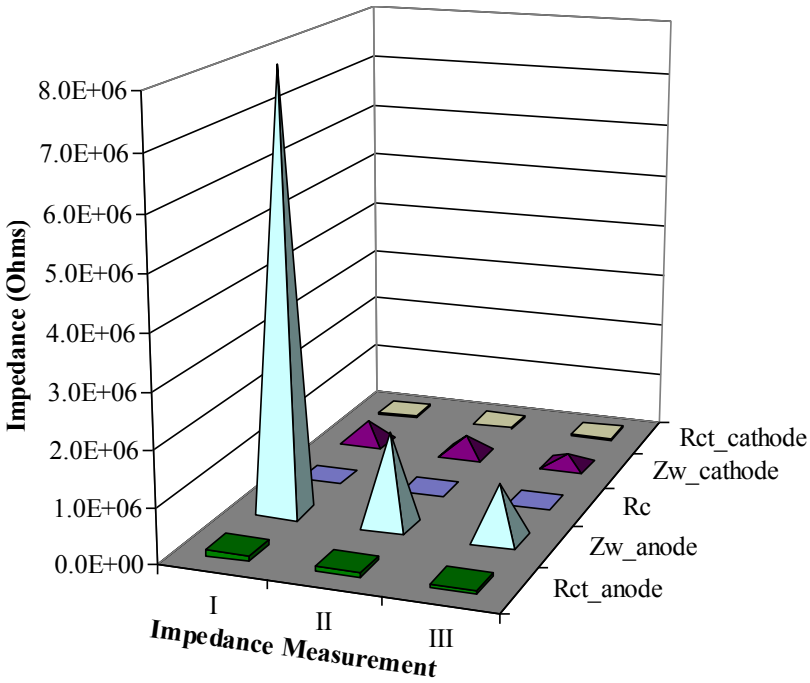

Figure 12: Copper trace–DI water cell parameters during dendritic growth.

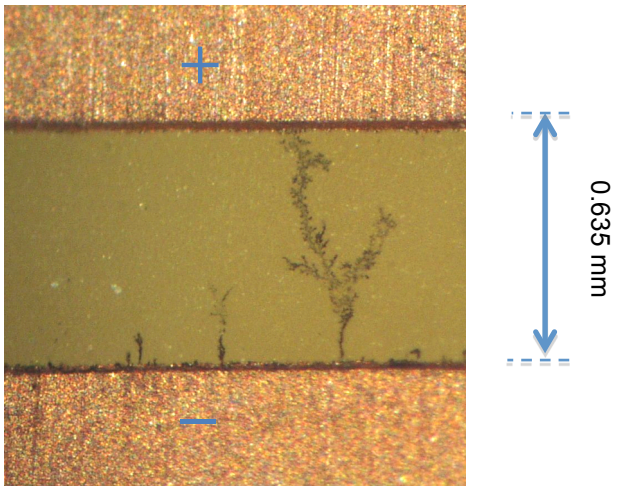

Figure 13: A typical dendrite grown after the alternate DC and AC applications.

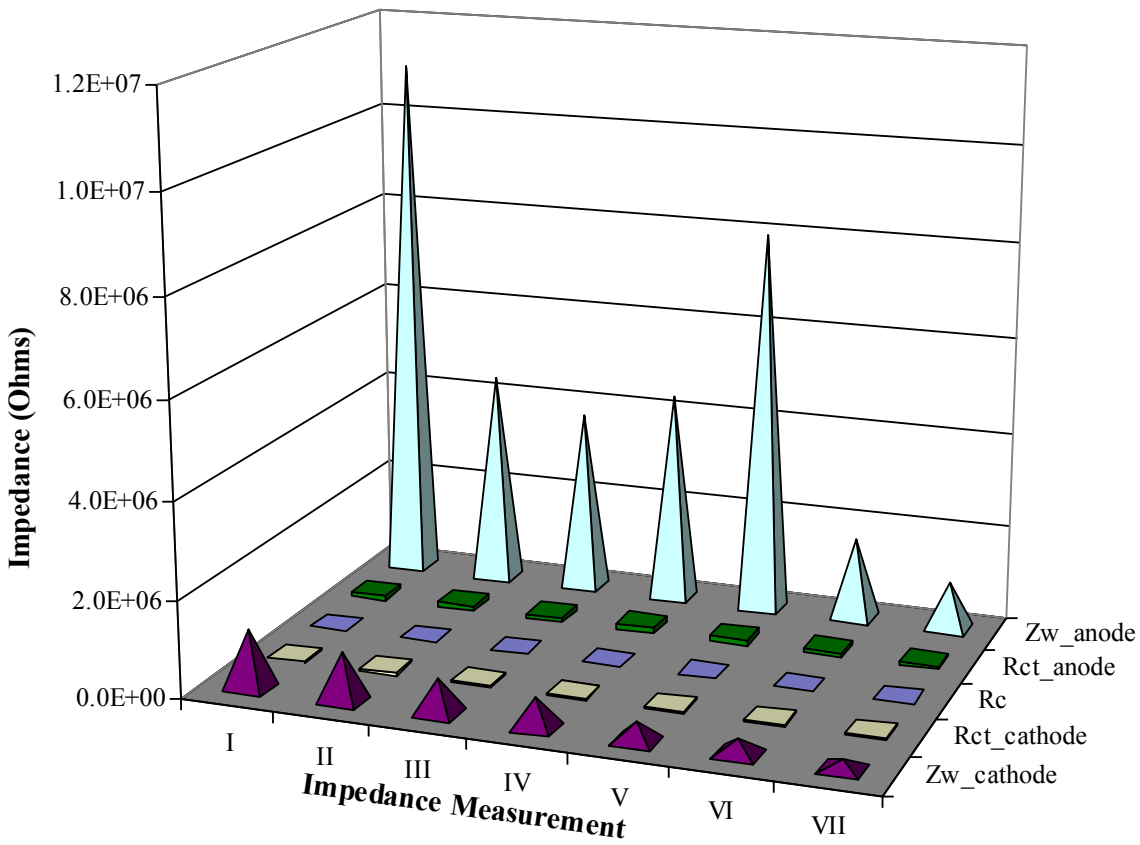

Figure 14: Copper trace–DI water cell parameters before and during dendritic growth. Dendrites initiated at stage V and touched the anode at stage VII.

3.4.5 Resistance to Transport through the OSP Layer

The resistance of copper ion transport through the OSP layer, R_o, is estimated to be $4x10^4$ Ohms, based on Figures 7, 8, 10 and 11. R_o is close to R_{ct}, but much smaller than Z_w; this suggests that the OSP layer is not an effective barrier to retard the dissolution of copper ions. This is because, in the bulk of OSP, there is a gradient of copper ions which originates from the diffusion of copper ions from the copper traces [115], while on the OSP surface exposed to air there is a layer of native Cu_2O that is a few nanometers thick and is prone to cracking [116]. Thus, copper ions can transport

through microcracks in the Cu_2O layer and dissolve into the electrolyte. This also implies that EIS can be used to detect a coating's effectiveness in preventing ECM.

3.4.6 Discussion of the Rate Limiting Step

The rate limiting step of an electrochemical cell depends on both electrode materials and electrolytes. In an $AgNO_3$ (0.3~12%) and KNO_3 electrolyte, it was found that the dendritic growth of Ag was controlled by both the spherical diffusion of Ag^+ to the dendrite tip and the activation (charge transfer at the tip) [18]. But in zincate solutions (0.01~0.2 mol/L) before zinc dendrites initiated, the bulk diffusion dominated; but when zinc dendrites started to grow, activation (charge transfer) dominated [114]. This study demonstrates that in a DI water electrolyte, the cell resistances ranked as $Z_{w\_anode} > Z_{w\_cathode} > R_{ct\_anode} > R_o > R_{ct\_cathode} > R_c$ before and during copper dendritic growth. This indicates that copper ion transport in the DI water electrolyte is more difficult than charge transfer at the anode or the tips of dendrites. This is because the lack of electroactive ions in the DI water initially resulted in a low conductivity electrolyte (compared to an electrolyte with electroactive ions and supporting salts); thus, the availability and sustainability of copper ions transported from the anode were substantial in triggering and maintaining the deposition at cathode (dendritic growth). So the diffusion of copper ions from the anode became the rate limiting step.

3.5 Conclusions

Potentiostatic applications, potentiodynamic scans, and electrochemical impedance spectroscopy were employed to study the kinetics of metal dissolution and dendritic growth on PCBs in DI water electrolyte. For the entire ECM process (before and during dendrite growth), anodic diffusion was the rate limiting step. This suggests that measures to suppress dissolution, such as coatings on Cu at the anode, could decrease ECM propensity and short circuits effectively.

This study also found that diffusion resistances decreased consistently with time during ECM with the exception of an abnormal increase in the anodic diffusive resistance due to the initiation of dendrites. But the traditional electrical current or SIR monitoring, as specified in IPC-TM-650 Method 2.6.14.1, detects an abnormal change of current or SIR only when dendrites touch the anode. This means the EIS is more sensitive than SIR monitoring in perceiving the physicochemical changes of the ECM process. Therefore, this study offers the electronics industry another option for how to detect dendritic growth by checking system impedances using EIS, in addition to the traditional current or SIR monitoring.

EIS impedance spectra indicate that OSP cannot effectively retard the dissolution of copper ions and suppress ECM in DI water electrolyte, although it can protect bare copper from being oxidized in air. This implies that electronics may incur ECM when condensation occurs between copper traces finished with OSP. This also suggests that EIS can be used to detect a coating's effectiveness to prevent ECM.

Finally, the identification of the anodic diffusion control and anodic charge transfer resistance values has helped to develop a physicochemical model of ECM to determine the concentration, flux density profiles, and time needed for dendrites to span the gap of electrodes on PCBs, which will be reported soon by the authors.

Chapter 4

Analysis of the Kinetics of Electrochemical Migration on Printed Circuit Boards Using Nernst-Planck Transport Equation

Abstract

This study modeled the kinetics of electrochemical migration under condensed conditions between copper conductors on printed circuit boards using Nernst Planck equation and impedance measurement. The times to generate an embryonic dendrite at cathode and grow from cathode to anode were measured experimentally and modeled. It was found that by acquiring electro-active ion surface concentration at anode with the help of impedance measurement and by considering migration and diffusion in the bulk ion transport, the model matched the experimental results quantitatively. The model was also extended to non-condensing condition by comparing the conductance in bulk water and moisture films. Historical models were applied to the experimental results and compared with the model of this study.

4.1 Introduction

With the trend towards miniaturization and high density in electronics, an electrochemical phenomenon known as electrochemical migration (ECM) can occur on printed circuit boards (PCBs), when PCBs are exposed to moisture or condensed water drops with applied potential difference. ECM is divided into a few steps: path

formation, electrodissolution, ion transport, and electrodeposition [117]. Path formation refers to the adsorption of a continuous moisture film on the surface of substrates as a leakage path under non-condensing conditions. Under a condensing condition such as a water drop bridging gaps of metallizations, this step is not required. After path formation, metal from the anode, under an electric field, dissolves into the electrolyte, migrates through the electrolyte, and deposits on the cathode in a neutral form. Thus dendrites form and grow from the cathode toward the anode, which is the manifestation of electrodeposition on a macroscopic level.

Because dendrite growth can lead to degradation of surface insulation resistance (SIR) and even short circuits when dendrites touch anode, ECM constitutes one failure mechanism in electronic products. This situation is exacerbated when products are designed to be smaller in that compacted designs shrink conductor spacings and increase the electrical field. Due to its disadvantageous effect, the modeling of time to failure (TTF) caused by ECM is of special interest in electronics.

Barton and Bockris [118] provided the first quantitative model to describe dendrite growth speed with respect to overpotential and radius of growth tip. An optimum growth speed was derived based on the variation of tip radius. The growth speed was observed to be constant and have a linear or parabolic relation to overpotential depending on whether the exchange current approaches zero or infinity, respectively. The time from application of bias to initiation of embryonic dendrites, known as

incubation time, was just extrapolated by the length of dendrites after they grew. However, this method cannot be used to predict incubation time and cannot explain the physics in this period.

Despic, et al [119][120], extended Barton and Bockris theory to the current density in the nonlinear region under activation and diffusion control, and considered multi-step electron discharge process. Diggle, et al [121] developed a model to extrapolate the incubation time, based on the initiation of zinc dendrites from rotation of screw dislocations, but this model only had qualitative match with experimental results, especially when zincate concentration approached a dilute solution. The propagation rate, assuming an activation control in the growth process, had a good match with experimental results.

Popov, et al [122][123][124] extended the model for incubation time as a function of overpotential, bulk concentration and initial height of protrusion, based on the exponential dependence of surface roughening amplification on time in the dendrites initiation process. It was found after a certain limit, the incubation time has no dependence on overpotential anymore.

Shyu [125] developed a model by considering ion transport (diffusion control only), activation and surface energy using interfacial instability and perturbation theory to describe the incubation and growth process. This model was able to determine the

critical overpotential as a function of exchange current density and the growth rate by assuming the tip radius to be paraboloid shape. However, the incubation time could not be quantitatively determined, and the fitting between the growth model and the experimental results from Diggle probably has to be improved due to the difficulty of measuring the exchange current density at that time.

By considering diffusion and migration, Chazalviel [126] showed analytically and numerically the existence of space charge region in the vicinity of cathode due to the depletion of anions. A characteristic time (Sand time) for building up this space charge region can be an explanation of incubation and is probably close to incubation time. The dendrite growth speed is equal to the velocity of anions, proportional to anion mobility and electrical field in the neutral region. The pinpointing of space charge, constituted a milestone finding in this field. The growth rate was confirmed experimentally by Fleury, et al [127] in copper sulfate and copper acetate electrolytes, but not confirmed by Devos [128] in copper sulfate electrolyte added by oxalate ions.

Fleury, et al [129][130][131][132] investigated the role of convection in the dendrite growth process and found that the space charge created electro-convective motions in the vicinity of dendrites, forming contra-rotative vortices between neighboring branches. With the increase of convection, the space charge size decreases. In a higher concentration binary electrolyte, the gravity-induced convection may also play a role [133], probably down to a 70 μm-thick cell [134]. Marshall, et al

[135][136][137][138][139] simulated the dendrite growth process using Nernst Planck equation (ion transport), Poisson equation (potential profile) and Navier-Stokes equation (hydrodynamic flow) and demonstrated the evolution of gravity induced convective tube and electro-convective rings, qualitatively matching the experimental results. These studies [129]-[139], have cast a deep insight into the role of convection in this process.

By assuming migration control in the incubation period, Bradley [140] concluded that incubation time in spatially coupled bipolar electrodes (SCBE) is proportional to the gap distance between electrodes and the inverse of cation mobilities and electrical field. This was simulated by Marshall [141] in electrochemical deposition (ECD) and SCBE and provided qualitative agreement with experimental results. These studies, together with Chazalviel and Fleury's work, clarified the role of cation mobility in incubation period and anion mobility in growth period.

These studies have provided a strong background about dendrites initiation and growth, but there exist three differences between ECD in electrochemistry and ECM on electronics, which may limit the application of these theories to ECM. First, the ion transport media on electronics is adsorbed moisture film, or bulk water resulting from the condensation during thermal cycling conditions (power on and power off, transition from a hot environment to a cold environment, etc.). The thickness of ion transport media may constrict the influence of convection. Second, the ionic strength

in the media is relatively low compared to ECD solutions which contain electroactive ions and possibly supporting electrolyte. Third, the electroactive ions (Cu^{2+}, Zn^{2+}, etc) are readily available for deposition in ECD, while there are no electroactive ions in the transport media prior to the application of potential difference in ECM.

DiGiacomo [142] developed a model to consider the chances of condensation on substrate surfaces and describe the TTF as the ratio of circuit physical parameters to environmental stress conditions (temperature, humidity and potential difference). This model assumed dendritic growth is migration controlled and predicted the TTF is proportional to the inverse of voltage or square of voltage depending on the curve fitting of experimental results. Yang, et al [143], developed an overall regression model using environmental stress conditions. However, there is a lack of physicochemical model which can explain the physical processes and be used to predict the TTF of ECM on electronics.

This study focuses on adjusting the theories on ECD and applying them to ECM under condensed conditions. Then the model developed is extended to non-condensing conditions. Electrochemical impedance spectroscopy (EIS) is used to obtain charge transfer resistance R_{ct}, which helps to calculate the surface concentration of electro-active ions at anode. Nernst Planck equations are used to model the ion transport and calculate the incubation time and growth time. Finally the

previous ECD models are applied to our experimental results and compared with the model of this study.

4.2 Theoretical Model of Copper Ion Transport Time

Figure 1 shows the different steps of the ECM process under the deionized water drop test. A failure is defined as the drastic current change from the initial current due to the abridgement of dendrites across the gap. The TTF is defined as the sum of incubation time and growth time. Incubation time is the time needed to initiate embryonic dendrites, which is the sum of ion dissolution, transport, and deposition time until a critical amount are deposited at cathode to be detectable. The growth time is the time from the appearance of embryonic dendrites, via propagation of dendrites, until abridgement of dendrites between anode and cathode. The ending of growth time is reflected in the current-time curve as a drastic change of current (end of zone 2 in Figure 11).

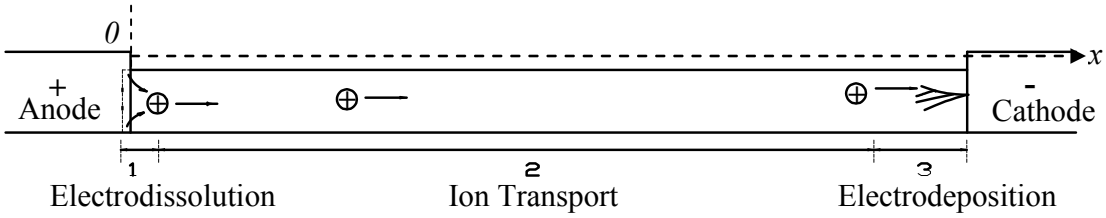

Figure 1: Steps of transportation process for ECM under deionized water.

Assume $A_{\gamma_1}B_{\gamma_2}$ is the binary electrolyte with a charge number z_1, z_2, respectively. Assume A is electroactive, and B is inert. Based on the Nernst-Planck equation and assuming convection does not dominate the process,

$$J_1 = -D_1 \frac{\partial c_1}{\partial x} - \mu_1 c_1 \frac{\partial \phi}{\partial x} \qquad (1)$$

$$J_2 = -D_2 \frac{\partial c_2}{\partial x} - \mu_2 c_2 \frac{\partial \phi}{\partial x} \qquad (2)$$

where J is the ionic flux density, D is the diffusivity, c is concentration, μ is the ionic mobility, F is Faraday's constant, ϕ is the potential, and x is distance. "*1*" represents electroactive ions, and "*2*" represents inert ions. These two equations include diffusion and migration terms. Diffusion is driven by concentration gradient $\partial c / \partial x$, while migration is driven by potential gradient $\partial \phi / \partial x$. From the continuity equation in the absence of homogenous reaction in the solution,

$$\frac{\partial c_i}{\partial t} = -\nabla \cdot J_i \qquad (3)$$

it is obtained that

$$\frac{\partial c_1}{\partial t} = D_1[\frac{\partial^2 c_1}{\partial x^2} + z_1 f \frac{\partial}{\partial x}(c_1 \cdot \frac{\partial \phi}{\partial x})] \qquad (4)$$

$$\frac{\partial c_2}{\partial t} = D_2[\frac{\partial^2 c_2}{\partial x^2} + z_2 f \frac{\partial}{\partial x}(c_2 \cdot \frac{\partial \phi}{\partial x})] \qquad (5)$$

where $f = \frac{F}{RT}$, $\mu = \frac{|z| FD}{RT}$ (based on Einstein-Smoluchowski relation). Since $\frac{c_1}{\gamma_1} = \frac{c_2}{\gamma_2} = c_s$, where c_s is the salt concentration, from (4) and (5) one can get

$$\frac{\partial c_s}{\partial t} = D_s \frac{\partial^2 c_s}{\partial x^2} \qquad (6)$$

where $D_s = \frac{D_1 D_2 (z_1 - z_2)}{z_1 D_1 - z_2 D_2}$. Equation (6) describes the salt concentration as a function of time and space. It can be solved by the Laplace transformation with boundary conditions:

$$c_s(x,0) = a \quad \text{(Initial bulk concentration of electroactive ions)} \qquad (7)$$

$$c_s(0,t) = c_s^0 \quad \text{(Assume surface concentration at anode is a constant)} \qquad (8)$$

$$c_s(L,t) \equiv 0 \quad \text{(Assume the surface concentration is zero at cathode)} \qquad (9)$$

In practice the magnitude of the overpotential at cathode can be large enough to cause the surface concentration at cathode to be zero. By using Fourier series, the solution of (6) with boundary conditions (7), (8) and (9) is

$$c_s(x,t) = c_s^*(x,t) + c_s^{\sim}(x,t) = \frac{v}{L}x + ab + \sum_{n=1,2\ldots}[\frac{2u}{n\pi}(1-\cos n\pi) + \frac{2v}{n\pi}\cos n\pi]e^{-\frac{n^2\pi^2 D_s t}{L^2}}\sin\frac{n\pi}{L}x$$

(10)

$$J_1 = -D_s(\frac{v}{L} + \sum_{n=1,2\ldots}\frac{n\pi}{L}[\frac{2u}{n\pi}(1-\cos n\pi) + \frac{2v}{n\pi}\cos n\pi]e^{-\frac{n^2\pi^2 D_s t}{L^2}}\cos\frac{n\pi}{L}x) \qquad (11)$$

where

$$u = a(1-b) \qquad (12)$$

$$v = a(d-b) \qquad (13)$$

$$b = \frac{1}{\gamma_1}e^{z_1 f \Delta E_1} \qquad (14)$$

$$d = \frac{1}{\gamma_1}e^{z_1 f \Delta E_2} \qquad (15)$$

and $^{\Delta E_1}$, $^{\Delta E_2}$ are the overpotentials at the anode and cathode, respectively.

If a=0, the solutions (10) and (11) become trivial. Under this case, an approximate solution when a=0 can be found to be

$$c_s(x,t) = c_s^0(1-\frac{x}{L})(1-erf(\frac{x}{2\sqrt{D_s t}})) \qquad (16)$$

where $c_s^{\,0}$ is the surface concentration of electroactive ions at the anode and L is the gap length.

From Equations (4), (5) and (6),

$$D_s \frac{\partial^2 c_s}{\partial x^2} = D_1[\frac{\partial^2 c_s}{\partial x^2} + z_1 f \frac{\partial}{\partial x}(c_s \cdot \frac{\partial \phi}{\partial x})] \qquad (17)$$

By integrating both sides and using the boundary condition $c_s(L, 0)=0$, it is obtained that

$$c_s \cdot \frac{\partial \phi}{\partial x} = \frac{D_s - D_1}{D_1 z_1 f} \frac{\partial c_s}{\partial x} \qquad (18)$$

From Equation (1), it is obtained that

$$J_1 = \frac{c_s^0 D_s}{L}\left[1 - erf(\frac{x}{2\sqrt{D_s t}})\right] + (1 - \frac{x}{L})\frac{c_s^0 \sqrt{D_s}}{\sqrt{\pi t}} e^{-\frac{x^2}{4D_s t}} \qquad (19)$$

which is the flux density profile of the electroactive ions. So Equations (10) and (11) are the concentration and flux density profile if the initial bulk concentration of electroactive ions $a \neq 0$; Equations (16) and (19) are the approximate concentration and flux density profile if the initial bulk concentration of electroactive ions $a=0$.

Assume Cu^{2+} is the electroactive ion, the initial bulk concentration of Cu^{2+} is 0 mol/L, the surface concentration of Cu^{2+} at anode is 10^{-6} mol/L after the application of potential difference, L=0.635 mm, $D_1 = D_{Cu^{2+}} = 3.67 \times 10^{-10} m^2/s$, $D_2 = D_{OH^-} = 5.24 \times 10^{-9} m^2/s$, and $D_s = 9.88 \times 10^{-10} m^2/s$. Then a simulation of the concentration profile in the copper electrodes-DI water system is shown in Figure 2.

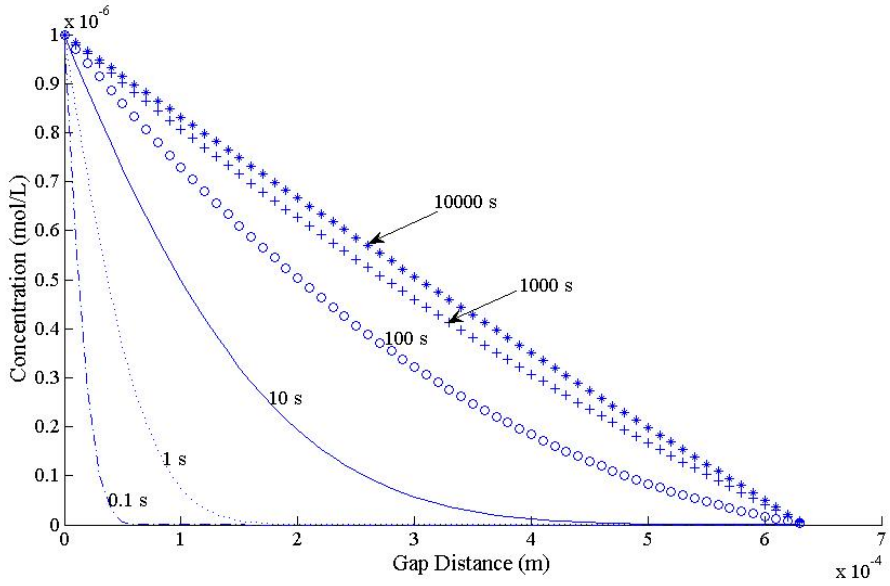

Figure 2: A simulation of electroactive species concentration kinetics based on Equation (10).

So it can be observed that as the ions transport from anode (left side) to cathode (right side) in Figure 1, it takes some time for the frontier of copper ions to reach the cathode. After 10,000 s, the Cu^{2+} ion profile finally becomes a straight line (star line). A simulation based on Equation (19) is shown in Figure 3. This indicates that during the non-stationary process, the flux density of electroactive ions across the gap is different: the closer to the anode, the higher the flux density. Until a sufficient amount of time passes (1000 s in this case, star line), the flux densities at different points across the gap become equal, and therefore the stationary state of the system is established.

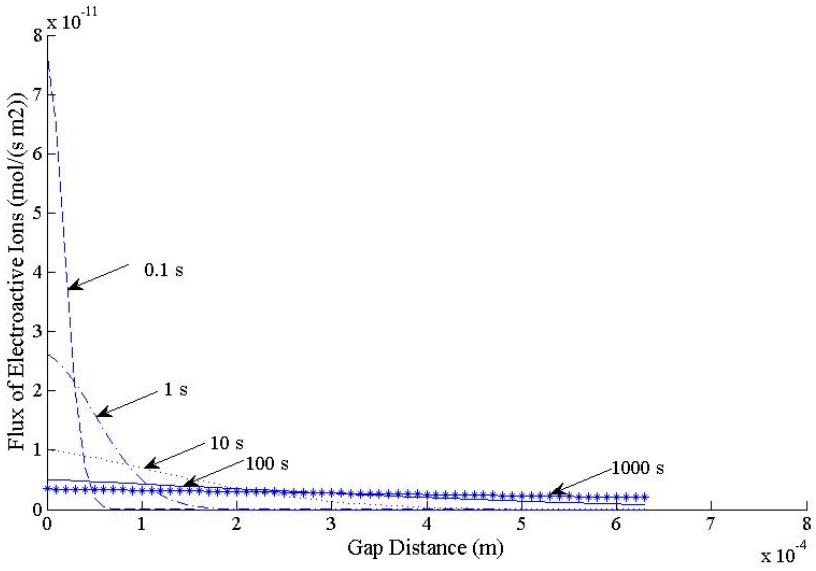

Figure 3: The flux density profile of the electroactive ions assuming that Cu^{2+} is the electroactive ion, the initial bulk concentration is 0 mol/L, and the surface concentration at the anode is 10^{-6} mol/L.

Based on Equation 19, the flux density at cathode ($x=L$) is

$$J_1(L,t) = \frac{c_s^0 D_s}{L}\left[1 - erf\left(\frac{L}{2\sqrt{D_s t}}\right)\right] \qquad (20)$$

and a simulation is shown in Figure 4. The area below the curve is proportional to the cumulative amount of deposited embryonic dendrites at the cathode.

Assume that the embryonic dendrites grow as small hemispheres with a radius of r; so until they reach critical dimensions, they cannot be detected. The minimum detectable dimension by human eyes is about 0.1 mm [144]. Since a magnification of 60 times was used for the optical microscope, the critical radius of embryonic dendrites is

$$r_{crit} = 0.1 \times 10^{-3} / (2 \times 60) = 8.3 \times 10^{-7} m \qquad (21)$$

Due to mass conservation, the flux density at cathode in a short period of time dt in a length of $2r$ should result in the growth of dendrites in a small radius dr,

$$M \cdot 2r \cdot J_1(t) \cdot dt = 2\pi r^2 \cdot dr \cdot \rho \qquad (22)$$

By separating variables and integrating both sides, it was obtained that

$$\int_0^{t_1} MJ_1(t)\,dt = \int_0^{r_{crit}} \pi r \rho\, dr \qquad (23)$$

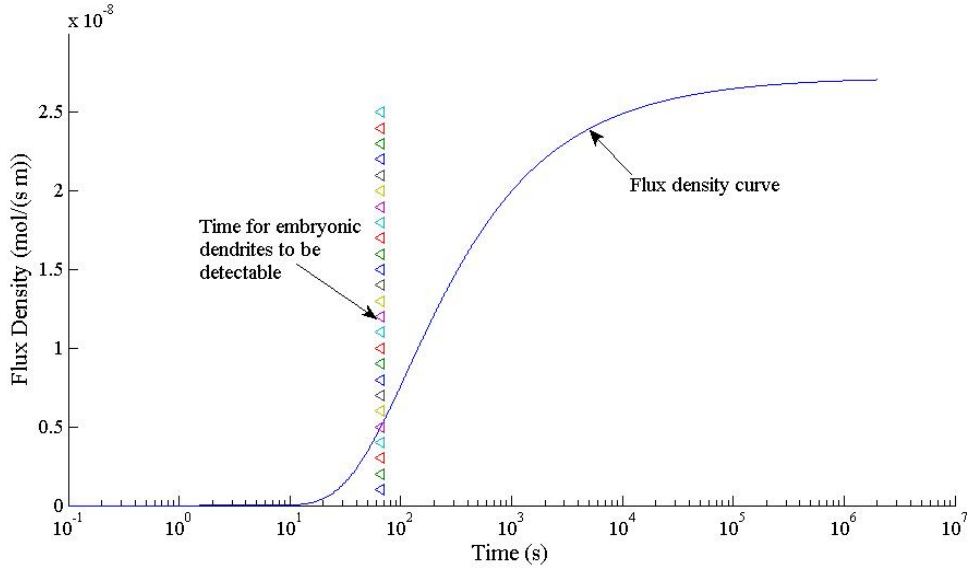

Figure 4: The kinetics of the flux of the electroactive ions at cathode (*x*=*L*) and the time for embryonic dendrites to grow long enough to be detectable. Assume the electroactive species are copper ions, the initial bulk concentration is 0 mol/L and the anode surface concentration C_s^0 is 10^{-6} mol/L.

Then

$$\int_0^{t_1} J_1(t)\cdot dt = \int_0^{r_{crit}} 2\,dr \cdot \rho / M = 2\rho / M \int_0^{r_{crit}} dr = 2\rho r_{crit} / M \qquad (24)$$

where M is the atomic weight of deposited metal, and ρ is the density of deposited metal. $J_1(t)$ is flux density, as given by Equation (20), so the time for the embryonic dendrites to grow and be detected, the incubation time t_1, can be found by integrating $J_1(t)$ with time and equating it to the cumulative deposited amount with a critical radius of r_{crit}, the right side of Equation (24). This step was conducted by programming in Matlab and then simulated, as shown in Figure 4. Assume the anode

surface concentration, C_s^0, of copper ions is 10^{-6} mol/L; then the time for embryonic dendrites to be detectable is 66 s.

For the dendrite growth process, regardless of how complex the morphology of dendrites is, there is always a trunk of dendrites propagating toward and almost being perpendicular to the anode, so based on mass conservation, the propagated length *dl* in a time period *dt* bears the following

$$J_1 \cdot A = \frac{dl \cdot A \cdot \rho}{Mdt} \tag{25}$$

where *A* is the cross sectional area of dendrites. Then

$$\upsilon = \frac{dl}{dt} = \frac{J_1 \cdot M}{\rho} \tag{26}$$

where υ is the dendrite growth speed, which depends on the ionic flux density. So

$$\int_{t_1}^{t_2} J_1 \cdot dt = \int_0^L \frac{\rho}{M} dl = \frac{\rho}{M} L \tag{27}$$

where t_2 is the time at which dendrites touch anode, so t_2-t_1 is the growth time. Since J_1 is already given in Equation (19), t_2-t_1 can be obtained through integration, similar to the way to calculate t_1 from Equation (24). So Equations (24) and (27) are the schemes to describe and numerically acquire incubation time and growth time, respectively. The difference lies in that for incubation time, the flux density profile changes with time, as specified by Equation (20), while for growth time, the flux density profile changes with time and space, as specified by Equation (19).

In order to resolve the surface concentration of electroactive ions at anode, it is assumed that charge transfer rate is so fast that Nernst equation holds, so

$$\phi_{anode} + \Delta V_{Ag/AgCl\_SHE} - IR_{ct\_anode} = \phi^0_{SHE} + \frac{RT}{ZF}\ln c_1^0 \qquad (28)$$

$$c_1^0 = e^{\frac{zF}{RT}(\phi_{anode}+\Delta V_{Ag/AgCl\_SHE}-IR_{ct\_anode}-\phi^0_{SHE})} \qquad (29)$$

where ϕ_{anode} is the measured potential of anode relative to Ag/AgCl reference electrode, $\Delta V_{Ag/AgCl\_SHE}$ is the potential difference between Ag/AgCl reference electrode relative to standard hydrogen electrode, I is current, R_{ct_anode} is the charge transfer resistance at anode, IR_{ct_anode} is the potential consumed in charge transfer at anode-electrolyte interface, ϕ^0_{SHE} is the standard hydrogen electrode potential, c_1^0 is the anode surface concentration of electroactive ions. So Equation 28 describes the relation between the surface concentration of electroactive ions, current, charge transfer resistance, and measured anode potential if a local equilibrium at anode can be built up. Equation 29 is used to calculate the surface concentration of electroactive ions at anode.

For the non-condensing condition, an approximation will be used. Since the ion transport media is an adsorbed moisture film, convection does not have to be considered. If we assume migration is the major transport mode and ignore diffusion, based on the relation between conductance and ionic mobility,

$$G = \frac{I}{U} = \frac{A_f}{L}k_I = \frac{A_f}{L}e_0 L_A(\gamma_1 z_1 c_1 \mu_1 + \gamma_2 z_2 c_2 \mu_2) \qquad (30)$$

where G is conductance, I is electrical current, A_f is cross sectional area of adsorbed moisture film or bulk water, k_I is conductivity, L_A is Avagadro's constant, e_0 is the

Table 1 A Summary of Models for Dendrites Incubation and Growth

	Incubation	Growth	Comments
Chazalviel	$\tau_s = \pi D(\frac{k_I}{2J\mu_a})^2$		Sand time, based on anion mobility
Bradley	$t_{incubation} = \frac{L}{\mu_c E}$		Based on cation mobility
Barton and Bockris		$t_{growth} = \frac{LRT}{i_0 V_m \eta}$	The equation when exchange current density i_0 is low. When i_0 is high, the equation does not apply to the scenario when initial bulk Cu^{2+} concentration is zero. V_m is molar volume.
Fleury		$t_{growth} = \frac{L}{\mu_a E}$	Based on anion mobility
This study	Equations 20, 24, 29	Equations 19, 27, 29	Bulk water electrolyte as ion transport media
	Equations 20, 24, 29, 32	Equations 19, 27, 29, 32	Adsorbed moisture film as ion transport media

unit electron charge. If we also assume the cation mobility and anion mobility change in the same way, it can be obtained that

$$G \propto k_I \propto \mu \propto D \tag{31}$$

so the ionic diffusivities in the adsorbed moisture film and in the bulk water are

$$D_{s\_film} = \frac{G_{film}}{G_{bulk}} D_{s\_bulk} \tag{32}$$

The ionic diffusivity in the adsorbed moisture film is calculated to be 3~4 orders of magnitude lower than the ionic diffusivity in the bulk water, based on conductance comparisons. Other parameters remain the same. Table 1 shows a summary of the models.

4.3 Experimental Results and Discussions

IPC B-25 multi-purpose test boards were used. The copper traces on the board have different spacings, 0.318 mm (12.5 mil), 0.635 mm (25 mil) and 1.27 mm (50 mil). The substrate was FR-4, a flame retardant resin epoxy composites reinforced by glass fibers. OSP finish was applied onto copper traces to prevent the oxidation of copper. In order to avoid the influences of other types of ions, 18.2-MOhm deionized water drops without supporting electrolyte were used as the electrolyte. The volume of water drops spanning copper metallizations was controlled with an AccuPet Pro pipette at 30 μL to maintain test repeatability. The environmental temperature was 18˚C. An optical microscope with 60 times magnification was used to monitor the dendrite growth. Potential differences across the gap were applied from 0.5 V to 5 V, with 0.5 V as the incremental step. The anodic potential was measured in-situ by a multi-meter with respect to Ag/AgCl reference electrode, shown in Figure 8. Currents were measured at 5 Hz by HP 34401A digital multimeter, which has a resolution of 0.1 μA. The experiments were repeated for 3~5 times for a given potential difference and spacing.

By inserting the tip (2 mm diameter) of micro-reference electrode into the water drop and not touching any copper trace, the anode and cathode potentials were measured. The equilibrium potentials at anode and cathode when the net current was zero ranged from -5 mV to 10 mV in general. A typical potential-time curve is shown in Figure 9. After the gap potential difference was applied, the anode and cathode potentials approached a plateau with time. Since the cathodic potential was quite negative, cathodic overpotential was so large that the Cu^{2+} surface concentration at cathode was practically zero. The anode potential was used to determine the surface concentration at anode. The anode potential increased with gap potential difference in general (Figure 10), with the averages being 22% of gap potential differences.

In order to obtain the surface concentration of Cu^{2+} at anode, the charge transfer resistance at anode was measured using Solartron 1287 electrochemical impedance spectroscopy (EIS). EIS measurement was performed independently from water drop testing with identical samples. The frequency ranged from 1 Hz to 10^6 Hz.

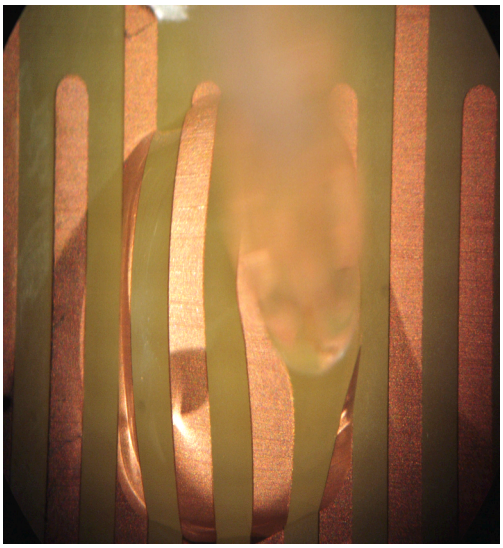

Figure 8: The tip of micro-reference electrode immersed in the water drop. Only the central pair of copper traces was powered.

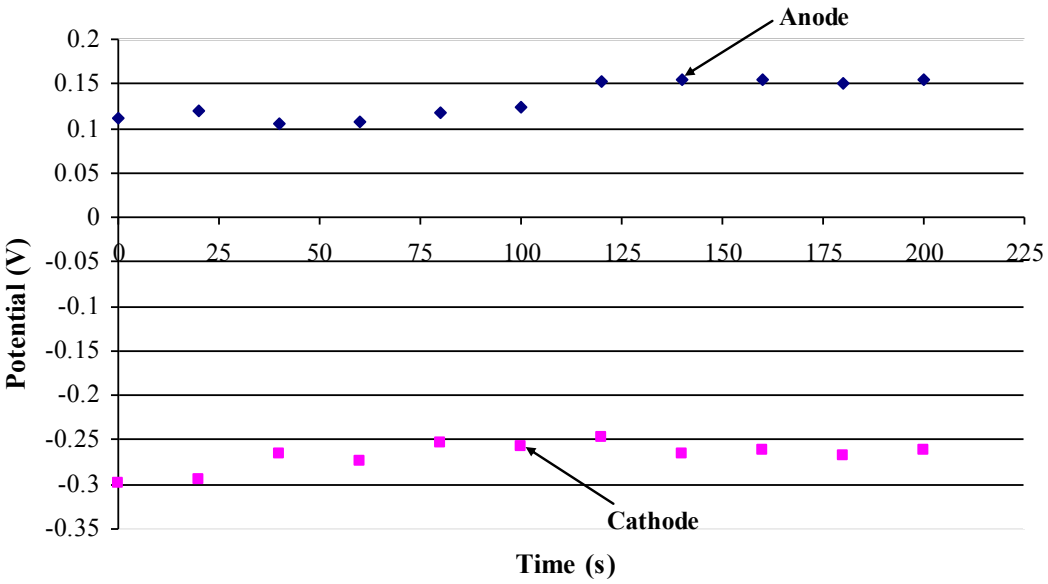

Figure 9: A typical anode potential curve with time when the gap potential difference was 0.5 V.

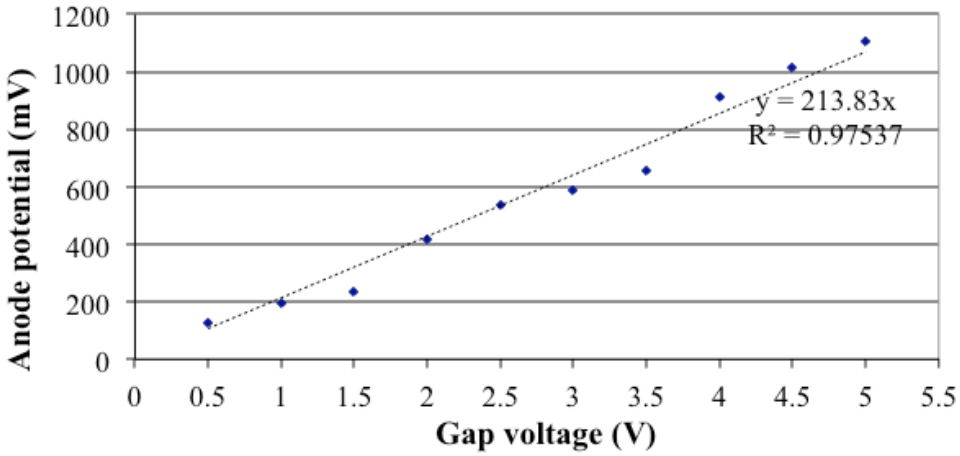

Figure 10: Anode potentials with respect to gap potential differences when the gap was 0.635 mm.

The current was almost constant during the incubation time and growth time. The initiation and growth of dendrites only caused small variations to the current. Each time one dendrite touched anode, the current jumped to a higher plateau, suggesting the addition of a new parallel resistor between the gap. As shown in Figure 11, zone 1

is the incubation period from application of bias to appearance of embryonic dendrite, zone 2 is the growth period from dendrite initiation until the first dendrite touched anode, and zone 3 is the period when successive dendrites touched anode one after another. Zone 4 corresponds to the removal of potential difference across the gap. Figure 12 shows some typical dendrites touching anode. The reason why "touching" did not short the circuit is because the resistances of dendrites themselves range from a few KOhms to a couple of hundred Kohms [145]. Figure 13 shows the current averages with respect to gap potential differences.

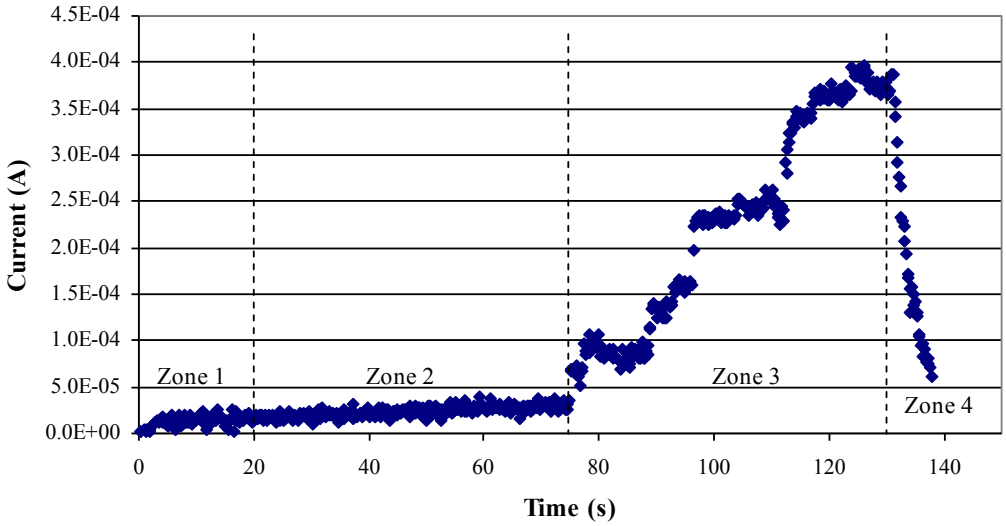

Figure 11: A typical current response with a 3.5 V potential difference across a 0.635 mm gap. Incubation time was 20 s and growth time was 56 s. The TTF was 76 s.

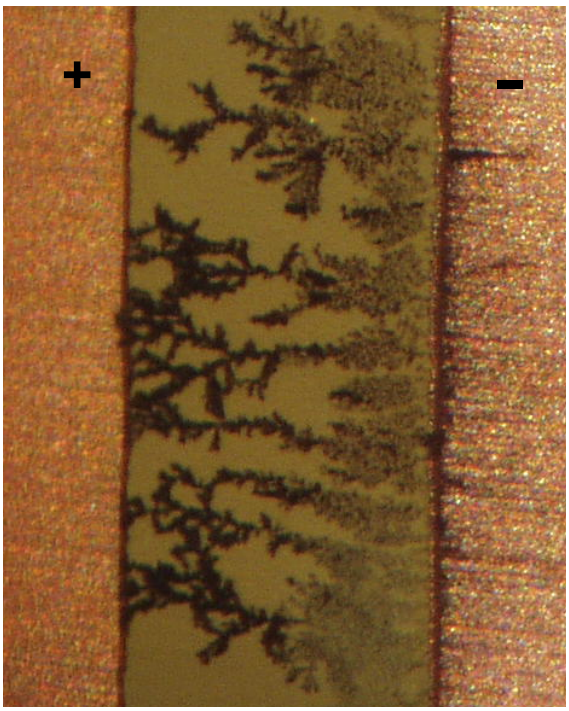

Figure 12: Typical dendrites abridged the gap.

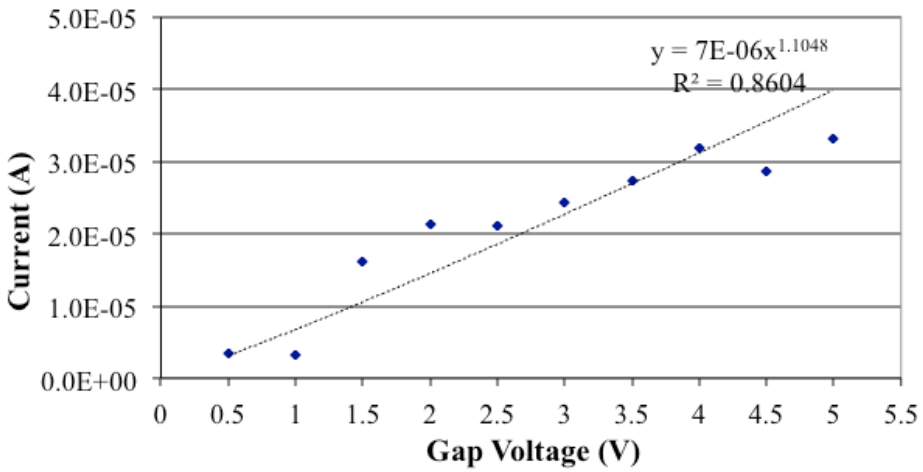

Figure 13: Cell current averages with respect to gap voltages.

By connecting the anode, cathode and reference electrode of the water drop testing setup to the corresponding electrodes of EIS, the anodic impedance was measured. Because the charge transfer resistance R_{ct} is the parameter of interest and it most likely corresponds to the high frequency region, the frequency was applied from 1 Hz to 10^5 Hz while omitting the time-consuming low frequency region (1 Hz~0.001 Hz).

In general the R_{ct} is independent of spacings and location of water drops on the comb structure. Table 2 shows the R_{ct}. A more detailed study on ECM kinetics using EIS is submitted elsewhere.

Table 2: Charge Transfer Resistances R_{ct}

Gap (mm)	0.635	0.317
Rct (Ohm)	12500	20000
	15000	37500
	20000	
	23000	
	37500	
Average (Ohm)	21600	28750

By applying anode potential, current and charge transfer resistance to Equation 29, the Cu^{2+} surface concentration at anode can be calculated. Averaged potentials and currents before dendrite abridging the gap were used. Taking Figure 11 as an example, the average potentials and currents in the first 76s (zone 1 and zone 2) were used. Then Cu^{2+} surface concentration is applied to Equation 20 to obtain the ionic flux at cathode, which is applied to Equation 24 and calculate the incubation time. So Equations 20, 24, and 29 constitute the modeling to acquire incubation time by taking into account both diffusion and migration effects. Figure 15 shows the comparison

between experimental, theoretical average incubation times and application of two historical models to the experimental results of this study.

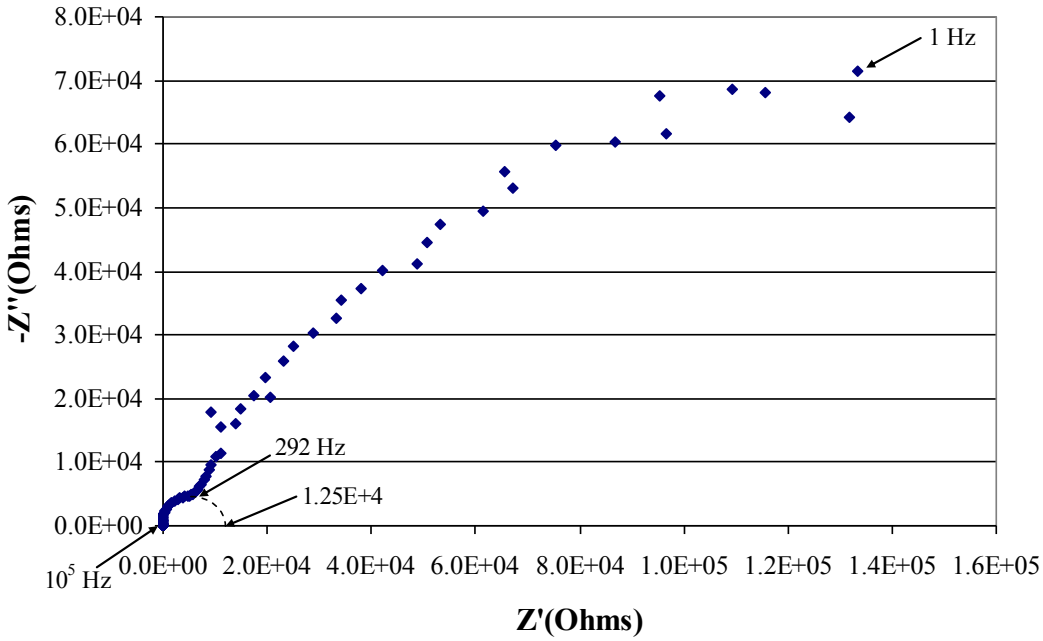

Figure 14: A typical anode impedance in Nyquist plot of EIS measurement data. The frequency ranged from 1 Hz to 10^5 Hz. The charge transfer resistance was 1.25×10^4 Ohms that is the crossing point between first imaginary semi-circle and x-axis.

It can be seen that Chazalviel and Devos's model shows similar trend in matching up our experimental results, but it is still less accurate than our model, especially when the gap potential difference is less than 4V. Bradley and Marshall's model catches the general trend of experimental results, but seems to predict the TTFs much faster than the experimental times. This is probably due to their assumption of migration control only in the incubation period. However, diffusion and migration always exist at the

same time in the incubation period, since the concentration gradient and electrical field always co-exist.

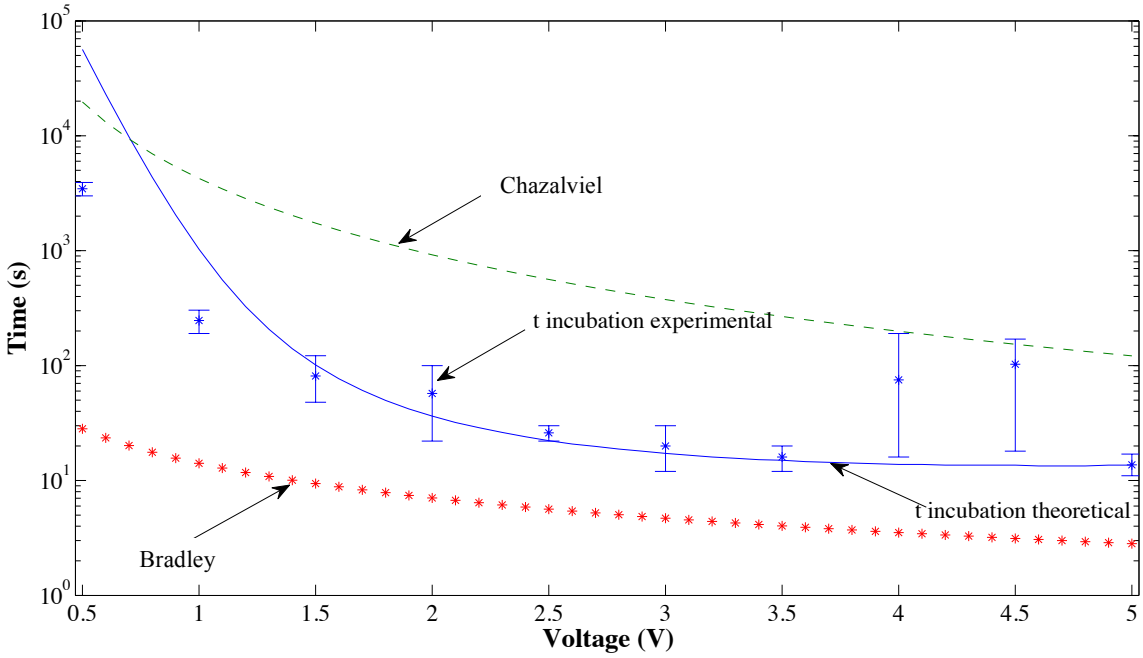

Figure 15: Comparison between theoretical and experimental incubation time.

Similarly, by applying Equations 19, 27, 29, the growth time can be calculated. Figure 16 shows the comparison between the experimental, theoretical average growth times and application of two historical models to the experimental results of this study. It can be seen that Barton and Bockris's model deviates from our experimental results by 3~4 orders of magnitude, which is probably caused by the electrolyte difference. Barton and Bockris used $NaNO_3$ and KNO_3 supporting electrolyte together with $AgNO_3$ to grow Ag deposits. The existence of Ag^+ prior to application of potential difference renders the cell under a mixed control (charge transfer and ion transport) at cathode, while the DI water electrolyte in this study does not have any supporting electrolyte and electroactive ions (Cu^{2+}) prior to application of potential difference, so

the whole cell is regulated by the thermodynamics at anode boundary and controlled by migration and diffusion in the ion transport process.

Fleury's model shows a difference of 2~3 orders of magnitude from our experimental results. Fleury claimed that growth speed is proportional to anion mobility and electrical field. A dendrite's growth speed is accompanied by the dendrite's pushing away anions toward anode and piling them up in an increasing concentration gradient toward anode. This assumption was confirmed experimentally in copper sulfate and acetate solutions [127]. However, in a DI water electrolyte, the major anion is OH^-, if the influences from other exterior ions such as bicarbonate are excluded. The mobility of OH^- is much higher than Cl^-, SO_4^{2-}, or NO_3^- due to a different transport mechanism. Anions like Cl^-, SO_4^{2-}, or NO_3^- physically transport from cathode toward anode, but the movement of OH^- is caused by tunneling of protons (H^+) and reorientation of water molecules in a direction favored by electrical field. It is not the movement of the very OH^- ion that transports from cathode to anode, but the tunneling of a proton through reorientation of water molecules from anode toward cathode that leaves behind another OH^- at anode [146]. So OH^- does not physically transport from cathode to anode. This is perhaps the reason why Fleury's model does not apply to our DI water electrolyte case. Figure 17 shows the comparison among our theoretical and experimental overall TTF which is the sum of incubation and growth time. Figure 18 is the comparison between overall theoretical and experimental TTF by fixing the gap potential difference but varying gap distances.

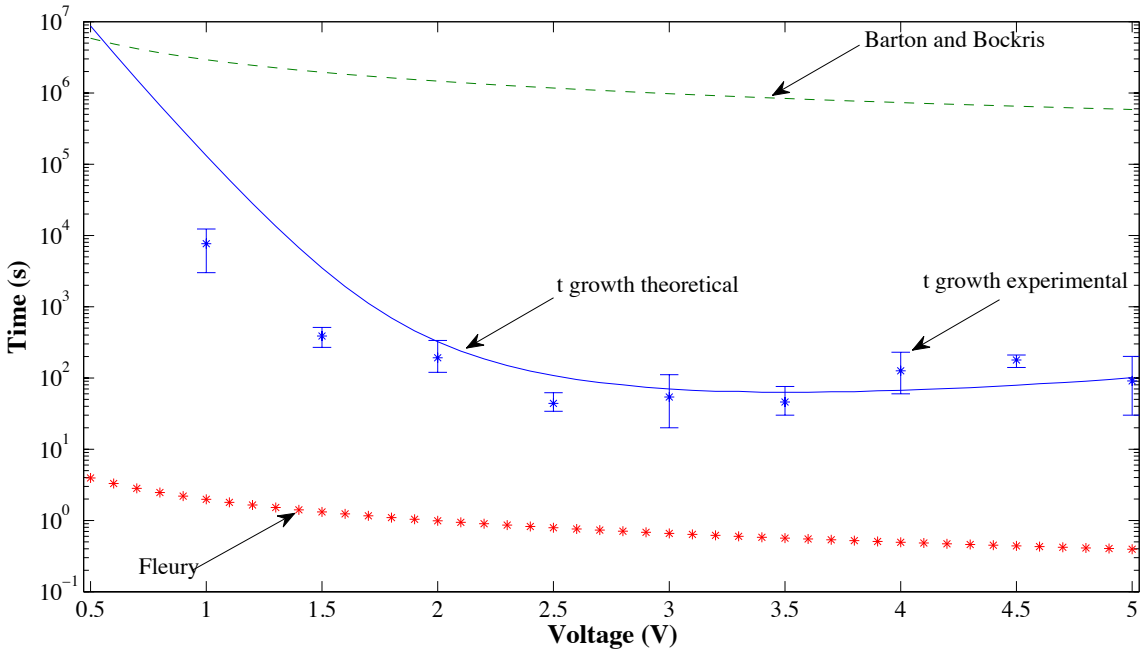

Figure 16: Comparison between theoretical and experimental growth time.

From Figure 17, it can be seen that a higher potential difference does not necessarily result in a shorter TTF, especially when the potential difference is above 4 V. The reason is because a higher potential difference generates a higher concentration at anode, which results in lower ion mobility, although the electrical driving force is higher. Also at a higher potential difference, such as above 4 V, the chances to generate air bubbles at cathode increase, which may partially block the surface of cathode, lowering the chances to grow dendrites and increasing the growth time. So this implies industrial standards concerning the water drop test do not necessarily need to use a harsh potential difference to reduce TTF. The IPC-TM-650, 2.6.13, "Assessment of Susceptibility to Metallic Dendritic Growth: Uncoated Printed Wiring", for example, discusses applying 15 V potential difference to copper metallizations with a DI water drop spanning a spacing of 15~30 mils. The ionic mobility decline with concentration and the oxygen bubble generation at cathode can

seriously decelerate the TTF, which probably makes a 15 V unnecessary and leads to unrepresentative results.

Also from Figure 17, we can see that the predicted curve is above the experimental results, which means the actual TTF is shorter than predicted TTF. The reason is probably because in the low potential difference region (<1.5 V), the exchange current density is lower than that in high potential difference region, the quasi-equilibrium cannot be built up, which makes Nernst equation not that feasible anymore. So the predicted TTF deviates from the experimental results more appreciably in low potential difference region than in high potential difference region.

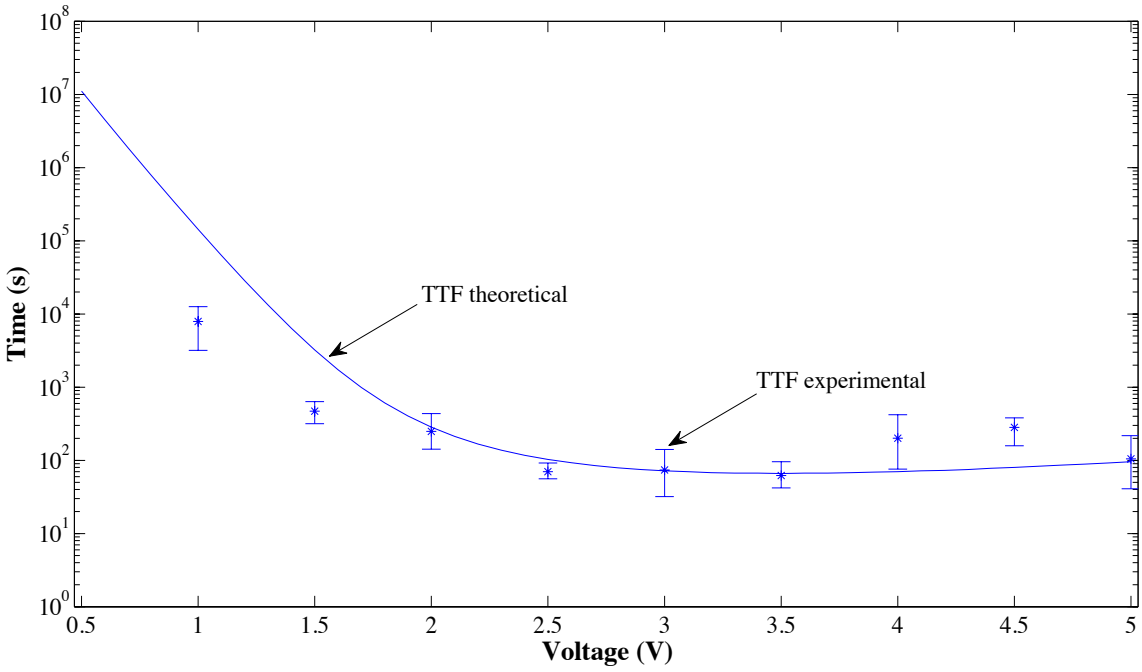

Figure 17: Comparison between overall theoretical and experimental TTF.

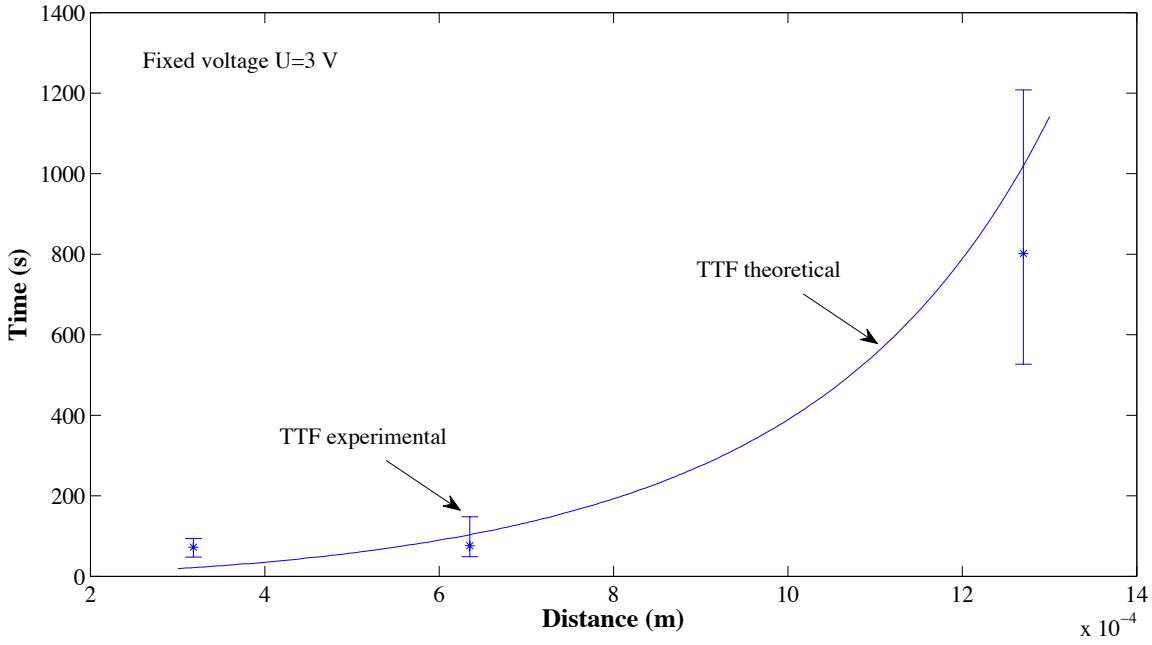

Figure 18: Comparison between overall theoretical and experimental TTF by varying gap distances.

In parallel to the water drop testing, identical comb structures were exposed to a non-condensing condition: 65C and 88% relative humidity with a 40 V potential difference applied across the gap. The test lasted for 1653 hours. In order to define the migration path, the residue of soldering flux (a chemical agent to help soldering on electronics) existed between electrodes before testing. Succinic organic acids were identified in the soldering flux residue to be 29 $\mu g/in^2$ by Ion Chromatography analysis. Due to the hygroscopic nature of soldering fluxes, a moisture film was preferentially formed where the flux residue was present. As shown in Figure 19, black copper dendrites formed at places bearing flux residues before the test. Since this was a non-condensing condition, the mobilities of Cu^{2+} and succinate ions were used to calculate the overall salt diffusivity inside the adsorbed moisture film using Equation 32. Table 3 shows the overall calculated diffusivities of Cu^{2+} cations with

hydroxide or succinate anions. Table 4 shows the TTFs of the test samples. The comparisons between theoretical and experimental TTFs indicate a general qualitative match, as shown in Figure 20.

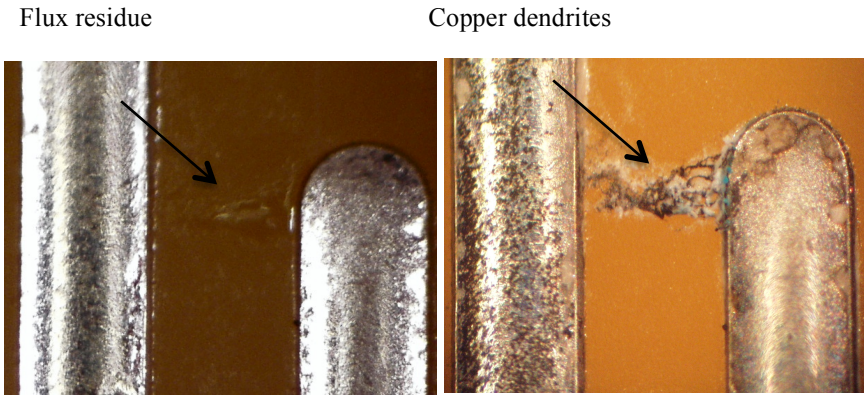

(a) (b)

Figure 19: A 0.635 mm comb structure exposed to 40V/65C/88%RH, (a): before test, (b): after test.

Table 3 Overall Calculated Diffusivities of Cu^{2+} Cations with Hydroxide or Succinate Anions

	Conductance in bulk water (S)*	Conductance in moisture film (S)*	Overall Ds in bulk water (m^2/s)	Overall Ds in moisture film (m^2/s)
$Cu(C_4H_4O_4)$	$8.84x10^{-6}$	$2.50x10^{-10}$	$3.84x10^{-10}$	$1.09x10^{-14}$
$Cu(OH)_2$			$9.88x10^{-10}$	$2.79x10^{-14}$

* Based on the overall average values from bulk water and moisture film conductance measurements on comb structures.

Table 4 Times to Failure Results of Non-condensing Environmental Test

Potential Difference (V)	Spacing (mm)	Time to Failure (hours)		
		Sample 1	Sample 2	Sample 3
40	0.635	Survived	188.9	Survived
	0.317	73.8	104.4	67.2

In general, the morphology is related to potential gradient. The potential gradient has to exceed a threshold value in order to trigger the growth of dendrites. Lower than the threshold value, layer deposition or powder deposition may result. A lower potential gradient results in a more random like fractal structure, while a higher potential gradient results in a more dendrite like structure with a preferential growth direction. Here the potential gradient controls the direction of dendrites, subjecting the growth to anisotropy instead of random noise. The higher the potential gradient, the more slim the dendrite looks, having a single trunk. The lower the potential gradient, the more stout or shrub like the dendrite is, lacking a single trunk. Based on Chazalviel, Fleury and Marshall's theories and simulations, the major potential drop is close to cathode. The potential gradient is little if close to anode, but steep and large if close to cathode. The closer to cathode (the farther to anode), the steeper the potential gradient is. This is why at cathode the potential gradient triggers the instabilities of deposition (thus growth of dendrites) and allows the dendrites to grow with it (toward anode).

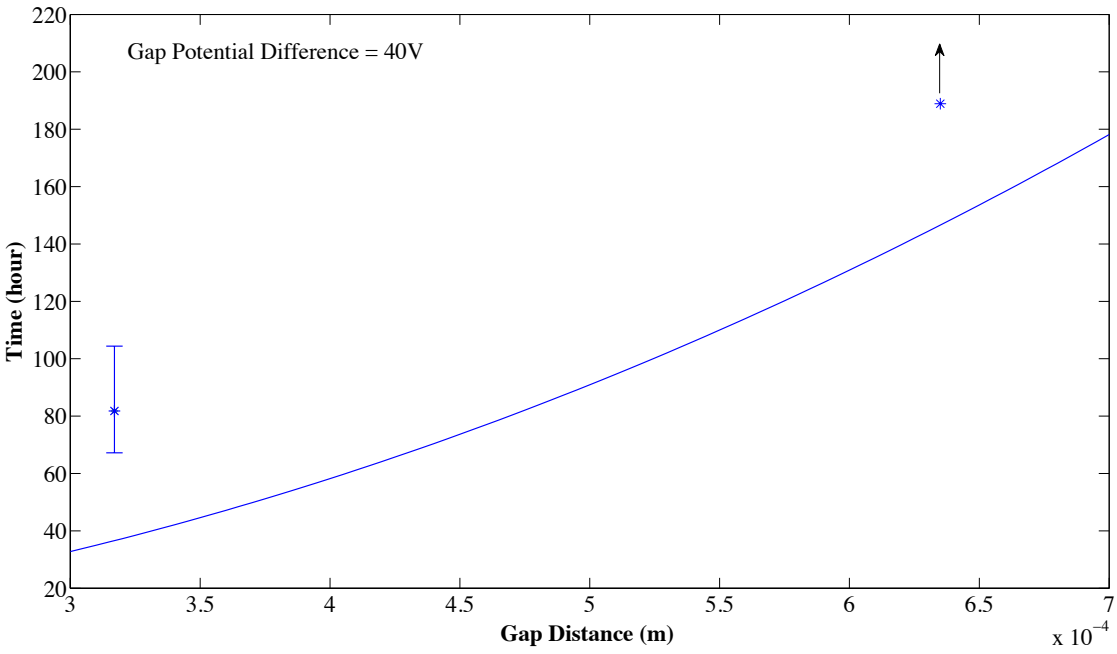

Figure 20: Comparison between overall theoretical and experimental TTFs in 65C/88%RH non-condensing condition. At 0.635 mm (25 mil) spacing, 2 samples survived the test while one sample failed at 188.9 hours.

4.4 Conclusions

To determine the overall failure times of biased PCB metallizations under condensed conditions, this study develops a physico-chemical model to characterize ECM process by adopting Nernst-Planck equation and electrochemical impedance measurement. Nernst Planck equation takes into account the diffusion and migration for ECM, while impedance measurement helps to determine the surface concentration and ionic flux of electroactive ions, thus uncovering the evolution of system flux profile during initiation and growth of dendrites.

Generally speaking, the model provided in this study is successful in determining and predicting the overall time to failure of copper electrodes-deionized water cell. The comparison between this model and historical models demonstrates that this model is better in the reign of DI water electrolytes. The reason is probably because when a bulk electrolyte forms on the relatively clean surface of PCBs, the absence of electroactive ions and supporting electrolyte prior to application of potential difference, renders the cell to be controlled by diffusion and migration in the electrolyte. The low concentration of electroactive ions, probably does not incur convection in a short time period, especially gravity induced convection. When an adsorbed moisture film becomes the ion transport medium, diffusion and migration dominate the cell without the influence of convection. However, our model can only provide a general qualitative match with experimental results in the adsorbed moisture film scenario. Due to the complex nature of electrochemical reactions at electrodes and the multi-driving forces in the transport media (diffusion, migration and convection), a model taking into account the controlling processes both at boundaries and in the transport media could have better accuracy than the ones only considering control process in the transport media.

Another feature of this model is to combine the *time domain* parameters-anode potential and cell current with the *frequency domain* parameter-charge transfer resistance. The advantage is that this method enables the thermodynamics at boundaries and kinetics in the bulk electrolyte to be considered together, but the

limitation is that the charge transfer resistance is not an in-situ measured parameter and may vary with time, thus compromising the accuracy of predicting time to failure, a *time domain* parameter. Thus a better model in future can be an in-situ measurement over parameters associated electrochemical reactions at interfaces and adopt them into ion transport kinetics.

Chapter 5

Conclusions and Future Work

5.1 Lead Free Solder ECM Propensity

IPC-B-24 comb patterns have been tested under THB conditions to evaluate the propensity of eutectic SnPb and lead free SAC solder to undergo ECM, and to assess the effects of board finish, electric field and spacing. A clear relationship between the electrochemical behavior and electrical behavior of different solders was established. The dendritic growth on the surface led to intermittent SIR drops, metal layer deposition resulted in a long term SIR decline, and the consumption of electroactive species generated the initial SIR increase right after humidity exposure, a characteristic of a diffusion-controlled cell. A model based on 3-D progressive and instantaneous nucleation was used to simulate the long term SIR decline and it matched the experimental data. The similarities between the simulation and experimental data indicate that both types of nucleation had occurred.

This study shows that SAC solder can exhibit failures under THB conditions if there is a long-term incompatibility between the fluxes and solder systems. The failure mechanism for the SAC boards, the deposition of metallic layers, was different from the dendritic growth often encountered on SnPb boards. The long-term deposition of metallic layers on the SAC boards necessitates the careful selection and evaluation of flux and solder systems to ensure their long-term compatibilities. The SIR results obtained with SAC solder demonstrate that THB tests of 500 hours or longer may be required to uncover reliability risks. SIR may exhibit a rising trend in the first 100-200 hours and give the impression of stabilization, whereas additional testing

may reveal problems that could threaten the reliability of electronic products which have long expected lifetimes.

A co-migration and co-deposition of Sn, Pb, and Cu on the SnPb board and Sn, Cu, and Ag on the SAC board was observed. The co-deposition of these metals was due to their low deposition potentials, which were in the milli-volt range, compared to the 5 V or 40 V applied bias. Although it has been argued by some researchers that Ag cannot migrate at room temperature due to its formation of intermetallic compounds, a small amount of Ag migration was observed in some samples in this study on SAC boards. Among the migrated species, Sn was predominant and manifested itself as layer deposits, Pb was predominant in the dendrites, while only a small proportion of the migrated metal was Cu. The occurrence of dendrites on SnPb boards tested at 40 V rather than at 5 V was attributed to the larger chance for the cathodic overpotential to exceed the critical cathodic overpotential and trigger dendritic growth under conditions of higher electrical stress.

The occurrence of ECM was influenced less by surface finish than it was by solder alloy. In the case of OSP this was attributed to the complexation of OSP during THB testing, which resulted in a non-detrimental green residue. In the case of HASL, the soldering process caused the HASL finish to dissolve into the solder, resulting in a final composition that was not sufficiently different from the nominal solder alloy composition to change its propensity for ECM compared to the OSP samples.

There was interaction between electric field and conductor spacing with respect to ECM. Within a spacing range from 12.5 mil (0.32 mm) to 25 mil (0.64 mm), when the electric field was relatively low (less than 1.6 V/mil), spacing was a stronger

factor than electric field in affecting ECM. When the electric field was relatively high (larger than 1.6 V/mil), electric field had comparable influence with spacing on ECM. With the current trend in the electronics industry towards miniaturization, higher density products would be expected to have greater risk of ECM overall, and to exhibit greater sensitivity to spacing than electric field. ECM's larger sensitivity to spacing implies that only lessening the electric field may not be sufficient to mitigate risk, and additional measures are needed to effectively suppress ECM.

5.2 Rate Limiting Step and Cell Kinetics

Potentiostatic applications, potentiodynamic scans, and electrochemical impedance spectroscopy were employed to study the kinetics of metal dissolution and dendritic growth on PCBs in DI water electrolyte. For the entire ECM process (before and during dendrite growth), anodic diffusion was the rate limiting step. This suggests that measures to suppress dissolution, such as coatings on Cu at the anode, could decrease ECM propensity and short circuits effectively.

This study also found that diffusion resistances decreased consistently with time during ECM with the exception of an abnormal increase in the anodic diffusive resistance due to the initiation of dendrites. But the traditional electrical current or SIR monitoring, as specified in IPC-TM-650 Method 2.6.14.1, detects an abnormal change of current or SIR only when dendrites touch the anode. This means the EIS is more sensitive than SIR monitoring in perceiving the physicochemical changes of the ECM process. Therefore, this study offers the electronics industry another option for how to detect dendritic growth by checking system impedances using EIS, in addition to the traditional current or SIR monitoring.

EIS impedance spectra indicate that OSP cannot effectively retard the dissolution of copper ions and suppress ECM in DI water electrolyte, although it can protect bare copper from being oxidized in air. This implies that electronics may incur ECM when condensation occurs between copper traces finished with OSP. This also suggests that EIS can be used to detect a coating's effectiveness to prevent ECM.

Finally, the identification of the anodic diffusion control and anodic charge transfer resistance values has helped to develop a physicochemical model of ECM to determine the concentration, flux density profiles, and time needed for dendrites to span the gap of electrodes on PCBs, which will be reported soon by the authors.

5.3 Physicochemical Model Development

To determine the overall failure time of biased PCB metallizations under condensed conditions, this study built a physico-chemical model to characterize the ECM process by adopting the Nernst-Planck equation and electrochemical impedance measurement. The Nernst-Planck equation takes into account the thermodynamic driving force (diffusion and migration in this case) for ion transport, while impedance measurement determines the electroactive ion concentration at the anode surface, thus uncovering the evolvement of the system flux density profile during initiation and propagation of dendrites.

The model provided in this study was successful in determining and predicting the overall time to failure of a copper electrodes-deionized water cell. A comparison between this model and historical models demonstrates that this model is better in matching the experimental results under DI water condition quantitatively. In the dendrite initiation period, Chazalviel's model shows similar matching to experimental results, but is still less accurate than the developed model. Other

models are far away from the experimental results of this study. The reason is because this model considers not only the charge transfer process at electrodes, but also the ion transport in the electrolyte, while the previous models always consider only the ion transport process. Barton and Bockris focused on diffusion control in the growth process, Bradley and Marshall assumed migration control in the initiation process, and Fleury assumed migration control in the growth process. Due to the complex nature of electrochemical reactions at the electrodes and the multi-driving forces in the ion transport (diffusion, migration and convection), a model taking into account the controlling processes both at the boundaries and in the bulk electrolyte can have better accuracy than the models that only consider the control process in the electrolyte.

The most distinct feature of this model is to combine the *time domain* parameters-anodic potential and cell current- with the *frequency domain* parameter-charge transfer resistance. The advantage is that this method enables the thermodynamics at boundaries and kinetics in the bulk electrolyte to be considered together, but the limitation is that charge transfer resistance is not an in-situ parameter and may vary with time, thus compromising the accuracy of predicting time to failure, a *time domain* parameter. Therefore, a future model can be an in-situ measurement over parameters associated with electrochemical reactions at interfaces and fit them into ion transport kinetics.

5.4 Future Work

The model developed in this study addresses the certainty about the TTF due to electrical stress and circuit geometrical feature, however, it does not address the randomness associated with the ECM. The theoretical curves by the model can

predict the averaged experimental times, but cannot predict the spread of experimental TTFs at each electrical stress condition due to the randomness of the experimental conditions, the possible unknown surface defects, the uncertainty associated with the dendrite growth process, etc. The randomness of growth process, has been addressed in the dielectric breakdown model (DBM) as a function of probability for a certain location on the dendrite tip to attract ions to deposit. In Marshall's simulation of dendrite growth process, this has been demonstrated. So, one future work can be to incorporate the randomness of growth process and simulate it in some way (such as Monte Carlo) and generate the min, max and standard deviations of TTFs at each electrical stress or spacing. So the future curve of TTFs will be a middle curve (certainty) with a shell of min and max curves (randomness).

References

[1] S. Chaikin, J. Janney, F. Church, and C. McClelland, “Silver Migration and Printed Wiring”, INDUSTRIAL AND ENGINEERING CHEMISTRY, VOL. 51, NO. 3, pp. 299-304, 1959.

[2] F. Ogburn, C. Bechtoldt, J. Morris, and A. de Koranyi, “Structure of Electrodeposited Lead Dendrites”, Journal of The Electrochemical Society, Vol. 112, No. 6, pp. 574-577, 1965.

[3] G. Marshall, and P. Mocskos, “Growth Model for Ramified Electrochemical Deposition in the Presence of Diffusion, Migration and Electro-Convection”, Physics Review E, Vol. 55, No. 1, pp. 549-563, 1997.

[4] G. Marshall, P. Mocskos, H. Swinney, and J. Huth, “Buoyancy and Electrically Driven Convection Models in Thin-Layer Electrodeposition”, Physics Review E, Vol. 59, No. 2, pp. 2157-2167, 1999.

[5] L. Hua, J. S. Zhang, “Corrosion Behavior of 64Sn-35Bi-1Ag Solder Doped with Zn in NaCl Solution and its Electrochemical Migration Characteristics in High Humid Thermal Condition for Electronic Packaging”, 2011 IEEE International Conference on Electronic Packaging & High Density Packaging, pp. 1034-1039, Shanghai, China, 2011.

[6] L. Hua, H. Hou, H. Zhang, T. Wu, Y. Deng, “Effects of Zn, Ge Doping on Electrochemical Migration, Oxidation Characteristics and Corrosion Behavior of Lead-Free Sn-3.0Ag-0.5Cu Solder for Electronic Packaging”, 2010 IEEE International Conference on Electronic Packaging & High Density Packaging, Xi’an, China, pp. 1151-1157, 2010.

[7] M. Moshrefi-Torbati and J. Swingler, “Reliability of Printed Circuit Boards Containing Lead-free Solder in Aggressive Environments”, J Mater Sci: Mater Electron, No. 22, pp. 400-411, 2011.

[8] B. Liu, T. Lee, and K. Liu, “Impact of 5% NaCl Salt Spray Pretreatment on the Long-Term Reliability of Wafer-Level Packages with Sn-Pb and Sn-Ag-Cu Solder Interconnects”, Journal of Electronic Materials, Vol. 40, No. 10, pp. 2111-2118, 2011.

[9] K. Hansen, M. Jellesen, P. Moller, P. Westermann, R. Ambat, “Effect of Solder Flux Residues on Corrosion of Electronics”, IEEE Annual Reliability and Maintainability Symposium, Fort Worth, TX, pp. 502-508, 2009.

[10] D. Minzari, F. B. Grumsen, M. S. Jellesen, P. Moller, and R. Ambat, “Electrochemical Migration of Tin in Electronics and Microstructure of the Dendrites”, Corrosion Science, No. 53, 2001, pp. 1659-1669.

[11] L. Hua, J. S. Zhang, “Corrosion Behavior of 64Sn-35Bi-1Ag Solder Doped with Zn in NaCl Solution and its Electrochemical Migration Characteristics in High Humid Thermal Condition for Electronic Packaging”, IEEE International Conference on Electronic Packaging Technology & High Density Packaging, Shanghai, China, 2011, pp. 1034-1039.

[12] D. Minari, M. S. Jellesen, P. Moller, R. Ambat, “On the Electrochemical Migration Mechanism of Tin in Electronics”, Corrosion Science, Vol. 53, 2011, pp. 3366-3379.

[13] S. Ho, S. Lian, K. Chen, J. Pan, T. Wang and A. Hung, “Studies of Ni-B as an Electrochemical Metal Migration Barrier”, IEEE Transactions on Components, Packaging, and Manufacturing Technology, part A, Vol. 19, No. 2, 1996, pp. 202-207.

[14] C. Gabrielli, L. Beitone, C. Mace, E. Ostermann, and H. Perrot, "Copper Dendrite Growth on a Microcircuit in Oxalic Acid", Journal of the Electrochemical Society, Vol. 154, No. 5, 2007, pp. H393-H399.

[15] O. Devos, C. Gabrielli, L. Beitone, C. Mace, E. Ostermann and H. Perrot, "Growth of Electrolytic Copper Dendrites II: Oxalic Acid Medium", Journal of Electroanalytical Chemistry, Vol. 606, 2007, pp. 85-94.

[16] L. Zou and C. Hunt, "Characterization of the Conduction Mechanisms in Adsorbed Electrolyte Layers on Electronic Boards Using AC Impedance", Journal of the Electrochemical Society, Vol. 156, No. 1, 2009, pp. C8-C15.

[17] C. P. Fabian, M. J. Ridd, M. E. Sheehan, and Ph. Mandin, "Modeling the Charge Transfer Resistance to Determine the Role of Guar and Activated Polyacrylamide in Copper Electrodeposition", *Journal of The Electrochemical Society*, Vol. 156, No. 10, 2009, pp. D400-D407.

[18] J. L. Barton and J. O'M. Bockris, "The Electrolyte Growth of Dendrites from Ionic Solutions", Proceedings-Royal Society of London. Series A, Mathematical, Physical and Engineering Sciences, Vol. 268, Iss. 1335, 1962, pp. 485-505.

[19] J. –N. Chazalviel, "Electrochemical Aspects of the Generation of Ramified Metallic Electrodeposits", *Physical Review A*, Vol. 42, No. 12, 1990, pp. 7355-7367.

[20] V. Fleury, M. Rosso, J. –N. Chazalviel, and B. Sapoval, "Experimental Aspects of Dense Morphology in Copper Electrodeposition", *Physical Review A*, Vol. 44, No. 10, 1991, pp. 6693-6705.

[21] J. C. Bradley, S. Dengra, G. A. Gonzalez, G. Marshall, and F. V. Molina, "Ion Transport and Deposit Growth in Spatially Coupled Bipolar

Electrochemistry," *Journal of Electroanalytical Chemistry*, Vol. 478, 1999, pp. 128-139.

[22] G. Marshall, F. V. Molina, A. Soba, "Ion Transport in Thin Cell Electrodeposition: Modeling Three-ion Electrolytes in Dense Branched Morphology under Constant Voltage and Current Conditions," *Electrochimica Acta*, Vol. 50, 2005, pp. 3436-3445.

[23] G. Marshall, E. Mocskos, G. Gonzalez, S. Dengra, F. V. Molina, C. Iemmi, "Stable, Quasi-stable and Unstable Physicochemical Hydrodynamic Flows in Thin-Layer Celle Electrodeposition", *Electrochimica Acta*, Vol. 51, 2006, pp. 3058-3065.

[24] G. DiGiacomo, "Metal Migration (Ag, Cu, Pb) in Encapsulated Modules and Time-to-Fail Model as a Function of the Environmental and Package Properties", Proceedings of IEEE 20thInternational Reliability Physics Symposium, San Diego, CA, Mar. 30/31, 1982, pp. 27–33.

[25] S. Yang and A. Christou, "Failure Model for Silver Electrochemical Migration", *IEEE Transactions on Device and Materials Reliability*, Vol. 7, No. 1, 2007, pp. 188-196.

[26] P. A. Kohl, "The High Speed Electrodeposition of Sn/Pb Alloys", *Journal of The Electrochemical Society: Electrochemical Science and Technology,* Vol. 129, No. 6, 1982, pp. 1196-1201.

[27] D. Shangguan, A. Achari, and W. Green, "Application of Lead-free Eutectic Sn-Ag Solder in No-Clean Thick Film Electronic Modules", *IEEE Transactions on Components, Packaging, and Manufacturing Technology,* Part B, Vol. 17, No. 4, 1994, pp. 603-611.

[28] T. Takemoto, R. Latanision, T. Eagar and A. Matsunawa, “Electrochemical Migration Tests of Solder Alloys in Pure Water”, *Corrosion Science*, Vol. 39, No. 8, 1997, pp. 1415-1430.

[29] G. Harsanyi, “Irregular Effect of Chloride Impurities on Migration Failure Reliability: Contradictions or Understandable?”, Microelectronics Reliability, Vol. 39, 1999, pp. 1407-1411.

[30] B. A. Smith and L. J. Turbini, “Characterizing the Weak Organic Acids Used in Low Solids Fluxes”, Journal of Electronic Materials, Vol. 28, No. 11, 1999, pp. 1299-1306.

[31] R. Manepalli, F. Stepniak, S. Bidstrup-Allen, and P. Kohl, “Silver Metallization for Advanced Interconnects”, IEEE Transactions on Advanced Packaging, Vol. 22, No. 1, 1999, pp. 4-8.

[32] W. Jud Ready and L. J. Turbini, “A Comparison of Hourly Versus Daily Testing Methods for Evaluating the Reliability of Water Soluble Fluxes”, IEEE Transactions on Advanced Packaging, Vol. 23, No. 2, 2000, pp. 285-292.

[33] S. Yoshihara, H. Tanaka, F. Ueta, K. Kumekawa, and H. Hiramatsu, “Newly Developed Real Time Monitoring System for Ionic Migration of Lead Free Solder by Means of Quartz Crystal Microbalance”, 2001 IEEE 2nd International Symposium on Environmentally Conscious Design and Inverse Manufacturing, Tokyo, 2001, pp. 1064-1069.

[34] M. S. Moats, J. Brent Hiskey, and D. W. Collins, “The Effect of Copper, Acid, and Temperature on the Diffusion Coefficient of Cupric Ions in Simulated Electrorefining Electrolytes”, Hydrometallurgy, Vol. 56, 2000, pp. 255-268.

[35] K. Mondal, J. Pattanayak, N. Mandich, T. Wiltowski, and S. Lalvani, "Modeling of a Process for Removal of Metal Ions by Electromigration and Electrodeposition", The Canadian Journal of Chemical Engineering, Vol. 80, 2002, pp. 465-471.

[36] T. Zapryanova, A. Danilov, and A. Milchev, "Growth Kinetics of Single Copper Crystals: the Concentration Dependence", Russian Journal of Electrochemistry, Vol. 46, No. 6, 2010, pp. 607-610.

[37] A. Carey, S. Wheatcraft, R. Glass, and J. O'Rourke, "Non-Fickian Ionic Diffusion across High-concentration Gradients", Water Resources Research, Vol. 31, No. 9, 1995, pp. 2213-2218.

[38] D. Q. Yu, W. Jillek, and E. Schmitt, "Electrochemical Migration of Sn-Pb and Lead Free Solder Alloys under Distilled Water", J Mater Sci: Mater Electron, Vol 17, 2006, pp. 219-227.

[39] D. Q. Yu, W. Jillek, and E. Schmitt, "Electrochemical Migration of Lead Free Solder Joints", J Mater Sci: Mater Electron, Vol 17, 2006, pp. 229-241.

[40] S. Zhan, M. H. Azarian, M. G. Pecht, "Surface Insulation Resistance of Conformally Coated Printed Circuit Boards with No-clean Flux", IEEE Transactions on Electronics Packaging Manufacturing, Vol. 29, No. 3, 2006, pp. 217-223.

[41] Y. Tsai, C. Hu, and C. Lin, "Electrodeposition of Sn-Bi Lead-Free Solders: Effects of Complex Agents on the Composition, Adhesion, and Dendrite Formation", Electrochimica Acta, Vol. 53, 2007, pp. 2040-2047.

[42] B. Noh and S. Jung, "Behavior of Electrochemical Migration with Solder Alloys on Printed Circuit Boards (PCBs)", Circuit World, Vol. 34, No. 4, 2008, pp. 8-13.

[43] C. Dominkovics and G. Harsanyi, “Fractal Description of Dendrite Growth during Electrochemical Migration”, Microelectronics Reliability, Vol. 48, 2008, pp. 1628-1634.

[44] Y. H. Xia, W. Jillek and E. Schmitt, “In-situ Observation on Electrochemical Migration of Lead-free Solder Joints under Water Drop Test”, 2008 IEEE Conference on Electronic Packaging Technology & High Density Packaging, Shanghai, China, 2008, pp. 1-5.

[45] S. Zhan, M. H. Azarian, and M. Pecht, “Reliability of Printed Circuit Boards Processed Using No-Clean Flux Technology in Temperature-Humidity-Bias Conditions”, IEEE Transactions on Device and Materials Reliability, Vol. 8, No. 2, 2008, pp. 426-434.

[46] S. Lee, M. Jung, H. Lee, T. Kang and Y. Joo, “Effect of Bias Voltage on the Electrochemical Migration Behaviors of Sn and Pb”, IEEE Transactions on Device and Materials Reliability, Vol. 9, No. 3, 2009, pp. 483-488.

[47] J. Jung, S. Lee, H. Lee, Y. Joo, and Y. Park, “Electrochemical Migration Characteristics of Eutectic Sn-Pb Solder Alloy in NaCl and Na2SO4 Solutions”, Journal of Electronic Materials, Vol. 38, No. 5, 2009, pp. 691-699.

[48] Y. R. Yoo and Y. S. Kim, “Influence of Electrochemical Properties on Electrochemical Migration of SnPb and SnBi Solders”, Metals and Materials International, Vol. 16, Iss. 5, 2010, pp. 739-745.

[49] L. Hua, and J. S. Zhang, “Corrosion Behavior of 64Sn-35Bi-1Ag Solder Doped with Zn in NaCl Solution and its Electrochemical Migration Characteristics in High Humid Thermal Condition for Electronic Packaging”, 2011 IEEE Conference on Electronic Packaging Technology & High Density Packaging, Shanghai, China, 2011, pp. 1034-1039.

[50] S. Lee, H. Lee, M. Jung, Y. Park, and Y. Joo, “Effect of the Composition of Sn-Pb Alloys on the Microstructure of Filaments and the Electrochemical Migration Characteristics”, Metals and Materials International, Vol. 17, Iss. 4, 2011, pp. 617-621.

[51] L. Mendes, V. Cardoso, A. Silva, “Electrochemical Migration on Lead-Free Soldering of PCBs”, Journal of Integrated Circuits and Systems, Vol. 6, No. 1, 2011, pp. 127-130.

[52] M. Pecht, E. Bumiller, D. Douthit and J. Pecht, *Contamination of Electronic Assemblies* (Boca Raton, FL: CRC, 2003).

[53] C. Lea, *A Scientific Guide to Surface Mount Technology* (Ayr, Scotland: Electrochemical Pub. Ltd., 1988).

[54] C. Dominkovics and G. Harsanyi, *Microelectron. Reliab.*, 48, 1628 (2008).

[55] G. Harsanyi, *IEEE Trans. Compon. Pack. A*., 18, 602 (1995).

[56] R. C. Benson, B. M. Romenesko, J. A. Weiner, B. H. Nall, and H. K. Charles, *IEEE Trans. Compon. Hybr.,* 11, 363 (1988).

[57] D. Q. Yu, W. Jillek, and E. Schmitt, *J. Mater. Sci.: Mater. El.*, 17, 229 (2006).

[58] S. M. Ho, S. M. Lian, K. M. Chen, J. P. Pan, T. H. Wang, and A. Hung, *IEEE Trans. Compon. Pack. A*, 19, 202 (1996).

[59] A. Shumka and R. R. Piety, *Proc. Int. Reliab. Phys. Symp.,* Las Vegas, NV, 93 (1975).

[60] Y. Awakuni and J. Calderwood, *J. Phys. D: Appl. Phys.*, 5, 1038 (1972).

[61] B. Yan, S. Meilink, G. Warren, and P. Wynblatt, *IEEE Trans. Compon. Hybr.,* CHMT-10, 247 (1987).

[62] L. Zou and C. Hunt, *J. Electrochem. Soc*., 156, C8 (2009).

[63] S. Zhan, M. H. Azarian and M. Pecht, *IEEE Trans. Electron. Pa. M*., 29, 217 (2006).

[64] IPC Publication IPC-TM-650, Method 2.6.14.1, *Electrochemical Migration Resistance Test* (Northbrook, IL: IPC, 2000).

[65] D. Q. Yu, W. Jillek, and E. Schmitt, *J. Mater. Sci.: Mater El.*, 17, 219 (2006).

[66] S. Zhan, M. H. Azarian, and M. Pecht, *Proc. 38th Int. Symp. Microelectron.,* Philadelphia, PA, 367 (2005).

[67] Joint Industry Standard, IPC J-STD-004, *Requirements for Soldering Fluxes* (Northbrook, IL: IPC, 2004).

[68] K. Kontturi, L. Murtomaki, and J. Manzanares, *Ionic Transport Processes in Electrochemistry and Membrane Science* (New York: Oxford University Press Inc., 2008).

[69] C. H. Hamann, A. Hamnett, and W. Vielstich, *Electrochemistry* (New York: Wiley-VCH, 1998).

[70] K. Takahashi, *J. Electrochem. Soc*., 138, 1587 (1991).

[71] M. Bendaoud, N. Bouchtout, F. Kaouah, and M. Saidi, *Proc. IEEE Int. Symp. Electr. Insul*., Toroto, Canada, 199 (1990).

[72] D. Das-Gupta, T. Welsh and A. Goodings, *Proc. IEEE Dielect. Mater. Meas. Appl.*, Canterbury, UK, 258 (1988).

[73] A. Saad and R. Tobazeon, *IEEE Trans. Electr. Insul*., EI-19, 193 (1984).

[74] P. Atkinson and R. Fleming, *J. Phys. D: Appl. Phys*., 13, 625 (1980).

[75] P. Atkinson and R. Fleming, *J. Phys. D: Appl. Phys*., 9, 2027 (1976).

[76] T. Chapman and H. Wintle, *J. Appl. Phys*., 51, 4898 (1980).

[77] M. Pepin and H. Wintle, *J. Appl. Phys*., 83, 5870 (1998).

[78] D. Das-Gupta, *IEEE Trans. Electr. Insul*., 27, 909 (1992).

[79] R. D. Armstrong, M. Fleischmann and H. R. Thirsk, *J. Electroanal. Chem.,* 11, 208 (1966).

[80] E. Bosco and S. K. Rangarajan, *J. Electroanal. Chem.,* 134, 213 (1982).

[81] M. Y. Abyaneh, V. Saez, J. Gonzalez-Garcia, and T. J. Mason, *Electrochim. Acta*, 55, 3572 (2010).

[82] A. Sinni and M. Palmer, *Proc. IEEE/CPMT Int. Electron. Manuf. Tech. Symp*., Austin, TX, 152 (1997).

[83] S. Zhan, M. H. Azarian and M. Pecht, *IEEE Trans. Device Mat. Re.,* 8, 426 (2008).

[84] J. Bradley, H. Chen, J. Crawford, J. Eckert, K. Ernazarova, T. Kurzeja, M. Lin, M. McGee, W. Nadler, and S. Stephens, *Nature*, 389, 268 (1997).

[85] IPC 9201A, *Surface Insulation Resistance Handbook* (Bannockburn, IL: IPC, 2007).

[86] R. Pandey, S. Sahu, and S. Chandra, *Handbook of Semiconductor Electrodeposition* (New York, NY: Marcel Dekker Inc., 1996).

[87] P. Kohl, *J. Electrochem. Soc*., 129, 1196 (1982).

[88] V. Maksimovic, M. Pavlovic, Lj. Pavlovic, M. Tomic, and V. Jovic, *Hydrometallurgy*, 86, 22 (2007).

[89] N. Nikolic, K. Popov, Lj. Pavlovic, and M. Pavlovic, *Surf. Coat. Tech*., 201, 560 (2006).

[90] D. Dobos, *Electrochemical Data, A Handbook for Electrochemists in Industry and Universities* (Amsterdam, Netherlands: Elsevier Scientific Pub. Co., 1975).

[91] Y. Li, *Proc. IEEE/CPMT Int. Electron. Manuf. Tech. Symp.*, Austin, TX, 56 (1997).

[92] E. Bradley and K. Banerji, *IEEE Trans. Compon. Pack. B*, 19, 320 (1996).

[93] E. C. Wagner and W. H. Millett, *Org. Synth.,* 2, 65 (1943).

[94] G. Mohamed, N. Ibrahim and H. Attia, *Spectrochim. Acta A*, 72, 610 (2009).

[95] K. Tellefsen, *Proc. Int. Conf. Electron. Assem: Mater. Process Challenges,* Atlanta, GA (1998).

[96] IPC Publication IPC-TM-650, Method 2.6.14.1, "Electrochemical Migration Resistance Test," Northbrook, IL: IPC, Sep. 2000.

[97] S. Zhan, M. H. Azarian and M. Pecht, "Surface Insulation Resistance of Conformally Coated Printed Circuits Boards Processed with No-Clean Flux," *IEEE Transactions Electronic Packaging Manufacturing*, Vol. 29, No. 3, pp. 217-223, July 2006.

[98] K. Takahashi, "Conduction Paths and Mechanisms in FR-4 Epoxy/Glass Composite Printed Wiring Boards," *Journal of Electrochemical Society*, Vol. 138, No. 6, pp. 1587-1593, 1991.

[99] C. Gabrielli, C. Mace, J. Matha, S. Mege, E. Ostermann, H. Perrot, "Investigation of Dissolution and Electrodeposition of Copper in Concentrated and Diluted Oxalic Media in Post-CMP Cleaning", *Solid State Phenomena*, Vol. 103-104, pp. 287-290, 2005.

[100] G. Marshall, F. V. Molina, A. Soba, "Ion Transport in Thin Cell Electrodeposition: Modeling Three-ion Electrolytes in Dense Branched Morphology under Constant Voltage and Current Conditions", *Electrochimica Acta*, Vol. 50, pp. 3436-3445, 2005.

[101] M. E. Huerta Garrido, M. D. Pritzker, "EIS and Statistical Analysis of Copper Electrodeposition Accounting for Multi-component Transport and Reactions", *Journal of Electroanalytical Chemistry*, Vol. 594, pp. 118-132, 2006.

[102] G. Marshall, E. Mocskos, G. Gonzalez, S. Dengra, F. V. Molina, C. Iemmi, "Stable, Quasi-stable and Unstable Physicochemical Hydrodynamic Flows in Thin-Layer Cell Electrodeposition", *Electrochimica Acta*, Vol. 51, pp. 3058-3065, 2006.

[103] O. Devos, C. Gabrielli, L. Beitone, C. Mace, E. Ostermann, H. Perrot, "Growth of Electrolytic Copper Dendrites. III: Influence of the Presence of Copper Sulphate", *Journal of Electroanalytical Chemistry*, Vol. 606, pp. 95-102, 2007.

[104] W. Lawson, R. D. Pilkington, and A. E. Hill, "Modeling and Analysis of the Growth of Copper Dendrites in Saturated Conditions Using A Multilevel Factorial Design Analysis", *Microelectronics International; Journal of ISHM-Europe, the Microelectronics Society-Europe*, Vol. 24, No. 2, pp. 28-34, 2007.

[105] Ph. Mandin, J. M. Cense, B. Georges, V. Favre, Th. Pauporte, Y. Fukunaka, D. Lincot, "Prediction of the Electrodeposition Process Behavior with the Gravity or Acceleration Value at Continuous and Discrete Scale", *Electrochimica Acta*, Vol. 53, pp. 233-244, 2007.

[106] K. I. Popov, P. M. Zivkovic, S. B. Krstic, N. D. Nikolic, "Polarization Curves in the Ohmic Controlled Electrodeposition of Metals", *Electrochimica Acta*, Vol. 54, pp. 2924-2931, 2009.

[107] Y. Lu, W. Wang, H. Xu, X. Kong, J. Wang, "Copper Corrosion and Anodic Electrodissolution Mechanisms in Naturally Aerated Stagnant 0.5 M H_2SO_4", *Corrosion Science*, Vol. 52, pp. 780-787, 2010.

[108] B. Sun, X-W Zou, Z-Z Jin, "Movement of the Deposit Segment in Thin Layer Electrochemical Cell- A Conjugate Dissolution/Deposition Behavior," *Electrochimica Acta*, Vol. 50, pp. 1031-1037, 2004.

[109] L. Zou and C. Hunt, “Characterization of the Conduction Mechanisms in Adsorbed Electrolyte Layers on Electronic Boards Using AC Impedance,” *Journal of Electrochemical Society*, Vol. 156, No. 1, C8-C15, 2009.

[110] Y. Leng, S. Cheng, J. Zhang, C. Zeng, and C. Wang, “Electrochemical Impedance Spectroscopy (EIS) of Metal Hydride Electrode and its Mathematical Model,” *Acta Physico-Chimica Sinica*, Vol. 13, No. 10, pp. 890-897, 1997.

[111] C. Deslouis, O. R. Mattos, M. M. Musiani, and B. Tribollet, “Comments on Mechanisms of Copper Electrodissolution in Chloride Media,” *Electrochimica Acta*, Vol. 38, No. 18, pp. 2781-2783, 1993.

[112] M. E. Folquer, S. B. Ribotta, S. G. Real, and L. M. Gassa, “Study of Copper Dissolution and Passivation Processes by Electrochemical Impedance Spectroscopy”, *Corrosion*, Vol. 58, No. 3, pp. 240-247, 2002.

[113] J. L. Barton and J. O’M. Bockris, “The Electrolyte Growth of Dendrites from Ionic Solutions”, Proceedings-Royal Society of London. Series A, Mathematical, Physical and Engineering Sciences, Vol. 268, Iss. 1335, pp. 485-505, 1962.

[114] J. Diggle, A. Despic, J. Bockris, “The Mechanism of the Dendritic Electrocrystallization of Zinc”, *Journal of The Electrochemical Society*: *Electrochemical Science*, Vol. 116, No. 11, pp.1503-1514, 1969.

[115] W. Paw, J. Nable and J. Swanson, “ ‘Behind the Scenes’ of Effective OSP Protection in Pb-free Processing”, *IEEE 3rd International Microsystems, Packaging, Assembly & Circuits Technology Conference*, Taipei, pp. 411-413, 2008.

[116] C. K. Chung, Y. J. Chen, C. C. Li, and C. R. Kao, "The Critical Oxide Thickness for Pb-free Reflow Soldering on Cu Substrate", *Thin Solid Films*, Vol. 520, pp. 5346-5352, 2012.

[117] S. Zhan, M. H. Azarian, and M. G. Pecht, "Surface Insulation Resistance of Conformally Coated Printed Circuit Boards Processed With No-Clean Flux", *IEEE Transactions on Electronics Packaging Manufacturing*, Vol. 29, No. 3, 2006, pp. 217-223.

[118] J. L. Barton and J. O'M. Bockris, "The Electrolytic Growth of Dendrites from Ionic Solutions", Proceedings of Royal Society of London, Vol. 268, 1962, pp. 485-505.

[119] A. R. Despic, J. Diggle, and J. O'M. Bockris, "Mechanism of the Formation of Zinc Dendrites", Journal of the Electrochemical Society: Electrochemical Science, Vol. 115, No. 5, 1968, pp. 507-508.

[120] A. R. Despic and M. M. Purenovic, "Critical Overpotential and Induction Time of Dendritic Growth", Journal of the Electrochemical Society: Electrochemical Science and Technology, Vol. 121, No. 3, 1974, pp. 329-335.

[121] J. W. Diggle, A. R. Despic, and J. O'M. Bockris, "The Mechanism of the Dendritic Electrocrystallization of Zinc", Journal of the Electrochemical Society: Electrochemical Science, Vol. 116, No. 11, 1969, pp. 1503-1514.

[122] K. I. Popov, M. D. Maksimovic, and D. T. Lukic, "The Mechanism of Copper Powder Formation in Potentiostatic Deposition", Journal of Applied Electrochemistry, Vol. 10, 1980, pp. 299-308.

[123] K. I. Popov, LJ. M. Djukic, M. G. Pavlovic, M. D. Maksimovic, "The Critical Overpotential for Copper Dendrite Formation", Journal of Applied Electrochemistry, Vol. 9, 1979, pp. 527-531.

[124] K. I. Popov, M. G. Pavlovic, M. D. Spasojevic, and V. M. Nakic, “The Critical Overpotential for Zinc Dendrite Formation”, Journal of Applied Electrochemistry, Vol. 9, 1979, pp. 533-536.

[125] J. H Shyu, “Roughness Evolution and Dendritic Growth in Electrodeposition”, PhD dissertation, Case Western Reserve University, 1982.

[126] J. N. Chazalviel, “Electrochemical Aspects of the Generation of Ramified Metallic Electrodeposits”, Physical Review A, Vol. 42, No. 12, 1990, pp. 7355-7367.

[127] V. Fleury, M. Rosso, J. N. Chazalviel and B. Sapoval, “Experimental Aspects of Dense Morphology in Copper Electrodeposition”, Physical Review A, Vol. 44, No. 10, 1991, pp. 6693-6705.

[128] O. Devos, C. Gabrielli, L. Beitone, C. Mace, E. Ostermann, and H. Perrot, “Growth of Electrolytic Copper Dendrites III: Influence of the Presence of Copper Sulphate”, *Journal of Electroanalytical Chemistry*, Vol. 606, 2007, pp. 95-102.

[129] V. Fleury, J. N. Chazalviel, and M. Rosso, “Theory and Experimental Evidence of Electroconvection around Electrochemical Deposits”, Physical Review Letters, Vol. 68, No. 16, 1992, pp. 2492-2495.

[130] V. Fleury, J. N. Chazalviel, and M. Rosso, “Coupling of Drift, Diffusion, and Electroconvection, in the Vicinity of Growing Electrodeposits”, Physical Review E, Vol. 48, No. 2, 1993, pp. 1279-1295.

[131] V. Fleury, J. Kaufman, and B. Hibbert, “Evolution of the Space-charge Layer during Electrochemical Deposition with Convection”, Physical Review E, Vol. 48, No. 5, 1993, pp. 3831-3840.

[132] V. Fleury, J. H. Kaufman, and D. B. Hibbert, “Mechanism of A Morphology

Transition in Ramified Electrochemical Growth", Nature, Vol. 367, 1994, pp. 435-438.

[133] M. Rosso, J. N. Chazalviel, V. Fleury, and E. Chassaing, "Experimental Evidence for Gravity Induced Motion in the Vicinity of Ramified Electrodeposits", Electrochimica Acta, Vol. 39, No. 4, 1994, pp. 507-515.

[134] J. N. Chazalviel, M. Rosso, E. Chassaing, and V. Fleury, "A Quantitative Study of Gravity-induced Convection in Two-Dimensional Parallel Electrodeposition Cells", Journal of Electroanalytical Chemistry, Vol. 407, 1996, pp. 61-73.

[135] G. Marshall, E. Perone, P. Tarela, and P. Mocskos, "A Macroscopic Model for Growth Pattern Formation of Ramified Copper Electrodeposits", Chaos, Solitons & Fractals, Vol. 6, 1995, pp. 315-324.

[136] G. Marshall, and P. Mocskos, "Growth Model for Ramified Electrochemical Deposition in the Presence of Diffusion, Migration, and Electroconvection", Physical Review E, Vol. 55, No. 1, 1997, pp. 549-563.

[137] G. Marshall, P. Mocskos, H. L. Swinney and J. M. Huth, "Buoyancy and Electrically Driven Convection Models in Thin-layer Electrodeposition", Physical Review E, Vol. 59, No. 2, 1999, pp. 2157-2167.

[138] G. Marshall, E. Mocskos, F. V. Molina, and S. Dengra, "Three-dimensional Nature of Ion Transport in Thin-layer Electrodeposition", Physical Review E, Vol. 68, 2003, pp. 021607 (1~8).

[139] G. Marshall, E. Mocskos, G. Gonzalez, S. Dengra, F. V. Molina, and C. Iemmi, "Stable, Quasi-stable and Unstable Physicochemical Hydrodynamic Flows in Thin-layer Cell Electrodeposition", Electrochimica Acta, Vol. 51, 2006, pp. 3058-3065.

[140] J. C. Bradley, S. Dengra, G. A. Gonzalez, G. Marshall and F. V. Molina, "Ion Transport and Deposit Growth in Spatially Coupled Bipolar Electrochemistry", *Journal of Electroanalytical Chemistry*, Vol. 478, 1999, pp. 128-139.

[141] G. Marshall, F. V. Molina, A. Soba, "Ion Transport in Thin Cell Electrodeposition: Modeling Three-Ion Electrolytes in Dense Branched Morphology under Constant Voltage and Current Conditions", *Electrochimica Acta*, Vol. 50, 2005, pp. 3436-3445.

[142] G. DiGiacomo, "Metal Migration (Ag, Cu, Pb) in Encapsulated Modules and Time-to-Fail Model as a Function of the Environmental and Package Properties", Proceedings of IEEE 20thInternational Reliability Physics Symposium, San Diego, CA, Mar. 30/31, 1982, pp. 27–33.

[143] S. Yang and A. Christou, "Failure Model for Silver Electrochemical Migration", *IEEE Transactions on Device and Materials Reliability*, Vol. 7, No. 1, 2007, pp. 188-196.

[144] http://sciencefocus.com/qa/how-small-can-naked-eye-see, latest accessed on Nov 16th, 2013.

[145] D. Q. Yu, W. Jillek, and E. Schmitt, "Electrochemical Migration of Sn-Pb and Lead Free Solder Alloys under Distilled Water", *Journal of Materials Science: Materials in Electronics*, Vol. 17, No. 3, 2006, pp. 219-227.

[146] C. H. Hamann, A. Hamnett, and W. Vielstich, *Electrochemistry*, New York: Wiley-VCH, 1998, pp. 36-44.